Probability of a rogue wave inducing extreme motions in a spar-type floating wind turbine

Tijmen Pieter Nederkoorn

T̃U Delft

Intecsea
Worley Group

Probability of a rogue wave inducing extreme motions in a spar-type floating wind turbine

by

Tijmen Pieter Nederkoorn

to obtain the degree of

Master of Science
in Offshore and Dredging engineering
at Delft University of Technology,

to be defended publicly on Wednesday July 14, 2021 at 13:00.

Thesis committee:	Dr. ir. C. L. Walters,	TU Delft, Chairman
	Dr. ir. H. C. Seyffert,	TU Delft, Supervisor
	Dr. ir. O. Morales Napoles,	TU Delft
	Dr. ir. P. Liu,	IntecSea
Student number:	4473183	
Project duration:	November 8, 2020 – July 14, 2021	

This thesis is confidential and cannot be made public until July 14, 2023.

An electronic version of this thesis is available at `http://repository.tudelft.nl/`.

TUDelft

Intecsea
Worley Group

Preface

Before you lies my Msc. thesis 'Probability of a rogue wave inducing extreme motions in a spar-type floating wind turbine'. This thesis was written to obtain a Master of Science degree in Offshore and Dredging engineering at the Technical University Delft.

The research project was executed in collaboration with IntecSea. The topic was established by combining my interest in waves and offshore wind energy with Harleigh's fascination for rare waves and statistics and IntecSea's desire to explore floating wind concepts. The work was carried out while fully working from home due to the COVID-19 restrictions during November 2020 to July 2021.

During my research I received an incredible amount of support from different directions. First and foremost, I want to thank my involved committee members. Harleigh, thank you for your endless enthusiasm, advice and interesting discussions. Our in-depth bi-weekly meetings, together with your sharp observations and excellent understanding of the relevant academical field have been invaluable to me. Ping, thank you for your constant support and guidance. Your curiosity about the underlying physics of my findings continuously encouraged me to broaden my understanding of the subject. Carey, I greatly valued your outside perspective and keen research oriented comments. Also, the monthly digital master student collaboration meetings that you organized were a very welcome way to hear and talk about research from peers. In addition, I would like to thank Martijn and Jeroen from IntecSea for their help and involvement in the bi-weekly meetings, and my fellow graduate student Freek, with whom I could share struggles and on-topic conversations during the whole process.

Furthermore, I would like to thank my housemates and colleague at-home graduate students Dirk, Mark, Oyono and Laurens for keeping me sane in the dark lockdown winter with endless outside exercising, gourmet lunches and improvised parties. Finally, I want to thank my parents Joost en Marijke and my brother Stijn for their perpetual support and enthusiasm, not only during the writing of this thesis, but during my whole studies.

Tijmen Pieter Nederkoorn
Delft, July 2021

Abstract

Due to the need for more renewable energy, interest in floating wind turbines has greatly increased over the last years. These turbines have to withstand harsh environmental conditions, such as extreme waves called rogue waves. These rogue waves (or freak waves) are exceptionally large waves compared to the surrounding sea state and are defined by two different size criteria, one relating to the crest height and the other to the wave height. Research has shown that these rogue waves occur more frequently than expected, from which the question arose whether these rogue waves could be dangerous for floating wind turbines.

This thesis aims to answer that question by evaluating the probability of such a wave interacting with a floating offshore wind turbine and the subsequent induced motion response. A location off shore California is evaluated for a spar-type floating wind turbine (SFWT). In this research, different time-extreme (TE) and space-time-extreme (STE) statistical wave crest and crest-to-trough models are used with historical wave data to estimate rogue wave occurrence probabilities. The STE models approximate the probability of a wave occurring within an area in time, as opposed to a point in time (TE), and are considered state-of-the-art. Wave data from 1998-2020 is used, which is a significant amount compared to the life of a typical offshore structure. A frequently chosen model for research into a SFWT is the OC3-Hywind concept, which consists of the National Renewable Energy Laboratory (NREL) 5MW reference turbine and a substructure based on the Hywind spar.

The area size which leads to the STE models estimating a higher rogue wave occurrence probability than the TE models is investigated for the first time. This is done by comparing the TE and STE probability models to each other on the basis of their maximum estimated exceedance probability of the rogue threshold, for different area sizes. Only on rare occasions, with a very small area, did the most conservative TE wave crest model estimate a higher probability than the STE2 (wave crest STE) model. Therefore, the STE2 model appears most conservative when evaluating rogue crests for a SFWT.

The Rayleigh model was the most conservative among TE crest-to-trough models that were considered, and estimated higher probabilities than the STE1QD (wave crest-to-trough STE) model in several sea states up until an area size of $12\times12\text{m}^2$.

The influence of the shape of the wave spectrum was investigated by two spectral bandwidth parameters. All four wave crest models showed an increase in rogue crest probability as the wave spectrum became narrower. Regarding the crest-to-trough models, no clear preference was observed.

Long-term rogue wave probabilities were calculated for four sizes of rogue crests and waves, where the squared area of the STE models was based on the waterline diameter of the OC3-Hywind spar ($6.5\times6.5\text{m}^2$). Probabilities were averaged per sea state bin, and it was observed that for this area the STE1QD model was more conservative than the Rayleigh model. When single maximum exceedance probabilities are compared, the Rayleigh model can be more conservative in several sea states until an area of $12\times12\text{m}^2$, but when overall occurrence probabilities are considered, this area appears to be roughly $6.5\times6.5\text{m}^2$.

Following the long-term rogue wave probability analysis, four rogue waves were each embedded in random wave series, based on their most likely wave spectrum, using a deterministic extreme wave model. With these wave time histories, simulations were run in OrcaFlex using a publicly available OC3-Hywind model. During the simulation the turbine was assumed to be in parked condition and only the wave loading was considered. Mostly the pitch angles and nacelle accelerations are limiting for safety, due to stability criteria and sensitive components in the nacelle. These limits are imposed by turbine manufacturers but are never shared publicly. Therefore, the results were compared with reference values from the literature. The dynamic response did not exceed these maximum reference values, but they can be considered quite serious as some did exceed lower thresholds.

Based on the long return period of the considered rogue waves, together with their induced dynamic response which does not exceed maximum reference values, it appears that these rogue waves alone are not dangerous for the considered SFWT. However, ultimately this will depend on the sensitivity of the components inside the turbine, as well as the desired risk profile of the wind farm owner.

Contents

List of Abbreviations

BFI	Benjamin-Feir index
CM	Center of mass
DNV	Det Norske Veritas
DOF	Degree of freedom
ECMWF	European Centre for Medium-Range Weather Forecasts
FFT	Fast Fourier transform
GW	Gigawatt
Hywind	The Hywind Scotland floating wind farm
IRENA	International Renewable Energy Agency
kWh	Kilowatt-hour
MLW	Most likely wave (model)
MSL	Mean sea level
MW	Megawatt
NDBC	National Data Buoy Center
NOAA	National Oceanic and Atmospheric Administration
NREL	National Renewable Energy Laboratory
OC3	Offshore Code Comparison Colaboration
OEM	Original equipment manufacturer
QD	Quasi-determinism
SFWT	Spar floating wind turbine
STE	Space-time extreme
SWL	Still water level
TE	Time-extreme
TLP	Tension-leg platform

List of Figures

List of Tables

1

Introduction

Excessive use of fossil fuels in the last century has skyrocketed the concentration of carbon dioxide in the earth's atmosphere. Since the beginning of the industrial age, the amount of CO2 in the atmosphere has increased 47% and in the short time-span from the year 2000 until present with 11% [16]. This CO2 surge has caused the world's temperature to increase up until the point that if no widespread carbon neutral energy is adopted we are heading towards a large scale environmental disaster. In 2015, 196 parties signed the Paris agreement with the goal to limit the global increase in temperatures to below 2°C, preferably even below 1.5°C. To reach this goal, participating countries have to reach their peak in carbon emissions as soon as possible to achieve a carbon-neutral world by 2050.

Due to the need for more renewable energy the interest in offshore wind energy has grown substantially over the last years. Bottom founded wind turbines have grown larger and the price per kWh has been reduced drastically. Northern Europe is a leader in the field of offshore wind energy where currently all the major wind farms are located. As of 2019, 22 GW of offshore wind power has been installed in Europe, which accounts for roughly 75% of the global installed power [54] [48]. In recent years other markets for offshore wind energy have started to emerge at an accelerating pace as well, such as China, the United States, Taiwan and Japan. Not only are these countries eager to decrease their carbon footprint, but also to establish their own supply chain as to benefit their economies. Figure 1.1 presents a forecast by the International Renewables Energy Agency IRENA of the expected total installed offshore wind energy, with a total capacity nearing 1000 GW by 2050.

As we progress into deeper waters where there is even more wind energy potential, the need for viable floating wind concepts increases. The wind at deeper waters blows more consistently and strongly which can yield more energy. In these depths bottom founded wind turbines become increasingly expensive, making floating wind turbines an attractive alternative. Right now industry experts believe that in 2030, 5GW to 30GW of floating offshore wind capacity could be installed worldwide [42]. At the moment, the Equinor Hywind Scotland and the Windplus WindFloat Atlantic farm are the only operational floating wind farms in the world. The Hywind farm consists of 5 6-MW turbines placed on a spar substructure. It was the first wind farm to demonstrate on an industrial scale the feasibility of floating offshore wind and paved the way for future initiatives. The WindFloat Atlantic farm consists of three 8.4-MW turbines supplying about 25MW to Portugal's electrical grid. The turbines are placed on a semi-submersible structure and are the world's largest turbines ever installed on a floating platform.

1.1. Floating wind concepts

Floating wind concepts can be divided into three main categories depending on their substructure: tension-leg platform, spar and semi-submersible. Figure 1.2 shows an overview of the different support structure types for both fixed and floating wind turbines. The floating designs are based mostly on structures from the oil and gas industry. The main difference between these concepts is how they achieve their stability.
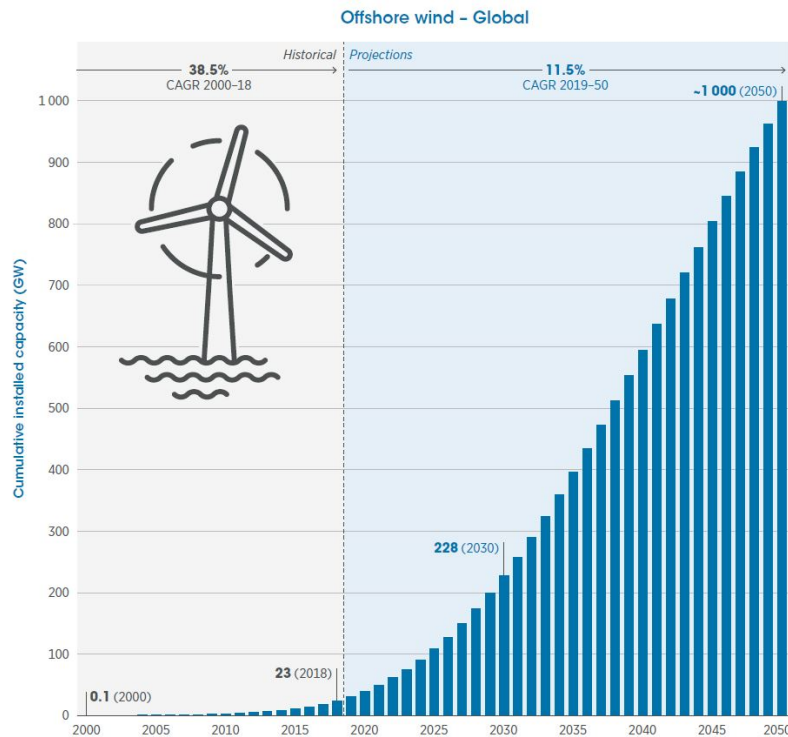
Figure 1.1: Historical and expected offshore wind capacity statistics based on IRENA's analysis [42].

1.1.1. Spar buoy

A spar buoy is a long slender ballast-stabilised cylinder attached to the seabed by a catenary or taut-spread mooring system. A spar achieves its stability by having the center of gravity below the center of buoyancy which provides a restoring moment to counteract wind and wave loads. The low center of gravity provides high intertial resistance against roll and pitch motions and the small waterplane area of the spar reduces the wave loads [50]. Fabrication is relatively simple because of the common shape, however the deep draught of the hull can cause logistical challenges during the assembly, transportation and installation. Also, this deep draught may restrict the spar type substructures to mostly deeper waters of >$100m$ [17].

1.1.2. Semi-submersible

A semi-submersible structure is a buoyancy-stabilised platform connected to the seabed with a catenary mooring system. Stability is achieved by changes in the submerged volume. Inclination of the platform due to a heeling moment will result in a larger submerged volume on the leeward side, inducing a counteracting restoring moment. Semi-submersibles have a low draught which allows outfitting, commissioning and even the turbine installation to be done on the dock. [53].

1.1.3. Tension-leg platforms

A TLP is a structure with a large buoyancy held in place by a tension-leg mooring system. The tension-leg mooring system connects the structure to the seabed via vertical tethers. The buoyancy of the structure is greater than the weight of the turbine. The extra buoyancy is used to tension the tethers which are connected to anchors on the seabed [73]. These are mostly gravity-based anchors, suction or pile driven. Due to this design the anchor mooring system has to withstand large vertical loads. This imposes certain seabed requirements and makes the installation complex and expensive [17]. The heeling moment induced by the wind is counteracted by a restoring moment resulting from a higher tension in the windward leg compared to the leeward leg. TLPs have a relatively shallow draft which allows for tow-out installation.

Figure 1.2: Types of foundations and moorings for bottom fixed and floating offshore wind turbines. From left to right: Monopile, Jacket, TLP, Spar, Semi-submersible [5].

1.2. Rogue waves

Floating wind turbines in deep water are subjected to harsh environmental conditions. Wind blowing unobstructed over a large area can generate large waves which together with the already strong wind will exert a significant environmental loading on the floating wind turbine. In the last 20 years, a lot of research has been done on a wave phenomenon called rogue waves. Rogue waves (often also called freak waves or monster waves) are unusually large waves relative to the surrounding sea state. Tales of single monster waves seen on the seas and ocean were often dismissed as typical sailor stories and until recently there was no evidence of these events. The concept of these oceanic rogue waves was introduced by Draper in 1966 [25]. Then, in 1984, the first rogue wave was recorded by the Gorm platform in the North sea. However, the New Years wave measured at the Draupner plaform in 1995 is what really got the scientific community interested [27]. Figure 1.3 displays the time records of these two well-known examples where the abnormality of the wave height relative to the sea state is clearly visible.
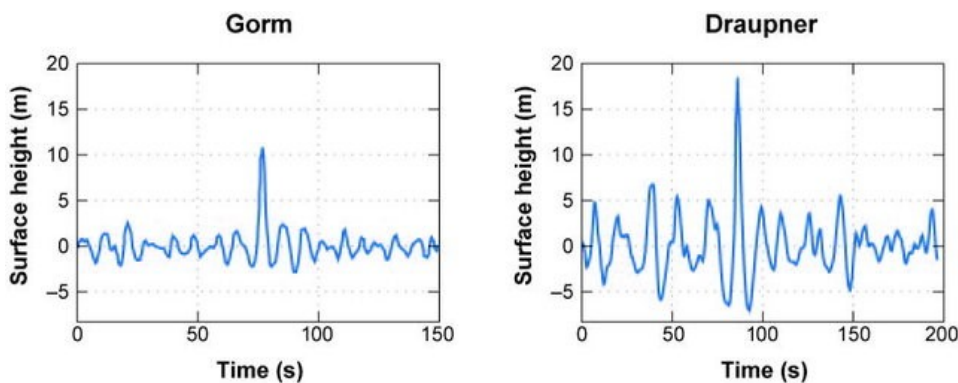
Figure 1.3: Two examples of a rogue wave record. The left panel displays the Gorm wave recording and the right panel the Draupner wave [27].

Rogue waves have been attributed as the cause of numerous shipping disasters over the last decades, such as the Louis Majesty cruise ship which was hit by an enormous rogue wave and killed two passengers, or the Suwa-Maru incident where a rogue wave is suspected to have sunk a fishing boat with 20 crew members in a moderate seastate [79] [20]. In a report from 2002, Faulkner evaluated cargo shipping accidents from the years 1981 to 2000 and concluded that a significant portion of these accidents are due to inadequate design against the worst possible wave conditions, also believed to be rogue waves [30]. An EU funded project

called MaxWave which involved different meteorological agencies, universities and research facilities set out to prove the existence of rogue waves and the risk of encounter [68]. For three weeks parts of the oceans were searched with radar and satellite technology to collect wave data. Numerous of these rogue waves were found and one of the conclusions from the MaxWave project, endorsed by other subsequent research, was that rogue waves occur more frequently than previously expected by conventional wave statistics [9] [31].

1.3. Research motivation

The question that arises from this conclusion is that when rogue waves are said to occur more frequently than expected and numerous ship accidents have already been caused by these waves, could they be a threat to the upcoming floating wind turbines as well? The motivation for this thesis therefore is to assess the probability of a rogue wave striking a floating offshore wind turbine and whether the subsequent impact could pose a threat to the survivability. To evaluate this, the spar type concept is chosen because of its technical maturity and proven feasibility over multiple years.

This report is structured as follows: first the phenomenon of the rogue waves is further investigated with the research focus on models which can predict the occurrence of rogue waves. Second, the physics governing the dynamic response of the spar floating wind turbine system is evaluated and existing research done into extreme response of a SFWT as a result of large waves is presented. Then, the research objectives and methodology is presented based on the identified literature gaps. Thereafter, the research into the rogue wave probability is presented, followed by the research into the dynamic response of the SFWT against rogue waves, after which relevant conclusions are made regarding the research objectives.

2

Rogue waves

Rogue (or freak) waves are not necessarily only very large waves. Their name refers to their size relative to the surrounding waves and their spontaneous appearance. Although there is no single true definition of a rogue wave, two scientific definitions have been widely adopted in academic literature to classify these waves. The first definition was introduced by Klinting and Sand in 1987 and consists of three rules [59]:

- *It has a wave height larger than two times the significant wave height.*

- *Its wave height is larger than two times of the fore-going and following waves.*

- *Its wave crest is larger than 65% of its wave height.*

This definition was reformulated in 1990 to include only the first statement as presented by equation 2.1 below [71].

$$\frac{H}{H_s} \geqslant 2 \tag{2.1}$$

Here H denotes the rogue wave height and H_s the significant wave height. The second rogue wave definition relates the crest height, η_c, to the significant wave height [27]:

$$\frac{\eta_c}{H_s} \geqslant 1.25 \tag{2.2}$$

It is common to assume a 20-minute sea state for these rogue wave thresholds, which is a characteristic duration for wave buoy time series. The DNVGL-RP-C205, a guideline for environmental conditions analysis, has adopted this sea state duration in their rogue wave definition, together with both possible thresholds as given by equation 2.1 and 2.2 [24].

This chapter presents a brief introduction on the existing knowledge of rogue waves and evaluates methods that can be used to predict rogue wave occurrence. First, linear and nonlinear wave theory is revisited to serve as a stepping stone to explain mechanisms believed to be responsible for rogue wave formation and lay the groundwork for basic wave statistics. Then, previous research into rogue wave occurrence is briefly evaluated and statistical wave models are discussed.

2.1. Linear wave theory

The basic concept to explain random water waves is based on the principle of summing a large number of independent harmonic waves. The waves due to their linear character are assumed not to affect each other as they travel across the water surface. For linear theory to be applicable the wave amplitude has to be small compared to the wave length and the water depth. The linear wave theory is also known as the Airy wave theory which is why the harmonic wave involved is sometimes called the Airy wave [3].

Figure 2.1 displays the superposition principle of the independent harmonic waves. The surface elevation at any given time and location in 3D is given by equation 2.3.

$$\underline{\eta}(x, y, t) = \sum_{i=1}^{N} \sum_{j=1}^{M} \underline{a}_{i,j} \cos\left(\omega_i t - k_i x \cos\theta_j - k_i y \sin\theta_j + \underline{\alpha}_{i,j}\right) \tag{2.3}$$

Where $\underline{a}_{i,j}$ is the wave amplitude, ω_i the frequency, $k_i = \frac{2\pi}{\lambda}$ represents the wave number with λ being the wave length, θ_j the direction and $\underline{\alpha}_{i,j}$ the phase. The amount of wave components (N) should approach infinity and phase distribution should be uniform for the surface elevation to be Gaussian distributed.
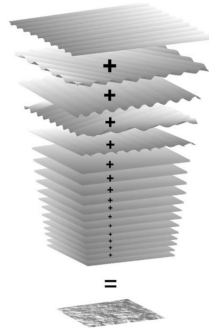
Figure 2.1: Superposition of a large number of different harmonic waves moving across the ocean surface which results in the random phase/amplitude model. Originally after Pierson *et al.*, 1955, retrieved from [40].

The wave velocity potential is given by equation 2.4 below. The particle velocity components are obtained by taking the derivatives $\delta\phi/\delta x$ and $\delta\phi/\delta z$, respectively given by equation 2.5 and 2.6. In deep water, the water particles under a harmonic wave move with an orbital motion where the wave-induced velocities decrease exponentially as the distance from the surface increases.

$$\phi = \frac{\omega a}{k} \frac{cosh[k(d+z)])}{sinh(kd))} cos(\omega t - kx)) \tag{2.4}$$

$$u_x = \omega a \frac{\cosh[k(d+z)])}{\sinh(kd)} \sin(\omega t - kx) \quad (2.5) \qquad u_z = \omega a \frac{\sinh[k(d+z)]}{\sinh(kd)} \cos(\omega t - kx) \quad (2.6)$$

Waves each propagate at their own velocity, which can be obtained from the dispersion relationship. The dispersion relationship relates frequency ω with the wave number k and the depth d (Eq. 2.7). By substituting the wave number by the wavelength this relationship could also be written as equation 2.8.

$$\omega^2 = gk\tanh(kd) \quad (2.7) \qquad L = \frac{gT^2}{2\pi}\tanh\left(\frac{2\pi d}{L}\right) \quad (2.8)$$

The expression for the phase speed (Eq. 2.9) shows that the velocity depends on the wave frequency and wave number. These properties are related to each other via the dispersion relationship, displaying the property that long waves propagate faster than short waves. Waves traveling over the free surface of the ocean will separate themselves based on their wavelength.

$$c_p = \frac{\lambda}{T} \text{ or } \frac{\omega}{k} \tag{2.9}$$

Two (or more) waves with slightly different frequencies traveling over the free surface can add up to form a series of wave groups. When the waves are in phase the crests coincide and the wave group has its maximum surface elevation. Similarly, when a wave crest coincides with another wave's trough they cancel each other out and the wave group has its minimum surface elevation. This phenomenon is illustrated by figure 2.2.
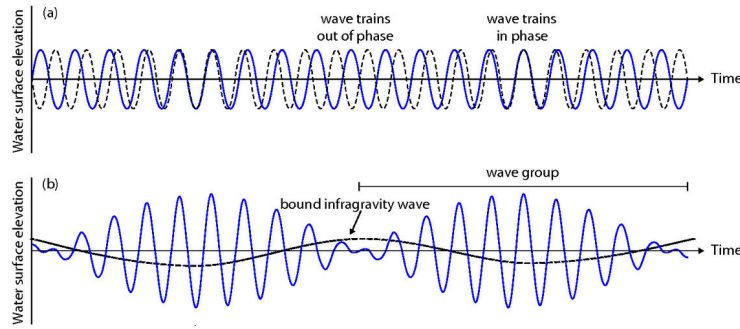
Figure 2.2: Two waves with slightly different frequencies merging into a wave group, retrieved from [7].

2.2. Nonlinear waves

When waves become too steep or the water becomes too shallow, deviations from the linear wave theory arise. The linear wave theory is no longer valid since the harmonic waves only approximate the nonlinear equations. Stokes (1847) presented a nonlinear wave theory which aims to provide a better approximation for a nonlinear wave profile by adding extra harmonic waves to the primary harmonic wave [37]. This theory writes the nonlinear wave by successive corrections (each higher-order correction is acquired based on the preceding lower-order correction) formulated in terms of the velocity potential. The wave steepness $\epsilon = ak$ is specially represented by Stokes' theory in the basic harmonic:

$$\eta(x, t) = a\cos(\omega t - kx) = \epsilon\eta_1(x, t) \tag{2.10}$$

where $\eta_1(x, t) = k^{-1}\cos(\omega t - kx)$. Now, a correction can be added to this basic component, written with the wave steepness raised to the second power (therefore also called a second-order correction or second-order stokes wave):

$$\eta(x, t) = \epsilon\eta_1(x, t) + \epsilon^2\eta_2(x, t) \tag{2.11}$$

The second harmonic wave which is added has the same phase speed as the initial linear wave and is therefore called a bound second harmonic. The Stokes expansion can be continued in the same sense by adding a third, fourth, fifth harmonic. Equation 2.12 illustrates the Stokes expansion up to the fifth order. This process can be expanded indefinitely until the desired order of correction is achieved. Characteristic for these nonlinear waves is the asymmetry between the crests and troughs as illustrated in figure 2.3. The crests are a little sharper and the troughs are flatter compared to the linear wave.

$$\eta(x, t) = \epsilon\eta_1(x, t) + \epsilon^2\eta_2(x, t) + \epsilon^3\eta_3(x, t) + \epsilon^4\eta_4(x, t) + \epsilon^5\eta_5(x, t) \tag{2.12}$$
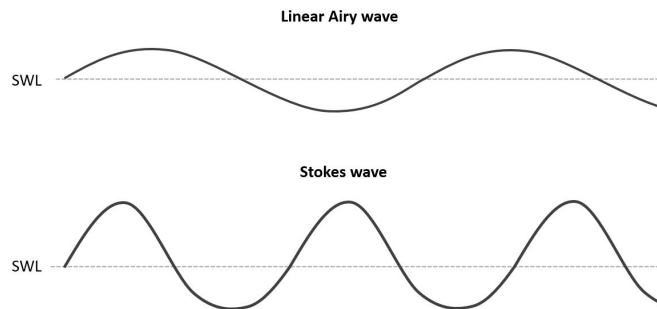
Figure 2.3: Schematic representation of the wave profiles of a linear Airy wave and a Stokes wave.

2.3. Short-term wave statistics

Wind waves are usually assumed to be approximated by a stationary, Gaussian process. The Gaussian probability density function of the surface elevation η is given by Eq. 2.13, where σ is the standard deviation which can also be written as $m_0^{1/2}$. This moment m_0 is the zeroth moment of the wave energy spectrum.

$$p(\eta) = \frac{1}{\sigma (2\pi)^{1/2}} \exp\left(-\frac{\eta^2}{2m_0}\right) \tag{2.13}$$

Generally there is a good agreement between observed or measured wave records and the Gaussian theoretical distribution in deep water. However, high crests are slightly underestimated by this distribution while deep troughs are somewhat overestimated [40]. Steeper waves or waves in shallow water deviate quicker because of their nonlinear character. Due to nonlinear processes wave crests become higher and sharper and troughs become flatter and shallower.

2.3.1. Crest and wave height distribution

The probability density function of the linear crest height (η_c) is a Rayleigh type distribution (Eq. 2.14). It depends on only one parameter: the zero-order moment m_0 of the variance density spectrum [40]. The cumulative distribution function is then given by equation 2.15 below.

$$p_{\underline{\eta}_c}(\eta) = \frac{\eta}{m_0} \exp\left(-\frac{\eta^2}{2m_0}\right) \tag{2.14} \qquad \Pr\left\{\underline{\eta}_c \le \eta\right\} = 1 - \exp\left(-\frac{\eta^2}{2m_0}\right) \tag{2.15}$$

For linear waves in deep water we may approximate that the wave height is about twice the crest height: $H \approx 2\eta_c$. With that assumption the wave height probability distribution follows from Eq. 2.14 and is given by equation 2.16 below. Equation 2.17 is derived from equation 2.15 in the same sense. The significant wave height is defined as the mean of the highest one-third of the waves, see figure 2.4.

$$p(H) = \frac{H}{4m_0} \exp\left(-\frac{H^2}{8m_0}\right) \tag{2.16} \qquad \Pr\left\{\underline{H} \le H\right\} = 1 - \exp\left(-\frac{H^2}{8m_0}\right) \tag{2.17}$$
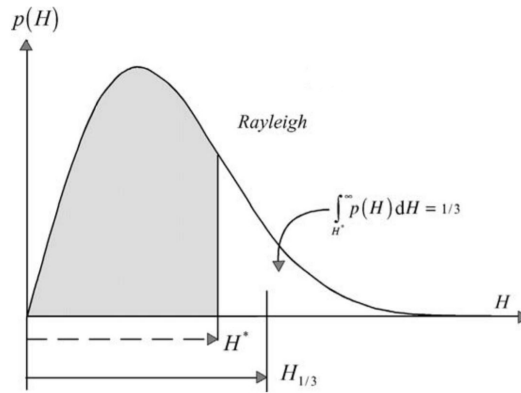
Figure 2.4: Rayleigh distribution as wave height probability density function. The significant wave height is indicated as $H_{1/3}$. Retrieved from [40].

2.3.2. Maximum wave heights

Intuitively one can already deduce that a within a large number of wave realizations the chance of a large wave occurring increases compared to evaluating a single crest. During a time duration D there will be a certain number of waves, which can be denoted by N. An estimate for N is to take the wave mean zero-crossing frequency, or 1 divided by the mean zero-crossing period, and multiply this by the duration D in seconds (Eq. 2.18).

$$N = f_0 D = T_0^{-1} D = \sqrt{\frac{m_2}{m_0}} D \tag{2.18}$$

The probability that a wave crest exceeds a certain threshold level η is given by $\Pr\{\underline{\eta}_c > \eta\}$, which can be calculated with equation 2.14 when the Rayleigh distribution is considered. Subsequently, the probability that this wave crest does <u>not</u> exceed the threshold can be written as $1 - \Pr\{\underline{\eta}_c > \eta\}$. Assuming all crests to be statistically independent, the probability that N wave crests within duration $\overline{D}$ do not exceed threshold η is given by:

$$\Pr\{\text{all}\,\underline{\eta}_c \leq \eta\} = (1 - \Pr\{\underline{\eta} > \eta\})^N \tag{2.19}$$

Then, to calculate the probability that a wave crest will be <u>larger</u> than the threshold, equation 2.20 can be used.

$$\Pr\{\underline{\eta}_{max} > \eta\} = 1 - (1 - \Pr\{\underline{\eta}_c > \eta\})^N \tag{2.20}$$

2.4. Rogue wave formation

There are different competing theories about physical mechanisms that are responsible for the formation of rogue waves [59]. Both linear and nonlinear effects have been shown to cause these large wave outliers and so far no true consensus has been reached about the most prominent generation mechanism.

First, there is geometrical (or spatial) focusing. This is the focusing of waves due to interference of wave systems coming from different directions, such as waves generated at different storm locations, or because of refraction/diffraction due to specific bathymetry. See for example figure 2.5, where Fochesato *et al.* (2007) created rogue waves in a numerical wave tank by directional focusing of waves [35].
Somewhat similar is temporal focusing of the waves due to their dispersive nature. Different ocean waves propagating at their own velocity can come into phase at a single location which results in a large concentration of energy [76]. Figure 2.2 illustrates a simplified version of this effect, where the waves coming into phase result in the largest wave of the group.
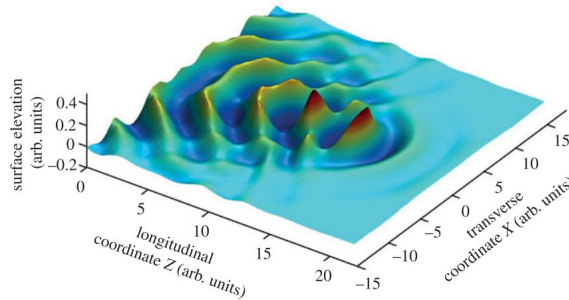
Figure 2.5: Numerical simulation of a rogue wave being formed by directional focusing of waves. Originally from [35], retrieved from [26].

A nonlinear effect responsible for rogue wave formation which has received much attention is modulational instability [43]. Modulational instability is the result of interaction between a carrier wave propagating at frequency ω and sidebands at $\omega \pm \Omega$ [89]. The crux of this effect is the unstable growth of weak wave modulations and can be illustrated as follows: when the Stokes wave becomes unstable, one wave in the middle of the wave group starts to grow at the expense of the waves around it, thus enabling the creation of a single large wave.

In recent years, the validity of the modulational instability theory for realistic ocean wind seas has been questioned. Experiments with rogue wave formation as a result of modulational instability ([64] [84] [83]) were performed with long-crested uni- or (narrow banded) directional waves, while real sea states are characterized by short-crested multidirectional wave fields [84] [83]. In real seas, the wave energy can spread out directionally and nonlinear focusing due to modulation instability is diminished [34]. In recent research there is increasing agreement that a plausible mechanism for rogue wave formation is spatio-temporal focusing as a result of the dispersive nature of the water waves [10] [22] [34] , strengthened by second-order non-resonant nonlinearities [80].

2.5. Rogue wave occurrence

Estimating the occurrence probability of rogue waves is a key topic of rogue wave research. Their large size and unpredictable nature can pose a real threat to ships and offshore structures. Since there is no consensus on the principal mechanisms responsible for these waves, estimating their probability proves to be a difficult task. Because rogue waves are rare statistical events, brute-force computational simulations are extremely time-consuming and are deemed infeasible for most applications. In the same sense, searching for rogues in ocean measurements, for example with wave buoys (figure 2.6), in order to extrapolate those statistics proves to be very difficult. Wave buoys can underestimate the wave peaks by being dragged through the crest or by sliding sideways from the highest point, thereby avoiding short-crested extreme waves [74] [36]. Furthermore, point measurements in a 2D grid do not provide accurate estimates of the space-time wave dynamics and the associated maximum wave elevation over a given area surrounding the buoy [33]. This is what makes it difficult to collect large amounts of high quality wave data containing rogues, causing research to search for alternatives.

In this section, previous research into rogue wave occurrence is briefly evaluated and their applicability to this thesis is discussed. Then, several statistical wave crest and crest-to-trough models are presented in detail where special interest is paid to the state-of-the art space-time extreme (STE) wave models.

Figure 2.6: A Datawell directional waverider buoy deployed by the Hydrographic Institute of the Republic of Croatia. Retrieved from [52].

2.5.1. Previous research into rogue wave occurrence

A study by Cattrell *et al.* (2018) investigated whether characteristic wave parameters can be used as fast predictors of increased rogue wave probability [19]. Rogue waves in wave data from 80 waverider buoys were identified and investigated in relation to significant wave height, wave steepness, wave skewness, kurtosis and spectral bandwidth parameters. Overall, the research concluded that the large data size did not yield a discernible link between rogue wave occurrence and the investigated characteristics.

Several studies looked into the influence of sea surface kurtosis on the occurrence probability of rogue waves in relation to modulational instability of the waves [58] [43] [83]. Kurtosis is a scaled version of the fourth moment of the probability distribution and can be seen as a measure of the "tailedness" of this distribution. A high kurtosis indicates a higher probability of outliers, such as rogue waves. Research into the modulational instability assumes unidirectional waves since a narrow-band approximation is used. Validity for real seas where the waves are spread out over multiple directions is therefore not assured.

The hindcasting of meteorological conditions for known rogue waves has been an extensive part of rogue wave research. Due to the certainty of a rogue wave being present in those conditions researchers aim to find key meteorological indicators and explanations for rogue waves. Many studies have investigated known rogue waves [39] [21] [20], such as Adcock *et al.* (2011) who discussed different explanations for the famous Draupner wave [1]. The focus in this area of research is predominantly on explaining how a rogue wave could have formed in such conditions. At the moment, research into hindcasting has not yet produced usable key indicators for rogue wave formation such that they could be used in a statistical analysis.

2.5.2. Statistical wave models

Two rogue wave definitions were presented at the beginning of this chapter, one regarding the wave height (crest-to-trough height) and one regarding the crest height. Due to the different statistical nature of crest and crest-to-trough heights these wave parameters have to be estimated using separate models. Research into statistical models that fit these wave parameters best has been an important research topic over the last decades. These models could provide an accurate estimate of rogue wave occurrence and are therefore highly interesting for this thesis.

Investigating short time wave statistics, research has shown that the statistical description of crest heights is highly influenced by nonlinearities, while crest-to-trough heights are only slightly affected [18] [81] [57]. In this section relevant time-extreme (TE) and space-time-extreme (STE) wave probability models will be presented for these wave parameters.

Crest-to-trough heights - TE
Because crest-to-trough heights are only slightly affected by nonlinearities, the linear Rayleigh distribution (Eq. 2.16) presented in section 2.3.1 is generally considered an overestimation for wave heights occurring at a certain location. A better estimation is given by a bandwidth corrected version of the Rayleigh distribution, originally presented by Naess in 1985 [61]:

$$P_N(H > h) = \exp\left[-\frac{4}{1 - \Psi^*}\left(\frac{h}{H_s}\right)^2\right]$$

(2.21)

This distribution accounts for finite bandwidth effects by incorporating bandwidth parameter ψ^*. Here ψ^* is the minimum of the autocorrelation function of the sea surface, which can be estimated from the wave spectrum as:

$$\psi(t) = \frac{1}{\sigma^2}\iint S(\omega,\theta)\,d\theta\cos(\omega t)\,d\omega$$

(2.22)

The Rayleigh distribution is recovered from equation 2.21 for a value $\psi^* = -1$.

Crest heights - TE
Crest heights are largely affected by nonlinearities. Tayfun (1980) presented a probability model to approximate second order Stokes' waves [80]. The Tayfun distribution is solely dependent on the wave steepness, and is given by:

$$P_T\{\eta_c/\sigma > \xi\} = \exp\left[-\frac{(-1 + \sqrt{1 + 2\mu\xi})^2}{2\mu^2}\right]$$

(2.23)

where $\xi = \xi_0 + \frac{\mu}{2}\xi_0^2$ is the second order wave elevation related to the linear wave elevation ξ_0 and

$$\mu = \mu_m\left(1 - v + v^2\right)$$

(2.24)

is a measure of the wave steepness where

$$\mu_m = \sigma\left(2\pi m_{001}/m_{000}\right)^2/g$$

(2.25)

is corrected with the spectral bandwidth as given by equation 5.5 [32]. The directional spectral moments are given by $m_{ijk} = \iint k_x^i k_y^j f^k S(f,\theta)\,df\,d\theta$. Although this distribution was originally derived for narrowband waves, it was recently proven to be valid for broadband waves as well [32]. The Tayfun distribution is considered accurate for second-order nonlinear seas where these nonlinearities are said to play a dominant role in the probability structure of a random sea state [34].

Forristall (2000) presents a nonlinear probability model based on the Weibull distribution (Eq. 2.26) fitted to second order simulations and experimental data [36].

$$P_F(\eta_c > \eta) = \exp\left[-\left(\frac{\eta}{\alpha H_s}\right)^\beta\right]$$

(2.26)

The parameters α and β were found as functions of the wave spectrum and the water depth. These were based on the degree of the degree of nonlinearity as given by the wave steepness and the Ursell number. The steepness number used in the fits is given by:

$$S_1 = \frac{2\pi}{g} \frac{H_s}{T_1^2} \tag{2.27}$$

where $T_1 = m_{000}/m_{001}$ is the spectral mean wave period. The Ursell number is a parameter which is often used to quantify the degree of nonlinearity of waves. Here, the Ursell number is given by:

$$\text{Ur} = \frac{H_s}{k_1^2 d^3} \tag{2.28}$$

where k_1 is the wave number for the frequency of the mean wave period and d is the water depth. The fits of the parameters α and β to the data can then be written as:

$$\alpha = 0.3536 + 0.2568 S_1 + 0.0800 \text{Ur} \tag{2.29}$$

$$\beta = 2 - 1.7912 S_1 - 0.5302 \text{Ur} + 0.284 \text{Ur}^2 \tag{2.30}$$

Tayfun and Fedele (2007) presented an improvement of the Tayfun model to include third-order nonlinearities [81]. Third-order nonlinearities due to quasi-resonant wave-wave interactions together with second-order nonlinearities provide a contribution to the excess kurtosis of a wave field. Comparison with 2D wave-flume experiments and 3D numerical simulations showed that this model predicted unusually large waves surprisingly well. Research has shown that third-order nonlinearities can significantly amplify the heights of 2D narrowband waves, however it should be noted that these effects are mostly investigated in terms of modulational instability for which the application to realistic sea conditions is questioned [34].

The probability of exceedance of a normalised crest by the Tayfun-Fedele model is given by:

$$P_{\text{TF}}\{\eta_c/\sigma > \xi\} \quad = \exp\left[-\frac{1}{2}\left(\frac{-1 + \sqrt{1 + 2\mu\xi}}{\mu}\right)^2\right]\left[1 + \frac{\Lambda}{64}\xi^2\left(\xi^2 - 4\right)\right] \tag{2.31}$$

where μ again is the wave steepness as presented in equation 2.24 and Λ is a function of the joint fourth-order cumulants of the surface elevation. Λ may in practice be approximated only as a function of the excess kurtosis by $\Lambda_{\text{appr}} = 8\lambda_{40}/3$, for which $\Lambda \approx \Lambda_{\text{appr}}$ is within a 3% error margin in agreement with observations for third-order nonlinear seas [34]. This excess kurtosis for a third-order nonlinear sea includes a dynamic component λ_{40}^d due to the quasi resonant nonlinear wave-wave interactions and a bound Stokes contribution λ_{40}^b so that the total excess kurtosis becomes:

$$\lambda_{40} = \lambda_{40}^d + \lambda_{40}^b \tag{2.32}$$

Due to the dynamic component being an order of magnitude smaller than the bound component we may assume its contribution to total excess kurtosis to be negligible. Therefore the excess kurtosis can be approximated as $\lambda_{40} \approx \lambda_{40}^b$. In deep water the bound component reduces to the simple form $\lambda_{40}^b = 18\mu_m$, where μ_m is given by equation 2.25.

Crest heights - STE

The Tayfun, Forristall and Tayfun-Fedele model are time-extreme models: their theoretical distributions approximate the sea surface at a given position in time. Ships and offshore structures are not pointlike objects and have a footprint area $> 0 \ m^2$. As mentioned before, research suggests that the spatial domain should be included when approximating occurrence probabilities of rogue waves. So, for calculations regarding these practical offshore applications the spatial dimension should be evaluated as well. Fedele, drawing upon Adler and Taylor (2007), presented in his 2012 paper a space-time extreme wave probability model [2] [31]. The model considers a stationary homogeneous Gaussian wave field $\eta(x, y, t)$ which is bounded by a space-time volume $V_{st} = XYD$. The model considers the average number of waves within the 3D domain N_V, waves on the 2D surfaces N_S and waves along the 1D perimeter N_B.

$$N_V = 2\pi \frac{XYD}{L_x L_y T_m} \sqrt{1 - \alpha_{xt}^2 - \alpha_{xy}^2 - \alpha_{yt}^2 + 2\alpha_{xt}\alpha_{xy}\alpha_{yt}} \tag{2.33a}$$

$$N_S = \sqrt{2\pi}\left(\frac{XD}{L_x T_m}\sqrt{1-\alpha_{xt}^2} + \frac{XY}{L_x L_y}\sqrt{1-\alpha_{xy}^2} + \frac{YD}{L_y T_m}\sqrt{1-\alpha_{yt}^2}\right) \tag{2.33b}$$

$$N_B = \frac{X}{L_x} + \frac{Y}{L_y} + \frac{D}{T_m} \tag{2.33c}$$

Where T_m is the mean zero-crossing period, L_x and L_y are the mean components of the wavelength in x- and y-direction and α_{xt}, α_{yt} and α_{xy} are the irregularity parameters of the sea state. These irregularity parameters account for correlations between space and time or space and space so that waves are not counted twice. All these parameters are given by the equations below.

$$T_m = \sqrt{\frac{m_{000}}{m_{002}}} \tag{2.34}$$

$$L_x = 2\pi\sqrt{\frac{m_{000}}{m_{200}}} \tag{2.35}$$

$$L_y = 2\pi\sqrt{\frac{m_{000}}{m_{020}}} \tag{2.36}$$

$$\alpha_{xt} = \frac{m_{101}}{\sqrt{m_{200}m_{002}}} \tag{2.37}$$

$$\alpha_{yt} = \frac{m_{011}}{\sqrt{m_{020}m_{002}}} \tag{2.38}$$

$$\alpha_{xy} = \frac{m_{110}}{\sqrt{m_{200}m_{020}}} \tag{2.39}$$

Now, the exceedance probabilities that a 3D crest height normalised with σ exceeds a certain threshold z within the 3D volume, on the 2D surfaces and along the 1D perimeter are given by:

$$P_B\{\eta_c/\sigma > z \mid B\} = P_R \tag{2.40a}$$

$$P_S\{\eta_c/\sigma > z \mid V\} = z P_R \tag{2.40b}$$

$$P_V\{\eta_c/\sigma > z \mid V\} = (z^2 - 1) P_R \tag{2.40c}$$

with P_R representing the Rayleigh distribution. The probability that the global surface maximum η_{max} exceeds threshold z (given $z \gg 1$) over the 3D volume by the space-time model (STE1) is given by:

$$\begin{aligned} P_{\text{STE1,max}}&\{\eta_{\max}/\sigma > z \mid (N_V, N_S, N_B)\} \\ &\approx \left[1 - (1-P_V)^{N_V}\right] + \left[1 - (1-P_S)^{N_S}\right] + \left[1 - (1-P_B)^{N_B}\right] \\ &\approx N_V P_V + N_S P_S + N_B P_B \approx \left(N_V z^2 + N_S z + N_B\right) P_R \end{aligned} \tag{2.41}$$

Benetazzo *et al.* (2015) extend the STE1 model to include the second-order contribution of the waves ξ as originally presented by the Tayfun model [9]:

$$\begin{aligned} P_{\text{STE2,max}}&\{\eta_{\max}/\sigma > \xi \mid (N_V, N_S, N_B)\} \\ &\approx \left(N_V z^2 + N_S z + N_B\right) P_R \end{aligned} \tag{2.42}$$

Fedele noted that for small thresholds the exceedance probability of the space-time model is larger than 1 [33]. The Gumbell asymptotic limit ensures exceedance probabilities smaller than 1 for small thresholds, resulting in equation 2.44 and 2.45 for the ST1 and ST2 model respectively. Here h_{st} is the dimensionless most probable extreme value η_{max}/σ which can be found by solving the following implicit equation:

$$\left(N_V h_{st}^2 + N_S h_{st} + N_B\right)\exp\left(-h_{st}^2/2\right) = 1 \tag{2.43}$$

Benetazzo compared stereo camera measurements with these two models where the predictions of the STE2 model were in very good agreement with the measurements [9]. Measurements over a grid of 11.2 x 11.2 m^2 already showed increased maximum crest height probability compared to time-extreme models, which could be very interesting for floating wind turbine applicability. However it should be noted that the sea state of the measurements was mild and larger waves may reduce this spatial relevance.

$$P_{\text{STE1,max}}\{\eta_{\max}/\sigma > z \mid (N_V, N_S, N_B)\} \approx \exp\left\{-\exp\left[-(z - h_{\text{ST}})\left(h_{\text{ST}} - \frac{2N_V h_{\text{ST}} + N_S}{N_V h_{\text{ST}}^2 + N_S h_{\text{ST}} + N_B}\right)\right]\right\} \tag{2.44}$$

$$P_{\text{STE2,max}}\{\eta_{\max}/\sigma > \xi \mid (N_V, N_S, N_B)\} \approx \exp\left\{-\exp\left[-\frac{\left(\xi - h_{\text{ST}} - \frac{\mu}{2}h_{\text{ST}}^2\right)\left(h_{\text{ST}} - \frac{2N_V h_{\text{ST}} + N_S}{N_V h_{\text{ST}}^2 + N_S h_{\text{ST}} + N_B}\right)}{1 + \mu h_{\text{ST}}}\right]\right\} \tag{2.45}$$

Crest-to-trough heights - STE

By extending the linear STE1 model, an expression can be formulated for a space-time crest-to-trough model. For this purpose, use is made of the Quasi-Determinism theory presented by Boccotti [13]. This linear theory states that the largest waves in a certain sea state follow a deterministic shape, based on the autocorrelation function of the wave spectrum as earlier defined by equation 2.22. Using the deterministic shape of the largest waves, the relation between crest and crest-to-trough height can be estimated as:

$$H = \sqrt{2(1 - \psi^*)} \cdot \eta \tag{2.46}$$

Here ψ^* is defined as the minimum of the autocorrelation function. Rewriting equation 2.44 using the deterministic relationship of crest and crest-to-trough gives us equation 2.47 for the STE1QD model.

$$P_{\text{STE1QD,max}}\{H_{max} > H \,|\, (N_V, N_S, N_B)\} \approx \exp\left\{-\exp\left[-\left(H - h_{\text{ST}} \cdot \sigma\sqrt{2(1 - \psi^*)}\right)\left(\frac{h_{\text{ST}} - \frac{2N_V h_{\text{ST}} + N_S}{N_V h_{\text{ST}}^2 + N_S h_{\text{ST}} + N_B}}{\sigma\sqrt{2(1 - \psi^*)}}\right)\right]\right\} \tag{2.47}$$

Previous research with space-time models

Although the space-time statistical model was introduced quite recently, research has been positive about its applicability. Cavaleri *et al.* (2016) used it as an example to explain the possibility of the Draupner rogue wave happening in a certain area of the North Sea [21]. Barbariol *et al.* explain in their 2017 paper how they implemented the model into WAVEWATCH III and present a first verification of this implementation against wave crest maxima measured on March 10, 2014 in space-time by a stereo camera placed on-board a platform in the Adriatic sea (e.g. figure 2.7). These measured space-time wave maxima are compared to the expected space-time extremes (STE) resulting from sea-state parameters as simulated by WAVEWATCH III. The results of this comparison show that the WAVEWATCH III STE model is in agreement with the observations.
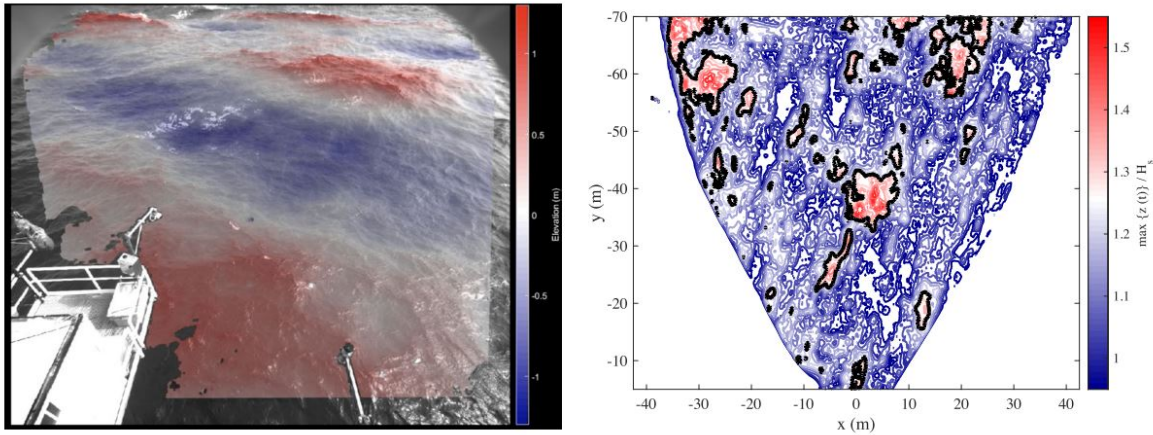
Figure 2.7: (Left panel) An example of stereo camera 3D wave measurements from the Aqua Alta platform in the Adriatic sea. (Right panel) The normalized maximum sea surface elevation at each position in the grid during time duration D. Here, the black contour illustrates areas where $H > 2H_s$. Retrieved from [10].

In their 2019 paper, Barbariol *et al.* aim to combine numerical wave model outputs and extreme statistics to study the global maximal wave heights of the world's oceans [8]. For the first time they focus on the climate features of the maximum crest and wave height in a statistical sense. A time-extreme model and space-time extreme model are used to calculate expected maxima. ERA-interim directional spectra of the world's oceans are used to estimate the statistical wave distributions. For the space-time extremes an area of 100 x 100 m^2 is chosen to represent an offshore rig. One of the conclusions of this study was that the effect of 3D geometry and the short-crestedness of realistic ocean waves over this fixed area are not negligible but that the importance of the spatial dimension lessens when wave conditions become extremer and thus more long-crested. The study did not mention from what area or from which sea states this effect reduces and how this then compares to 'regular' time-extreme models.

Benetazzo *et al.* (2020) present a study on an improvement for the phase-averaged spectral wave model WAM to incorporate extreme wave analysis with the spatio-temporal extreme model [12]. As explained before, WAVEWATCH III was already equiped with routines to estimate online spatio-temporal maximum wave heights. The study compares extreme wave outputs from the newly adapted WAM and WAVEWATCH III with stereo observations of 3D wave fields in the Adriatic and North sea. Model performance and differences between the models appear to stem mostly from the significant wave height estimation. Results from the comparison with the measurements shows that the theories used to calculate the extremes provide good model performance.

2.6. Concluding remarks - Rogue waves

In this chapter the rogue wave phenomenon was investigated. Several competing theories for the generation of rogue waves have been laid out and research into methods to predict rogue waves was briefly discussed. The goal was to evaluate what methods could possibly be used for one of the research objectives of this thesis: estimate the probability of a rogue wave hitting a SFWT.

Characteristic wave parameters of rogue seas have been investigated to find fast predictors of increased rogue wave probability, however research found no discernible link. Kurtosis seems to indicate a higher chance of rogue waves and was explored in relation to modulational instability, however validity for realistic, short-crested multidirectional seas is questioned. Hindcasting meterological conditions of known rogues increases our understanding of these waves but research in this corner is predominantly focused on explaining how a rogue could have formed in such environmental conditions and not so much on the probability of this event happening.

Statistical wave models, some which incorporate higher-order nonlinearities, appear to be best suited for this thesis. Wave height models which incorporate both space and time in particular have received much attention over the last years and are considered state-of-the-art.

According to research, the influence of area on rogue wave occurrence probability increases for low sea states and decreases for higher seas due to the waves becoming longer crested. What the authors, and others, did not research is from what area or sea state the spatial importance diminishes or increases and how this then compares to time-extreme probability models. More in general, the space-time extreme wave models have not yet been used directly with the footprints of real offshore structures to evaluate the possible increased rogue wave probability compared to time-extreme models. It will be highly interesting for the floating wind industry to know whether they should account for increased extreme wave heights based on the footprint of the structure. This is a gap in the literature that this thesis aims to answer.

3

Dynamic response spar floating wind turbine

To evaluate the effect of a rogue wave striking a SFWT, the dynamic response of the structure will be assessed. Large induced angles or nacelle accelerations will result in high loads and fatigue strain on the turbine and the blades which could be damaging [77] [67]. This chapter gives a brief overview of the dynamic response of a SFWT and an outline of the research that has already been done in evaluating the dynamic response of the turbine to gain a better understanding of how other authors have approached this case.

3.1. Dynamic response

A floating body such as a floating wind turbine has six degrees-of-freedom: surge, sway, heave, roll, pitch and yaw (see Figure 3.1). The motions of the structure are governed by a corresponding 6-DOF motion equation:

$$(\mathbf{M} + \mathbf{A})\mathbf{X}'' + (\mathbf{B})\mathbf{X}' + (\mathbf{C})\mathbf{X} = \mathbf{F}(t) \tag{3.1}$$

Here $\mathbf{M}$, $\mathbf{A}$, $\mathbf{B}$, $\mathbf{C}$ are the [6x6] matrices of the mass, added mass, damping and stiffness respectively, $\mathbf{X}$ is the [6x1] motion vector containing the displacements where $\mathbf{X}'$ and $\mathbf{X}''$ denote the first and second time derivatives containing the velocities and accelerations respectively and $\mathbf{F}(t)$ is the [6x1] external force vector containing the forces in x, y, z direction and the corresponding moments about those axes. The external force vector can be composed of the environmental forces, the mooring forces and the static restoring forces, visualised by equation 3.2 below. Regarding the environmental forces, only the wave loading will be considered in this research. The static force relates to the equilibrium of the displaced water with the structure's weight.

$$\mathbf{F}(t) = \mathbf{F}_{environmental} + \mathbf{F}_{mooring} + \mathbf{F}_{static} \tag{3.2}$$
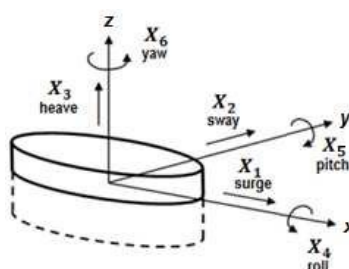
Figure 3.1: The six degrees-of-freedom of a floating body visualised by axis and directions of rotation. Retrieved from [38].

3.1.1. Wave loading

Wave loading results in a dynamic force acting on the structure due to the oscillatory nature of the waves. The induced motions as a result of this depend on the magnitude, variability and location of the force. Wave forces acting on a slender cylinder in oscillatory flow are governed by the Morison equation (Eq. 3.3) [60]. This equation is a summation of two wave force components: the linear inertial force and the quadratic drag force. Here ρ is the density of seawater, C_m and C_D are the empirical inertia and drag coefficients respectively, D is the diameter of the cylinder and $u(t)$ and $\dot{u}(t)$ are the velocity and acceleration of the wave. When viewing this equation in time it is important to note that the acceleration and velocity components are 90° out of phase due to the oscillatory motion.

$$F(t) = \frac{\pi}{4}\rho C_M D^2 \cdot \dot{u}(t) + \frac{1}{2}\rho C_D D \cdot u(t)|u(t)| \tag{3.3}$$

For a harmonic deep water wave, the velocity components $u(t)$ and $\dot{u}(t)$ can be analytically derived from the velocity potential function, which was introduced in section 2.1. By deriving this function with respect to x or z the velocity in the that direction can be found (see Eq. 2.5 and 2.6). Further integration with respect to time of a velocity component will result in its acceleration.

3.1.2. Hydrostatic stability

The law of Archimedes states that a floating body stays afloat by displacing an amount of water equal to its weight. The center of gravity of that displaced water is the center of buoyancy as illustrated by B in Figure 3.2. A small heel angle ϕ imposed on the structure shifts the center of buoyancy thereby creating a restoring moment around the center of gravity. These restoring forces are only dependent on the structure's displacements and not on time.
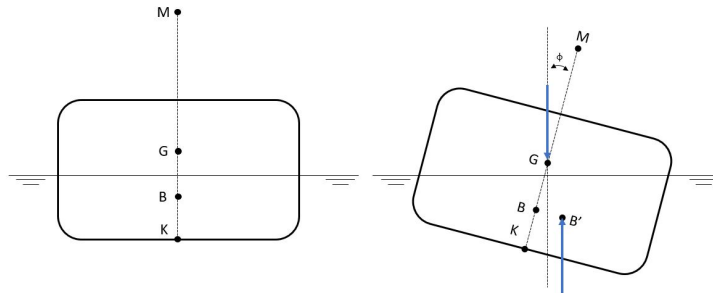
Figure 3.2: Schematic view of a floating body with center of gravity (G), center of buoyancy (B), keel (K) and metacenter (M) in neutral and slightly heeled position. Originally after [87].

3.1.3. Mooring loads

To restrict motions and keep a floating structure in place, a mooring system is used. There are two main mooring line configurations which differ in the way they counteract movement (Figure 3.3). The restoring force from catenary mooring lines comes from an increase in suspended weight of the chain which is caused by movements. Taut mooring lines act as low-stiffness springs and provide a restoring force when elongated.
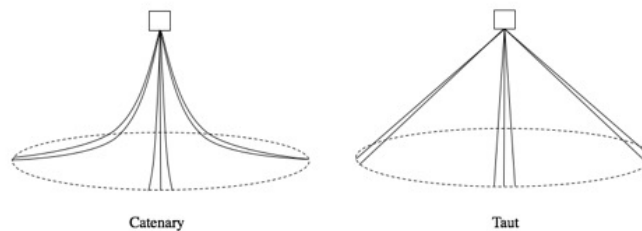
Figure 3.3: A schematic view of a catenary and taut mooring system [86]

3.2. Previous research - Dynamic response of SFWTs

A considerable amount of research has been done into the dynamic response of SFWTs. As mentioned in the introduction, the first concept that demonstrated on an industrial scale the feasibility of floating offshore wind was the spar concept. A frequently chosen concept for research into the SFWT is that as presented by Jonkman (2010) in his definition of a floating system for phase IV of the IEA Offshore Code Comparison Collaboration (OC3) [45]. This concept consists of the NREL 5MW reference turbine and a spar buoy based on the Hywind concept and scaled to accommodate a 5MW turbine, hereafter referred to as OC3-Hywind concept [47]. Below, research of three authors into the dynamic response of a SFWT is briefly evaluated.

- Aggerwal *et al.* (2012) investigated the short term extreme response of the OC3-hywind concept by a coupled wind-wave analysis by combining aerodynamic software FAST and hydrodynamic software ANSYS-AQWA. The 3-hour short term extreme responses are derived from those short time domain sets with the Global Maxima Method. With this method the maximum response of each time series is taken and then fitted against the Gumbell and Weibull distributions.

- Jeon *et al.* (2013) numerically investigated the dynamic response of a rigid floating spar substructure moored by three catenary mooring lines to unidirectional irregular waves [44]. The wind turbine itself was modelled as a tower with a lumped mass on top. Wind loading was not incorporated in the modelling. Time and frequency response of the cylindrical substructure and the tension in the mooring cables were parametrically investigated by changing the position of the cables on the substructure and their total length.

- Yu *et al.* (2015) studied the dynamic response of the OC3-Hywind concept with a numerical simulation method to evaluate the wind-wave dynamic characteristics under two different environmental conditions [88]. With the software FAST a time-domain analysis was conducted and from the results of the two load cases comparisons are made for wave and wind-wave induced loads. Also, the excited frequencies and motion coupling are investigated.

Figure 3.4: A visualisation of the OC3-Hywind concept with a 5MW wind turbine, retrieved from [45].

3.2.1. SFWT response to a rogue wave

Limited research has been done on the response of a SFWT to a single rogue wave. Here, two research papers into this subject are discussed, where increased attention is paid to the way the wave forces and the dynamic responses are calculated from the rogue wave profile.

Ruzzo et al. (2018) analyzed the dynamic response of a SFWT (OC3-Hywind) in parked conditions to a rogue wave generated by Quasi-Determinism (QD) theory [70]. From the velocity potential of the deterministic rogue wave the velocity and acceleration of the wave profile are calculated. Subsequently, the horizontal wave forces on the structure are calculated with the Morison's equation. The vertical wave force is taken as the sum of the Froude-Krylov force and the variation of buoyancy due to structure motion. The responses in heave, pitch and surge are evaluated with a 3-DOF in-house nonlinear numerical code. Only the hydrodynamics were considered, no wind forces were modelled and the turbine was assumed to be in parked conditions.

Only one sea state is assessed, where the rogue wave is assumed to be twice the height of the significant wave height. A parametric analysis is performed by varying the equilibrium position of the spar and evaluating the responses.

Qu *et al.* (2020) investigated the effect of the wave-current interaction on the generation process of a rogue wave [66]. To generate the free surface profile of a sea with a current containing a rogue wave they apply a phase-modulating algorithm. The waves and current are assumed 1-dimensional, only dependent on time. One sea state is considered against which 5 different current speeds are evaluated for the rogue wave generation. For each current speed multiple simulations are run where they report how many waves in those simulations are found to meet the rogue wave criterion of $H_{rogue} \geq 2H_s$. They aim, among other things, to illustrate differences in rogue wave generation for following and opposing currents. The wave forces are obtained from surface elevation time-histories containing the rogue waves by applying transfer functions they obtained using the software WADAM. Then, the dynamic response is evaluated by a 6-DOF in-house numerical code. The turbine is assumed to be in parked conditions and only the wind drag force working on the turbine is included. Due to the 1-dimensional nature of the waves and current, limited to one sea state, nothing about rogue wave statistics or their severity can be concluded for realistic ocean conditions.

3.3. Concluding remarks - Dynamic response SFWT

In this chapter a brief overview of the motion response of a spar-type floating wind turbine was given, as well as some previous research into this subject. Two research papers have evaluated a case of a single rogue wave hitting a SFWT. The OC3-Hywind concept is used by many authors in their dynamic analysis and is considered a valid reference SFWT design. Therefore it is the obvious choice to use this design for this thesis as well.

What stands out from the previous research into the dynamic response induced by a rogue wave is that the authors consider only one sea state, and do not say anything about the probability of such an event happening or whether this wave is the worst that could happen. Furthermore, none of the papers say something about the tower-top acceleration, which is a common industrial operational limit [67]. It would be most valuable if the dynamic response was known to rogue waves of different sizes, with each their own occurrence probability as estimated by different probability models. This way, for the first time, a risk assessment can be done on the possible danger of these rogue waves to a SFWT. This is an area where this research aims to contribute to the literature.

4

Research objectives and methodology

The objective of this thesis is to evaluate whether rogue waves could be a threat to spar-type floating wind turbines, based on their occurrence probability and the subsequent induced motions of the turbine. Some practical choices are made regarding site selection and software. California is chosen as a location of interest for floating wind energy. Also, the software program OrcaFlex is chosen for the motion response time-domain simulations. OrcaFlex is the industry standard for dynamic offshore analysis and a license was made available by IntecSea for this research.

Based on the thesis objective and the literature gaps, the following research main and sub-questions have been established:

- How threatening are rogue waves to a spar-type floating wind turbine, based on the probability of the wave occurring and the accompanying motion response?

Whereby the following sub-questions are formulated:

- How do space-time extreme wave probability models compare to time-extreme models in predicting rogue waves off the Californian coast on a spatial scale relevant to floating offshore wind turbines?

  - From what spatial scale do space-time extreme and time-extreme wave models yield significant differences?
  - What is the influence of the shape of the directional wave spectrum on the predicted rogue wave occurrence?

- What is the dynamic response of a spar-type floating wind turbine to rogue waves with different occurrence probabilities as predicted by space-time and time-extreme wave models based on OrcaFlex time-domain simulations?

4.1. Methodology

Figure 4.1 visualizes the research methodology for this thesis. Squares 1 - 6 are part of the rogue wave probability part, squares 7 and 8 are part of the dynamic response modeling and squares 9 and 10 represent the results and conclusion. These steps are briefly explained below.

1. Collect environmental data

The first step is to collect environmental data. More specifically, directional wave data is needed. Around 23 years of wave data has been evaluated, which is a significant amount since this is close to the life-span of a typical offshore structure.

2. Calculate directional spectra

With the directional wave data the spectral wave moments are calculated. From these spectral moments the input parameters for the probability models are found.

3. Evaluate the probability models

With the input parameters from the previous step, the different TE and STE probability models are evaluated in all sea states. Rogue wave crest and crest-to-trough exceedance probabilities are calculated according to their definition.

4. Compare models

Once the exceedance probabilities are calculated using the historical wave data, the models can be compared on their estimated probabilities of a rogue event. This is done for different STE area sizes.

5. Spectrum analysis

To investigate the influence of the shape of the wave spectrum, two spectral bandwidth parameters are evaluated and their relation to the estimated probabilities of a rogue event are investigated.

6. Probabilistic analysis

Using the previously calculated hourly exceedance probabilities, a method is established to estimate overall rogue wave probabilities.

7. Generate deterministic rogue wave series

Using a deterministic extreme wave theory, random wave series are generated with a deterministic rogue wave embedded. These wave series are based on real wave spectra and the most likely shape of the rogue wave.

8. Probabilistic analysis

The previously generated wave series with the embedded rogue waves are imported in OrcaFlex and simulations are run. The dynamic responses are presented as results and are used when evaluating the research questions.
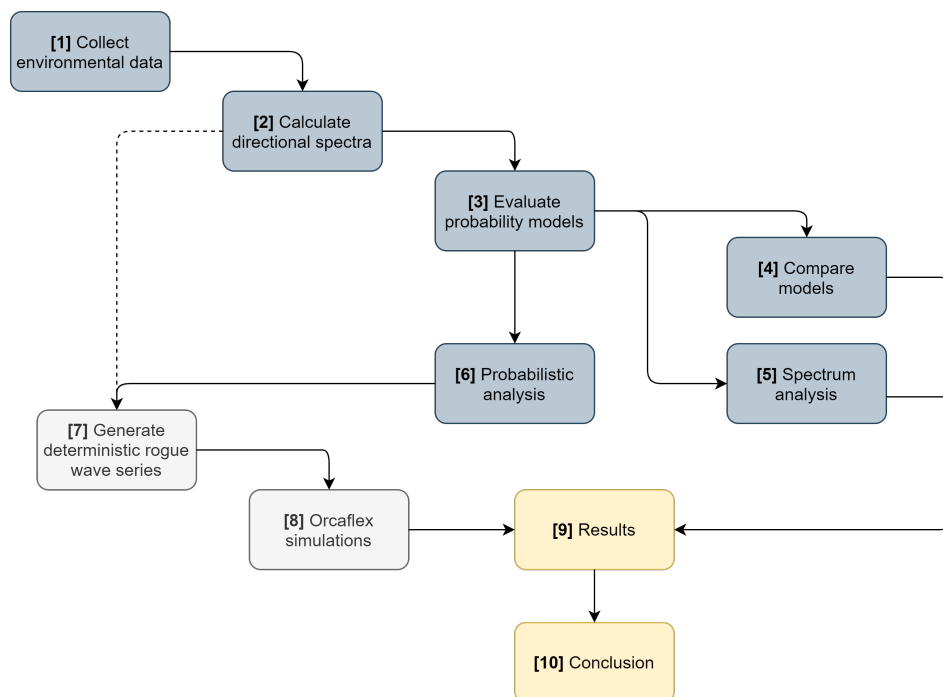
Figure 4.1: A schematic representation of the research methodology.

5

Rogue wave probability

This chapter presents the research into the rogue wave occurrence probability. Directional wave data, required to calculate the input parameters for the statistical models, is retrieved from a wave buoy located offshore California. Subsequently, this data is imported, filtered and further processed in Python. The wave climate is mapped by sorting the sea states in bins of significant wave height and mean wave period, creating a scatter diagram. The probability of a rogue wave crest and wave occurring is calculated in each sea state using the TE and STE models. With this data, the following points have been investigated:

- The influence of the area size of a STE model on the rogue wave estimate is investigated by comparing it with the estimate of the TE models. More specifically, the area size from which a STE model yields a more conservative rogue wave estimate compared to a TE model is explored.

- The influence of the shape of the wave spectrum on the estimated rogue wave probability has been investigated using two spectral width parameters.

- A long-term occurrence probability for four rogue wave and crest sizes has been calculated, using the different TE and STE models.

5.1. Wave data

The National Oceanic and Atmospheric Administration (NOAA) collects data of several wave buoys located off the coast of California. Figure 5.1 A displays a map retrieved from the NOAA website where these wave buoys are marked by coloured squares. A yellow square means the buoy is active and a red square means the buoy has been inactive for some time. Three of these buoys, operated by the National Data Buoy Center (NDBC), are directional wave buoys and are marked in figure 5.1 B by the letters A, B and C. Some properties of these buoys are summarized in table 5.1 below.

Figure 5.1: (Left) A: All wave buoys located off the Californian coast which are available through the NOAA. (Right) B: Three directional wave buoys marked by letters A, B and C. Retrieved from [63].

Buoy	Water depth [m]	Years of data available
A: St. Martin	1112	2003-2020
B: Monterey	1646	1998-2020
C: Santa Rosa Island	1005	2003-2020

Table 5.1: Properties of the three directional wave buoys.

The wave data of the NDBC buoys is not acquired from direct measurements. Accelerometers or inclinometers within the buoy measure the heave acceleration or the vertical displacement of the hull during the 20-minute data acquisition window each hour, together with sensors such as a triaxial magnetometer and/or three ortogonal angular rate sensors, which measure the hull azimuth, pitch and roll angles. Then this data is transformed from the time domain to the frequency domain by applying a Fast Fourier transform. After this transformation, response amplitude operator processing is performed on the data to eliminate hull and electronic noise so that the directional and non-directional wave parameters can be derived.

Buoy A, B and C each provide six different data files, which are sampled per hour and collected per year. The measurements taken during the 20-minute data acquisition window are assumed to represent the conditions for the whole hour. The first file contains meteorological data such as wind speed, significant wave height, dominant wave period, air pressure, etc. The second file contains the wave energy in m^2/Hz. The third until sixth file contain parameters necessary to calculate the directional wave spectrum sampled per frequency: mean wave direction, principle wave direction and Fourier constants r1 and r2, which are explained further in section 5.2. Figure 5.2 below illustrates how these six files relate to each other. Each line of data of all six files is sampled per hour. To calculate the directional wave spectrum at a specified time you would need to extract the data lines from the relevant files with the same timestamp, thus on the same line.
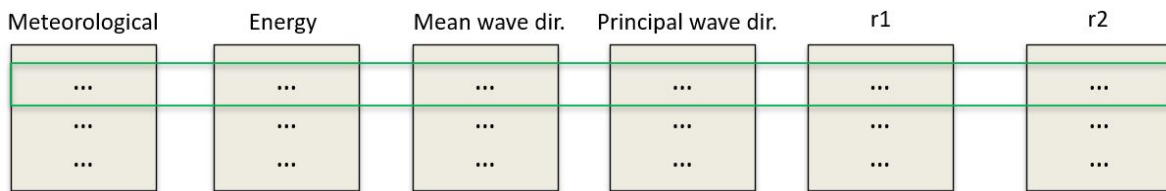
Figure 5.2: A visual representation of the data files provided by the directional wave buoys. The green line illustrates how the data lines in the files are interconnected as they are sampled at the same time intervals.

The wave buoy located in the Monterey bay has with 23 years the most wave data available. Therefore the data of this buoy is the obvious choice for this research. This is a significant amount of wave data compared to the typical life of an offshore structure [29]. All data was downloaded as .txt files so that they can be easily imported into Python.

Input from all six files is needed for calculations with the wave data. Therefore a corrupt or missing data line in one of the files (figure 5.3) means that the line with that particular time-stamp becomes useless and has to be removed in all data files. The first python script imports all wave data from the .txt files, filters the corrupt data, excludes the incomplete lines in all files, and returns the usable data. This usable data is then stored per year in a type of python data file called a 'pickle', so that it can be easily accessed later on.
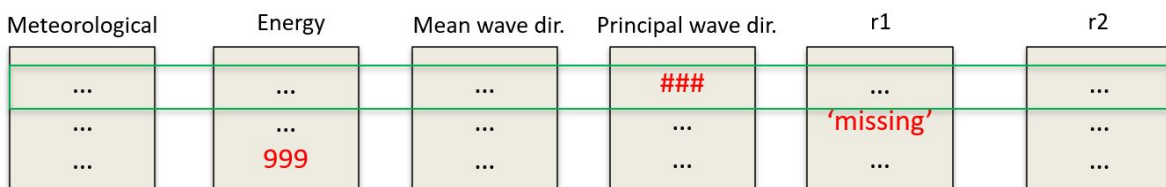
Figure 5.3: An illustrative representation of corrupt or missing data inputs in the six data files, which leads to the complete deletion of that particular line in all files.

5.2. Directional wave moments

The most widely used method to represent a directional wave spectrum is by the directional Fourier series expansion, which was originally developed by Longuet-Higgins *et al.* in 1963 [28] [55]. The parameters that govern the directional spectrum in this method are: α_1 = mean wave direction, α_2 = principal wave direction, $r1$ = first normalized directional Fourier constant, $r2$ = second normalized directional Fourier constant and C_{11} = non-directional spectral density (energy). Notice that these are the parameters provided by the wave buoys (figure 5.2).

The directional wave spectrum $S(f,\theta)$ can be written as:

$$S(f,\theta) = C_{11}(f)D(f,\theta) \tag{5.1}$$

where $D(f,\theta)$:

$$D(f,\theta) = \frac{\frac{1}{2} + r_1 \cos(\theta - \theta_1) + r_2 \cos(2(\theta - \theta_2))}{\pi} \tag{5.2}$$

is the directional spreading function without any weighing values to prevent negative energy. These weighing values can be added in an analogous manner to the cosines of equation 5.2. For this research they are chosen as 2/3 and 1/6 for the first and second cosine respectively, after [28].

In section 2.5.2 of chapter 2, various statistical wave models were introduced. Their input parameters are dependent on the directional moments of the wave spectrum. For good readability a recap of the relevant equation for these moments is presented below:

$$m_{ijk} = \iint k_x^i k_y^j f^k S(f,\theta) \, df \, d\theta \tag{5.3}$$

Here k_x and k_y are the directional wave number in x- and y-direction respectively, f the wave frequency and $S(f,\theta)$ the directional wave spectrum. Using equation 5.2, this integral can be evaluated numerically with the available buoy data. This is done for all sea states within the 23 year data set.

The buoy provides directional wave data in degrees, measured clockwise from true north. The main direction of wave propagation is chosen as the direction of the positive x-axis when calculating the spectral directional moments. Using the imported and filtered directional wave data as illustrated in the section before, the spectral directional moments for all sea states are calculated in Python.

5.3. Probability models - Python implementation

In section 2.5.2 various wave probability models were introduced. As these models and the corresponding terminology will be often used in this chapter, some extra attention will be paid to their categorization. The probability models can be classified in two ways:

- They either estimate the probability of a wave crest, or the probability of a 'complete' wave (crest-to-trough) occurring.

- They either estimate the wave occurring at a point in time (TE models) or they estimate the wave occurring within an area (STE models).

See table 5.2 below for a clear overview of the probability models with these two categories considered.

Probability models	Time extreme (TE)	Space-time extreme (STE)
Crest	Forristall, Tayfun, Tayfun-Fedele	STE2
Crest-to-trough	Naess, Rayleigh	STE1QD

Table 5.2: An overview of the probability models considered in this research and their categorization based on two above mentioned criteria.

Equations 2.21 to 2.47 presented in section 2.5.2, containing the Naess, Forristall, Tayfun, Tayfun-Fedele, STE2 and STE1QD model, together with the Rayleigh model (Eq. 2.17) have been implemented in Python. The necessary input parameters follow from the earlier calculated directional wave moments.

The crest models are defined with respect to the wave crest exceedance probability, normalized with σ (the standard deviation of the surface elevation). In this research, the significant wave height(H_s) is assumed to be $H_s = 4\sigma$, which is common practice [40]. The rogue crest definition given by equation 2.2 is redefined by substituting 4σ in place of H_s, which leads to a new rogue wave threshold of $\eta/\sigma = 5$. The crest-to-trough models are defined with respect to the wave height exceedance probability, so no substitutions have to be made regarding the crest-to-trough rogue threshold (Eq. 2.1).

Remember from chapter 2 that the rogue waves are defined using one of the two size criteria, which have to be met within a 20-minute time duration for the waves to be considered rogue. Therefore, all probabilities which will be calculated will be exceedance probabilities of the rogue wave threshold, within 20 minutes.

In high sea states (large H_s), wave lengths will become long and they will become wide crested (perhaps a couple hundred meters). Since the TE and STE probability models will be compared in multiple sea states, including these high ones with the long waves, it could be that quite a large area is required before significant differences will be observed between some models. According to Benetazzo *et al.*, the area evaluated with the STE models should be smaller than $100 \times 100\text{m}^2$ for the unbounded models to stay accurate and prevent theoretical unlimited growth [11]. Therefore, $100m$ has been chosen as upper limit for the STE area sides.

Figure 5.4 gives a schematic representation of how the different Python scripts used to evaluate the wave probability models relate to each other. First the wave data is imported and filtered. Then this filtered data is stored in a pickle data file. The script 'Moments & parameters' imports this data, calculates the spectral directional moments and subsequently the model input parameters. These input parameters are then again stored in a pickle. The script 'Probability models' imports these parameters and evaluates the probability models for each available sea state within the data set. The calculated probability data is then again stored in a pickle so that it can be easily accessed by later scripts using it for comparisons and other calculations. As they serve a core function in the probability analysis, these three Python scrips are presented in Appendix F.
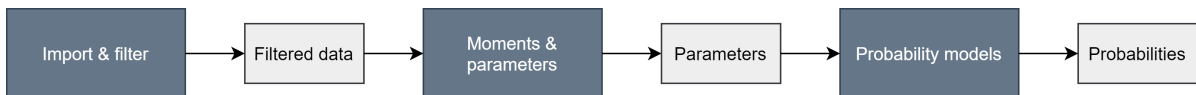
Figure 5.4: A schematic representation of the different Python scripts used to evaluate the probability models using the wave data.

5.4. Wave climate - scatter diagram

In order to compare the statistical models in different sea states it is desired to sort the sea states in bins. To do so, a scatter diagram with the significant wave height and the mean zero-crossing period is made (figure 5.5). The average amount of waves (N) which have occurred in each sea state are calculated using the mean zero-crossing wave period and are subsequently stored in their respective bin. From this diagram, frequently occurring combinations of H_s and T_m can be chosen as a criterion to compare the models on. Also, this diagram can be used to address the occurrence probability of a certain sea state.

At the end of section 5.1 the process of excluding corrupt data lines was introduced. Due to the fact that a single corrupt line in one of the 6 interdependent data files leads to the exclusion of that line in all 6 data files, quite some data lines had to be removed in order to prepare the data for the calculations. Also, in the first file from 1998, the first sampled date is not January 1st like in the others, but June 19th. If no data lines had been excluded, we would have had a total of 197568 hourly sea states. After the corrupt data exclusion there are 170845 hourly sea states left. In the following sections and chapters, these 170845 hourly sea states will be addressed as 'the data set' and the included years (1998-2020) might be given as reference to the time period. This exact number will be revisited when return periods are considered in calculations, due to the influence it will have on the overall probability.
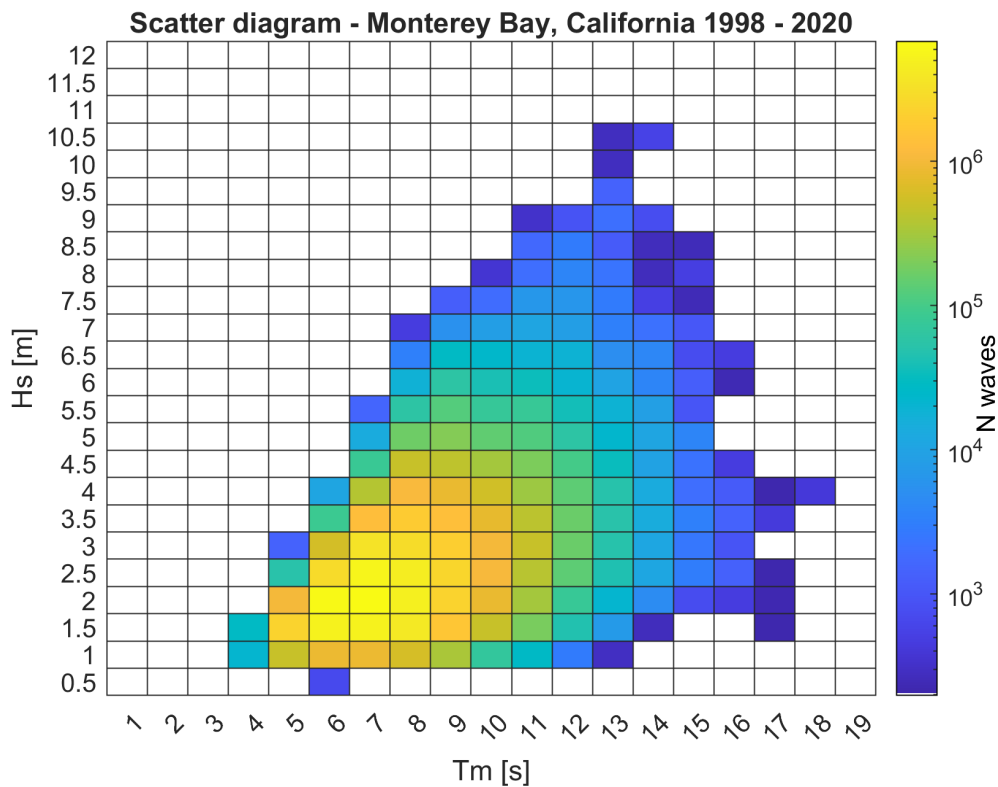
Figure 5.5: Scatter diagram of the significant wave height and the mean zero-crossing wave period. Data set from Monterey Bay from 1998-2020.

5.5. Influence of spatial scale on predicted rogue wave probability

In this section, the TE and STE models are compared to each other, based on their estimated probability that a rogue crest or wave (crest-to-trough) will occur. The comparisons will be done with ratios where the probability estimated by the STE model is divided by that of the TE model, in a range starting with no spatial component (X=0, Y=0) to A = 100×100m^2, to investigate the influence of the spatial scale on the probability of a rogue wave event. Especially interesting is the area size which will result in the STE model estimating higher probabilities of a rogue wave occurring compared to the TE model.

5.5.1. Method

Several comparisons are made between TE and STE probability models. These comparisons are made for 10 different sea state combinations of H_s & T_m, based on figure 5.5. These combinations of H_s & T_m are chosen as follows:

First, for each possible H_s range of figure 5.5 (such as $2 < H_s \leq 2.5$, $2.5 < H_s \leq 3$, etc.) the H_s & T_m bins containing the most waves (N) are picked out. Since there are 21 rows with sea state entries, this comes down to 21 bins. This way, frequently occurring H_s & T_m combinations are identified. Then, from those frequently occurring combinations, 10 bins were chosen as sea states to compare the models in.

The STE and TE models are compared on their estimated exceedance probability of a rogue wave event within a 20-minute time series. This is $P(\eta/\sigma \geq 5)$ for a rogue wave crest and $P(H/H_s \geq 2)$ for a rogue wave, after equation 2.2 and 2.1 respectively. Within each of the 10 previously chosen sea state bins, the maximum exceedance probability of the rogue threshold is identified for each wave model. These are the highest exceedance probabilities per bin and are chosen as a way to represent a worst-case scenario in terms of rogue wave occurrence. The probability estimated by a STE model is then divided by that of a TE model, in a range starting with no spatial component (X=0, Y=0) to A = 100×100m^2, in each sea state.

By dividing the probability of the STE model by that of the TE model their difference ratio is easily obtained. An important number here is '1', since a result lower than '1' indicates that the TE model estimates a higher probability and a result larger than '1' indicates that the STE model estimates a higher probability. The following comparisons are made and presented in the figures below:

Comparisons rogue crest models

- STE2 - Forristall model (figure 5.6)

- STE2 - Tayfun model (figure 5.7)

- STE2 - Tayfun-Fedele model (figure 5.8)

Comparisons rogue wave models

- STE1QD - Naess model (figure 5.9)

- STE1QD - Rayleigh model (figure 5.10)

5.5.2. Results - Wave crest models

Figure 5.6, 5.7 and 5.8 present the comparisons between the STE2 model and the Forristall, Tayfun and Tayfun-Fedele models respectively. The area size is reported on the x-asis in terms of $\sqrt{xy}$ as a way to indicate the length of the sides of the squared area. An area size of $\sqrt{xy} = 10m$ means that the considered area was 10×10m^2. Some observations regarding these figures:

- A first observation shows that as the area size increases, the relative difference between the TE and STE models increases. This is of course what was expected.

- The values on the y-axis show the ratio difference between the STE and TE model, where higher values mean a larger difference. Regarding the TE models, the Forristall model appears to estimate the lowest probabilities, followed by the Tayfun model and Tayfun-Fedele model estimates the highest rogue crest probabilities.

- Figure 5.6 and 5.7 clearly show a decreasing trend of the relative difference between the estimated rogue crest probability by the STE and TE model, as the sea state becomes higher. This can be explained by the fact that as waves become higher, they generally become longer crested, thus decreasing the amount of unique waves that exist within or on the borders of the considered area and therefore decreasing the influence of the spatial dimension.

- Figure 5.8 also shows traits of the above mentioned trend, though it is less pronounced. Many of the curves in figure 5.8, from a sea state of $4 < H_s \leq 4.5m$ and higher, are somewhat clustered together. This could be explained due to the fact that the Tayfun-Fedele model is an extension of the Tayfun model where an extra parameter, the excess kurtosis, is taken into account to incorporate 3rd order surface nonlinearities.

What is interesting to see is that when the area sides X and Y approach 0, the STE2 model still approximates higher exceedance probabilities of a rogue crest occurring than the Forristall and Tayfun model. This can be clearly seen in both figure 5.6 (b) and 5.7 (b). The black dashed line denotes the y-value threshold of '1', indicating whether the STE or the TE model estimates a higher probability. From an analytical point of view one might expect the STE2 and Tayfun model to converge at $\sqrt{xy} = 0m$, since the Tayfun crest definition was used to extend the linear STE1 model to the nonlinear STE2 model. However, when formulating the exceedance probability function of the STE model, the asymptotic Gumbel limit was used to ensure probabilities lower than '1' for small η/σ thresholds. Therefore these two models do not converge as the area sides approach $0m$.

Only the Tayfun-Fedele model, in two sea states, slightly estimates a higher rogue crest exceedance probability as the area sides X and Y approach 0. However, this difference can be considered quite insignificant, as from an area of approximately $2 \times 2m^2$ onwards the STE2 model again predominates. Due to the dependence of the Tayfun-Fedele model on the excess kurtosis of the wave field, this exact area size may of course vary. Nevertheless, since the area ($2 \times 2m^2$) is so small, and the Tayfun-Fedele model is the most conservative TE wave crest model, one could conclude that when rogue wave crests are considered for structures like floating offshore wind turbines, inclusion of the spatial dimension using the STE2 model will provide the most conservative estimate in all sea states.

(a)

(b)
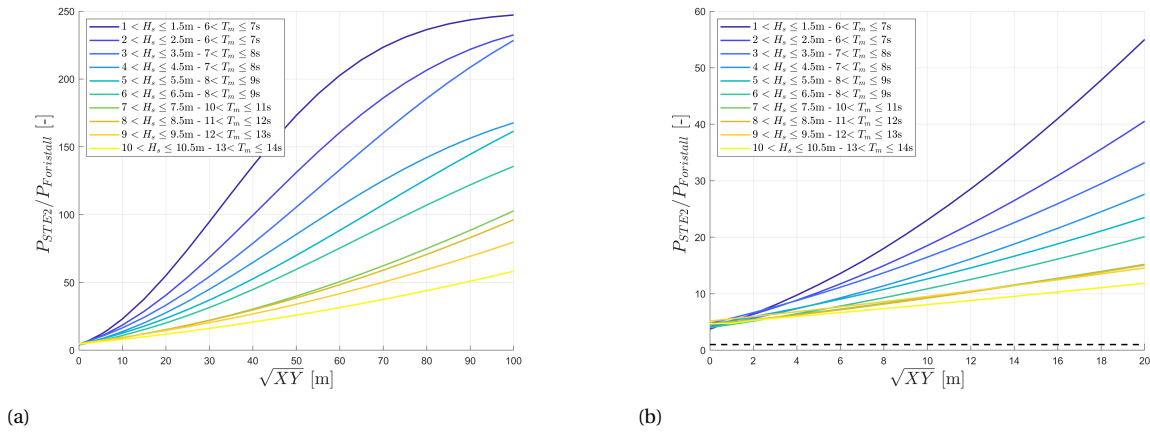
Figure 5.6: Comparison of the STE2 and Forristall estimate of $P(\eta_{max}/\sigma \geq 5 \mid D)$ with D = 1200s. (a) Area sizes ranging from no spatial component (X=0,Y=0) to $100 \times 100m^2$. (b) Area sizes ranging from no spatial component (X=0,Y=0) to $20 \times 20m^2$. The horizontal black dashed line visualises a y-ratio of '1'.

(a)   (b)
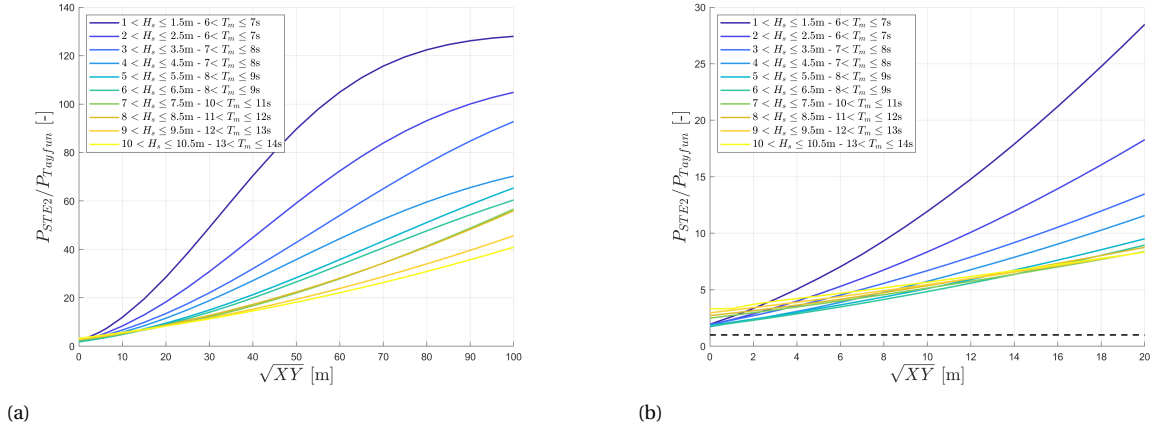
Figure 5.7: Comparison of the STE2 and Tayfun estimate of $P(\eta_{max}/\sigma \geq 5 \,|\, D)$ with D = 1200s. (a) Area sizes ranging from no spatial component (X=0,Y=0) to 100×100m^2. (b) Area sizes ranging from no spatial component (X=0,Y=0) to 20×20m^2. The horizontal black dashed line visualises a y-ratio of '1'.

(a)   (b)
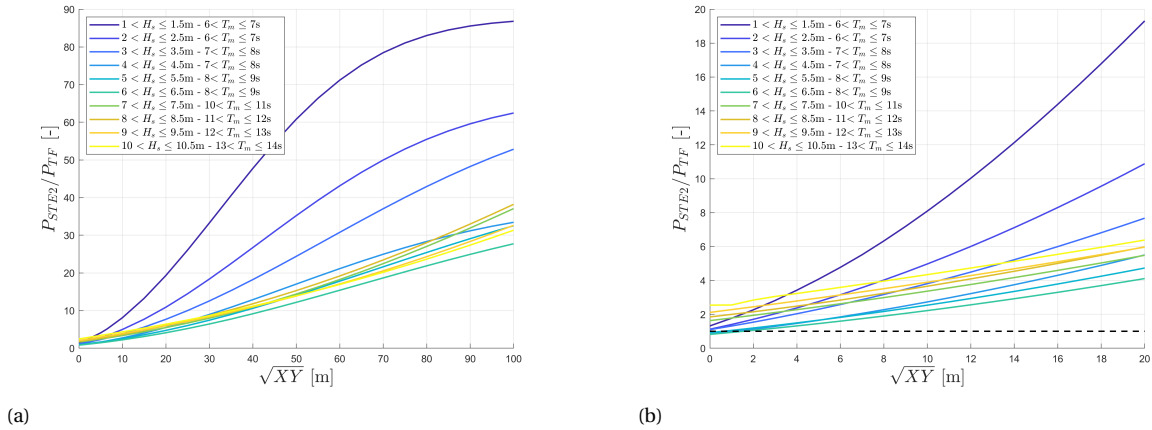
Figure 5.8: Comparison of the STE2 and Tayfun-Fedele estimate of $P(\eta_{max}/\sigma \geq 5 \,|\, D)$ with D = 1200s. (a) Area sizes ranging from no spatial component (X=0,Y=0) to 100×100m^2. (b) Area sizes ranging from no spatial component (X=0,Y=0) to 20×20m^2. The horizontal black dashed line visualises a y-ratio of '1'.

5.5.3. Results - Wave crest-to-trough models

Figure 5.9 and 5.10 present the comparisons of the STE1QD model with the Naess and Rayleigh model respectively. Again clearly visible is the increasing difference in estimated exceedance probability of the rogue wave threshold between STE and TE model as the area increases, and the declining relative difference as the sea state becomes higher. Notice also that both in figure 5.9 and 5.10 the lines belonging to the two lowest sea states seem to approach a maximum as the area increases. This is because in those sea states the STE1QD model estimates an exceedance probability of almost '1' from a certain area size onwards.

Figure 5.9 (b) shows that as the area sides X and Y decrease to 0, the STE1QD model still predominates the Naess model. This can again be seen by looking at the black-dashed line symbolizing $y = 1$, which is never crossed by any of the curves. In figure 5.10 (b) it is observed that for a small area (approximately <2×2m^2), the Rayleigh model always estimates a higher rogue wave probability than the STE1QD model, regardless of the sea state. As the area size increases, the STE1QD model starts to predominate, and from an area size of around 12×12m^2 onwards the STE1QD model estimates higher rogue wave probabilities even in the highest sea states. This is interesting because the Rayleigh model is generally regarded to be conservative (e.g. see [57]). These results would indicate that when rogue waves are evaluated for an offshore structure with a footprint larger than 12×12m^2, inclusion of the spatial dimension using the STE1QD model will provide the most

conservative estimate in all sea states.

(a)   (b)
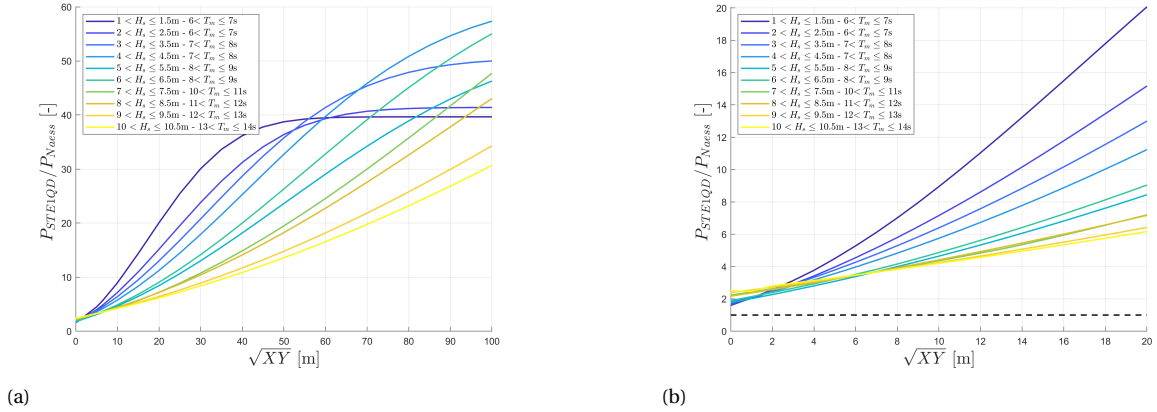
Figure 5.9: Comparison of the STE1QD and Naess estimate of $P(H_{max}/H_s \geq 2\,|\,D)$ with D = 1200s. (a) Area sizes ranging from no spatial component (X=0,Y=0) to 100×100m^2. (b) Area sizes ranging from no spatial component (X=0,Y=0) to 20×20m^2. The horizontal black dashed line visualises a y-ratio of '1'.

(a)   (b)
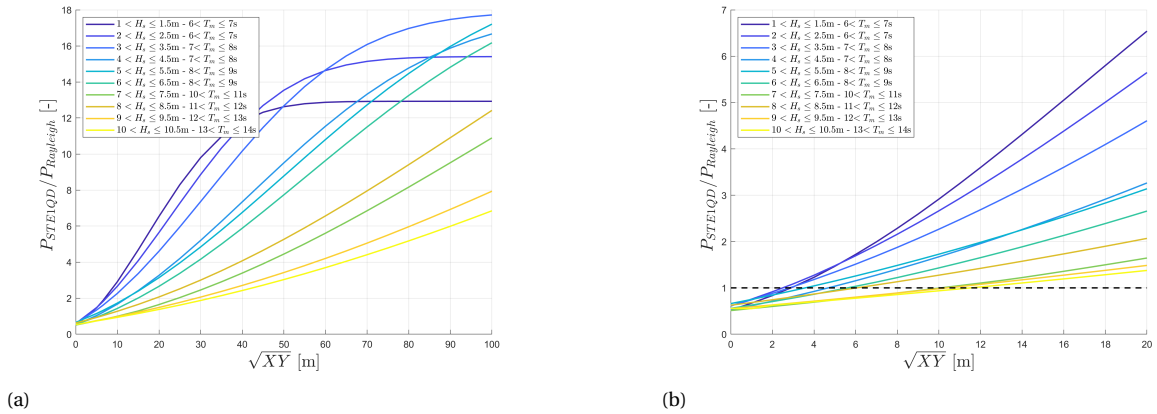
Figure 5.10: Comparison of the STE1QD and Rayleigh estimate of $P(H_{max}/H_s \geq 2\,|\,D)$ with D = 1200s. (a) Area sizes ranging from no spatial component (X=0,Y=0) to 100×100m^2. (b) Area sizes ranging from no spatial component (X=0,Y=0) to 20×20m^2. The horizontal black dashed line visualises a y-ratio of '1'.

5.6. Influence of wave spectrum on rogue wave probability

To investigate the influence of the wave spectrum on the predicted rogue wave probability, two spectral width parameters are investigated. These spectral bandwidth parameters, ϵ (Eq. 5.4) and ν (Eq. 5.5), range between 0 and 1. As their values approach '0' it indicates that the wave energy is concentrated around the peak frequency and the spectrum is considered narrow (figure 5.11a) . When their values approach '1' it indicates that the wave energy is spread out over multiple frequencies, giving a wide spectrum (figure 5.11b). Notice the irregular shape of the wide wave spectrum together with the existence of negative crest heights due to the energy being spread out over multiple frequencies.

$$\epsilon = \sqrt{1 - \frac{m_2^2}{m_0 m_4}} \qquad (5.4) \qquad\qquad \nu = \sqrt{\frac{m_2 m_0}{m_1 m_1} - 1} \qquad (5.5)$$
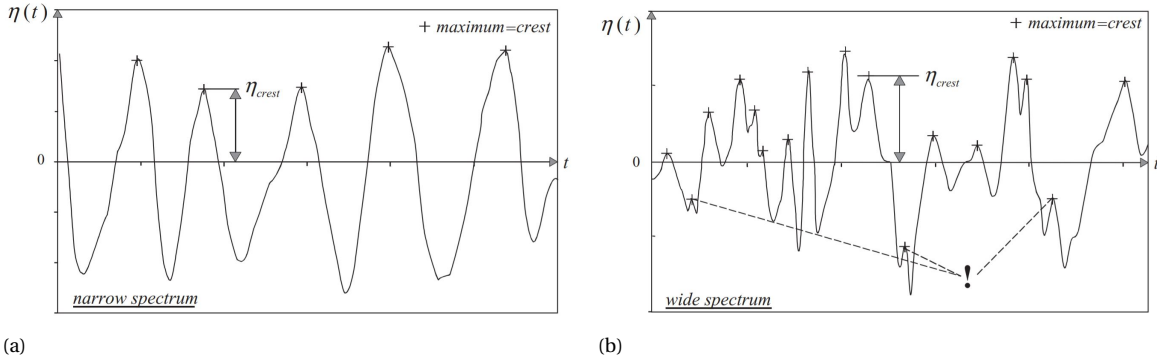
Figure 5.11: A representation of a narrow wave spectrum (a) and a wide wave spectrum (b). Retrieved from [40].

This comparison uses the previously calculated exceedance probabilities of the two rogue thresholds within a 20-minute duration. Additionally, the two spectral width parameters are evaluated in each sea state. Then the exceedance probabilities of all considered sea states are matched with their corresponding spectral width values in order to create scatter plots.

Regarding the two spectral parameters, ν is preferred to ϵ since the calculation of ϵ depends on the 4th spectral moment m_4 (see equation 5.4). Because m_4 is a high-order moment, it is sensitive to noise in the spectrum at the high frequencies. Therefore, the value of ϵ depends not only on the shape of the wave spectrum, but also on errors, the high frequency cut-off or nonlinear distortions in the high-frequency part of the wave spectrum [40].

5.6.1. Results - Wave crest models

Figure 5.12 to figure 5.15 present the scatter plots of the four considered wave crest probability models and the two spectral width parameters. Each dot represents a 1 hour sea state, with on the vertical axis the exceedance probability of the rogue threshold in 20 minutes, and on the horizontal axis the spectral parameter ϵ or ν. The trendlines are based on a polynomial fitted to the data using a MATLAB Polyfix function [6]. Appendix A presents a brief trendline shape comparison for both the crest and crest-to-trough models.

For all four models, an increase in estimated exceedance probability of the rogue crest threshold can be observed as the spectral parameters ϵ and ν decrease. This indicates that the considered probability models estimate a higher chance of rogue wave crests occurring as the wave spectrum becomes more narrow. The coefficient of determination, R^2, is presented in the figure descriptions. This coefficient represents a 'goodness-of-fit' of the trendline for all data points and ranges between 0 and 1. Due to the very large data size with a wide spread, these values are rather low. This means that the presented trendline is not an exact representation of the data, but should be regarded more like an indication.
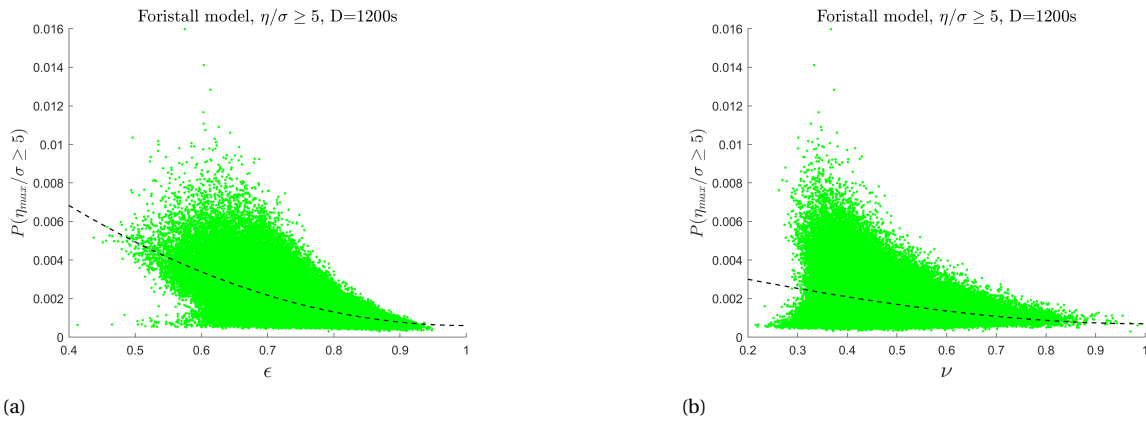
Figure 5.12: Exceedance probability of the rogue wave threshold $P(\eta/\sigma \geq 5)$ for D = 20 minutes as estimated by the Forristall model, plotted against (a) spectral width parameter ϵ with 3rd order trendline (R^2 =0.3577) and (b) spectral width parameter ν with 2nd order trendline (R^2 = 0.0865).
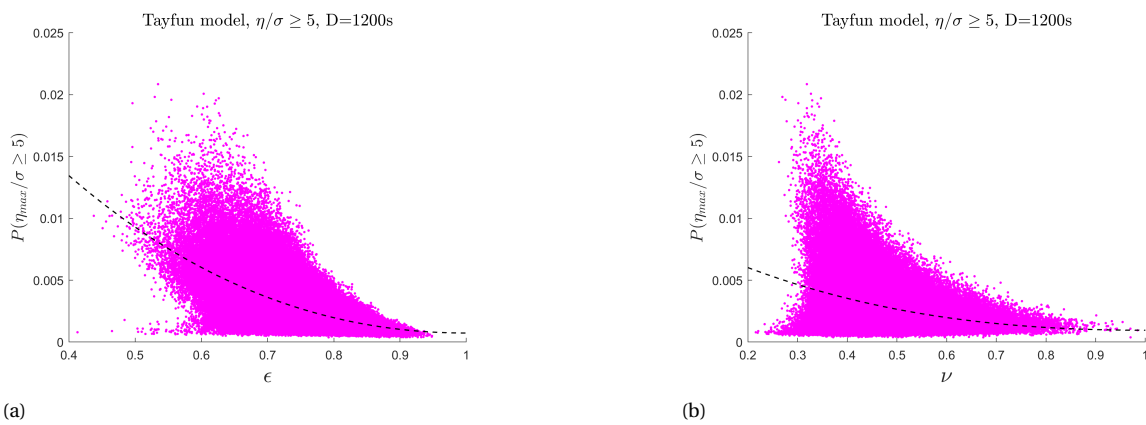
Figure 5.13: Exceedance probability of the rogue wave threshold $P(\eta/\sigma \geq 5)$ for D = 20 minutes as estimated by the Tayfun model, plotted against (a) spectral width parameter ϵ with 3rd order trendline (R^2=0.3479) and (b) spectral width parameter ν with 3rd order trendline (R^2=0.1055).
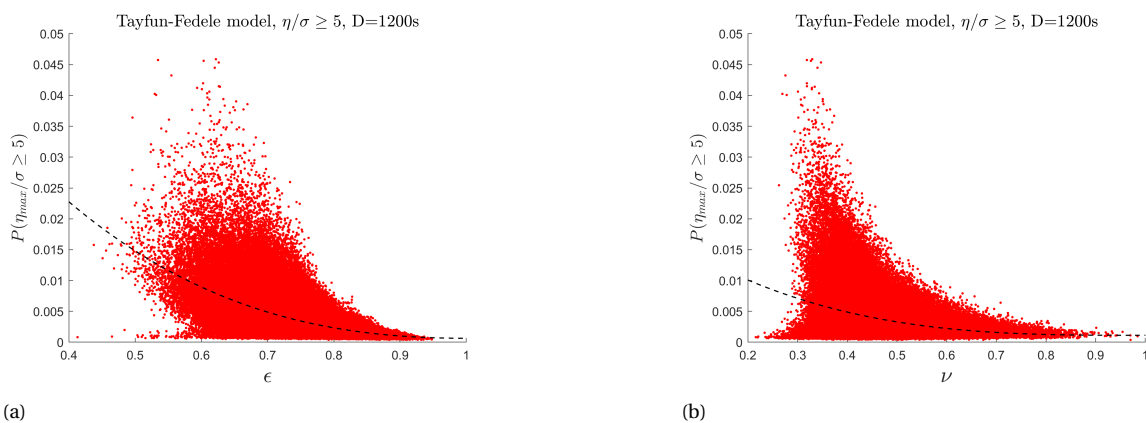
Figure 5.14: Exceedance probability of the rogue wave threshold $P(\eta/\sigma \geq 5)$ for D = 20 minutes as estimated by the Tayfun-Fedele model, plotted against (a) spectral width parameter ϵ with 3rd order trendline (R^2 =0.3012) and (b) spectral width parameter ν with 3rd order trendline (R^2 =0.1093).
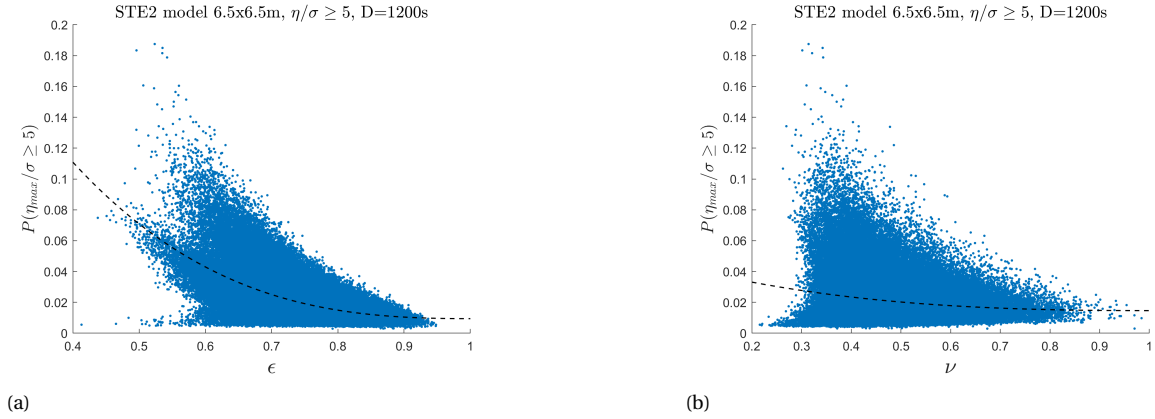
Figure 5.15: Exceedance probability of the rogue wave threshold $P(\eta/\sigma \geq 5)$ for D = 20 minutes as estimated by the STE2 model with A=6.5×6.5m^2, plotted against (a) spectral width parameter ϵ with 3rd order trendline ($R^2 = 0.3296$) and (b) spectral width parameter ν with 3rd order trendline ($R^2 = 0.0301$).

5.6.2. Results - Wave crest-crest-to-trough models

Figure A.9 to figure 5.18 present the scatter plots of the three considered crest-to-trough wave probability models. See appendix A for a brief trendline shape analysis. In the scatterplot where the Naess model is considered, figure A.9, no clear trend regarding the spectral parameters and the rogue wave probability can be observed. The Naess model is dependent on two parameters: the ratio of the inquired wave height to the significant wave height, and the minimum value of the underlying autocorrelation spectrum. The minimum value of the autocorrelation spectrum has no direct connection to ϵ and ν, which can explain the absence of a trend.

In the same sense, a clear trend for the Rayleigh distribution (figure 5.17) is difficult to distinguish. For spectral parameter ϵ, a distinctive positive slope can be observed as ϵ goes to 0. However, since the Rayleigh distribution is only dependent on the significant wave height, this behaviour is most probably due to the mean zero-crossing period T_m, defined as $\sqrt{m_0/m_2}$, which is used to calculate the amount of waves N in the 20-minute time interval. The second spectral moment m_2 can be found to the power of 2 in the numerator of the fraction in equation 5.4. A relatively high m_2 will result in a lower T_m and a low value of ϵ. This lower value of T_m results in a high amount of waves in the 20-minute time interval, resulting in increased rogue wave probability.

Lastly, the STE1QD model trendline appears to slope upwards when ϵ is regarded, though overall it cannot be said that the shape of this data brings forward a robust trendline. This model is a linear STE model which was extended using the QD theory. Due to the dependence on many parameters governed by spectral moments and the unclear trendline, a clear conclusion regarding the influence of the spectral parameters on the estimated rogue probabilities cannot be drawn.

5.6.3. Relation to previous literature

In section 2.5.1, a study from Cattrell *et al.* was presented where data from 80 wave buoys was used to find possible connections between characteristic wave parameters and rogue waves [19]. They reported that the normal seas and rogue seas had similar ν values, but that higher ν values showed increased rogue crest and wave probability. In the case of the rogue crests, those results differ from the results from this section. Regarding ϵ, the rogue crests appeared to have a higher occurrence probability in seas with a more narrow bandwidth, which is in accordance with the results of this section.

Similarly, Christou and Ewans (2014) also investigated characteristic sea parameters in relation to rogue waves, but with measurements from fixed sensors on offshore platforms [22]. They did not differentiate between crest and crest-to-trough height in their bandwidth analysis. In contrast to Cattrell, they reported for ν that the rogue waves occurred slightly more frequently in narrowband waves, which is more in accordance to the results of this study. For ϵ they report a similar distribution for normal waves and rogue waves.
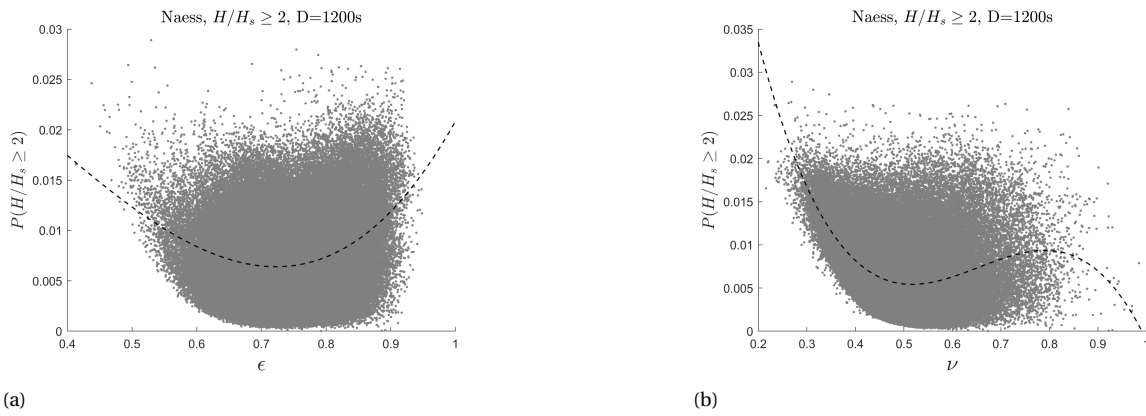
Figure 5.16: Exceedance probability of the rogue wave threshold $P(H/H_s \geq 2)$ for D = 20 minutes as estimated by the Naess model, plotted against (a) spectral width parameter ϵ, trendline is 3rd order, $R^2 = 0.0726$ and (b) spectral width parameter ν, trendline is 3rd order, $R^2 = 0.2498$.
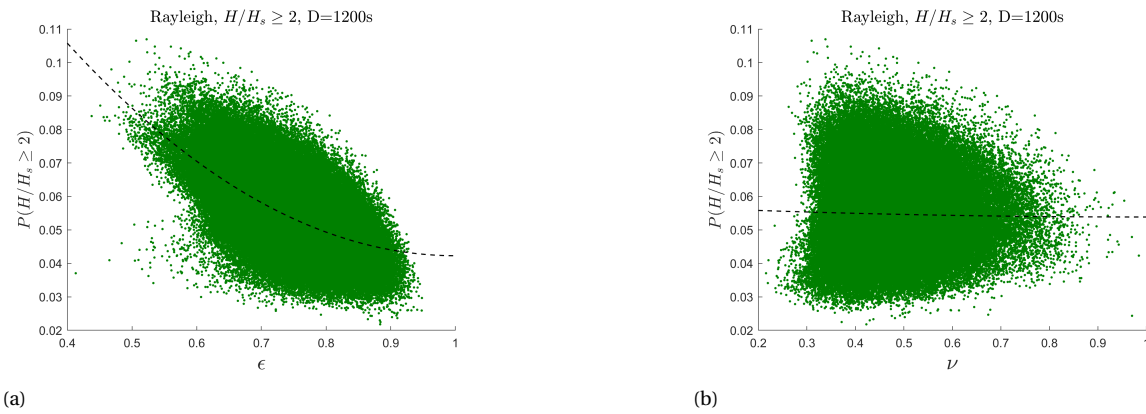
Figure 5.17: Exceedance probability of the rogue wave threshold $P(H/H_s \geq 2)$ for D = 20 minutes as estimated by the Rayleigh model, plotted against (a) spectral width parameter ϵ with 2nd order trendline ($R^2=0.3471$) and (b) spectral width parameter ν with 2nd order trendline ($R^2=5.77e-4$).
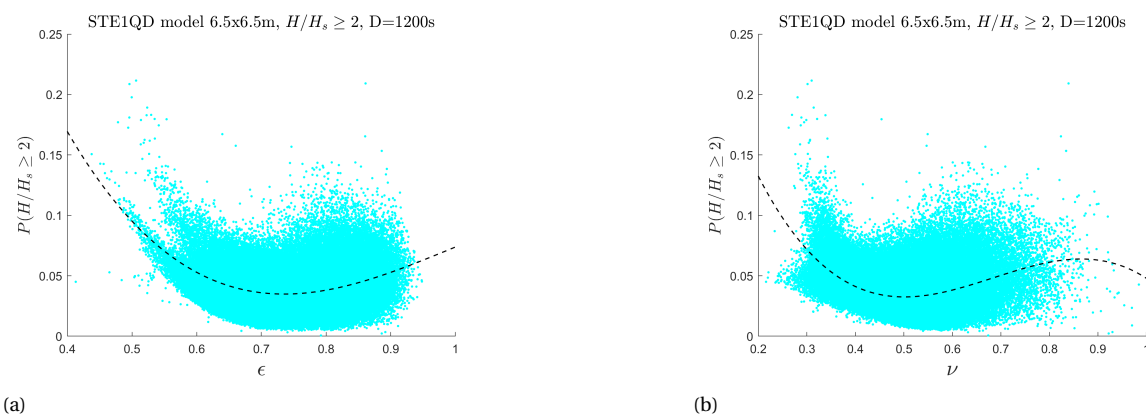
Figure 5.18: Exceedance probability of the rogue wave threshold $P(H/H_s \geq 2)$ for D = 20 minutes as estimated by the STE1QD model with A=6.5×6.5m^2, plotted against (a) spectral width parameter ϵ with 3rd order trendline ($R^2 = 0.1106$) and (b) spectral width parameter ν with 3rd order trendline ($R^2 = 0.1881$).

5.7. Long-term rogue wave probability

To estimate the long-term rogue wave probability, both the short-term rogue statistics and the sea state occurrence probability have to be taken into account. In figure 5.5 the wave climate was visualised by a scatter diagram sorting the average number of waves into bins of significant wave height and mean zero-crossing period. For the purpose of calculating the overall rogue probability this scatter diagram is slightly modified, such that instead of the amount of waves it now shows the amount of 1-hour sea states sorted in each bin (figure 5.19). With this scatter diagram the expected occurrence of a certain sea state in the duration of the data set can be addressed, while at the same time serving as a sort criterion to estimate average rogue probabilities per bin.

Note that in section 5.4 the exact amount of usable sea states after the corrupt data exclusion was introduced. This corresponds to 170845 hourly sea states, which converted to years is 19.5. This means that an overall probability of a rogue wave occurring within the data set corresponds to this return period of 19.5 years, which will also be used when extrapolating to longer return periods.
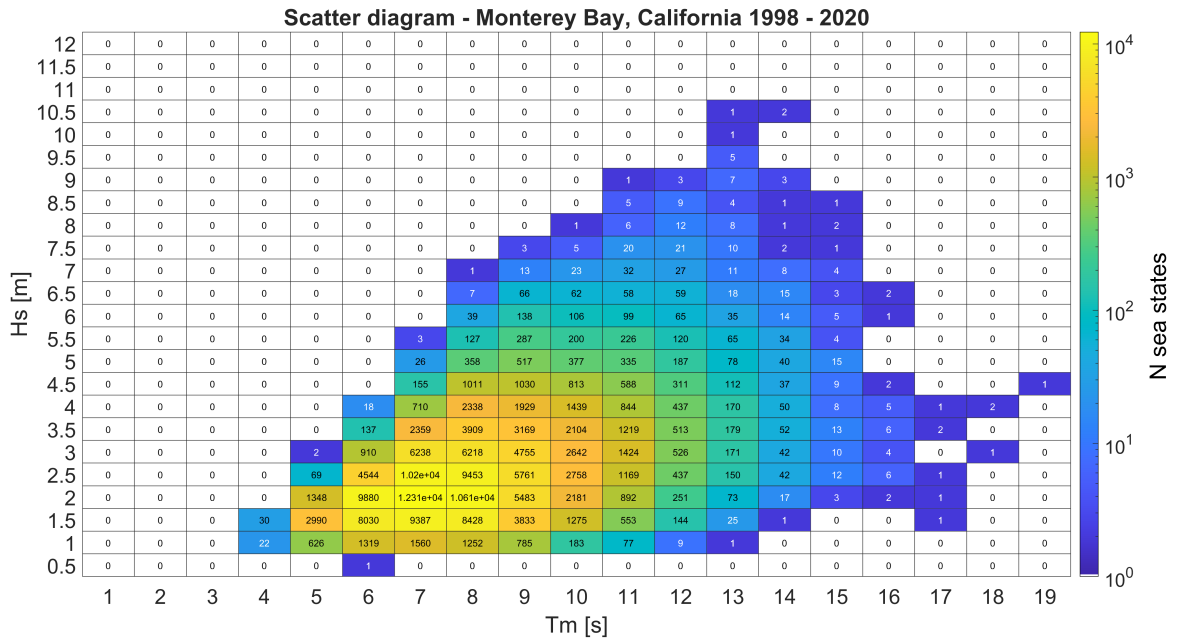
Figure 5.19: Scatter diagram of the significant wave height and the mean zero-crossing wave period. Numbers in the respective bins correspond to the amount of 1-hour sea states found in the data set. Data from Monterey Bay from 1998-2020.

First, rogue size thresholds are established for both the crest and the crest-to-trough height. Since we are only interested in the very large waves, the four most upper rows containing sea state entries of figure 5.19 are investigated. For each of these rows the average significant wave height is calculated to serve as benchmark for the thresholds. Table 5.3 below presents these H_s averages, together with the corresponding rogue thresholds.

Scatter diagram row H_s [m]	Avg H_s [m]	η_{rogue} [m]	H_{rogue} [m]
10 - 10.5	10.31	12.89	20.62
9.5 - 10	9.92	12.40	19.84
9 - 9.5	9.13	11.41	18.26
8.5 - 9	8.78	10.98	17.56

Table 5.3: Average significant wave height and corresponding rogue thresholds of the four rows containing the highest sea states of the scatter diagram.

In theory, one could state that in each of the sea states found in figure 5.19 a rogue wave could form which will exceed a threshold from table 5.3, given enough time. Though this is extremely unlikely, it will be the starting

point of this calculation. To evaluate the probability that <u>at least one wave</u> will exceed one of the thresholds, one can calculate the probability that in all sea states <u>no waves</u> will exceed the threshold ($P_{no\,rogue}$). The probability of at least one wave exceeding a rogue threshold is then easily found by evaluating $P_{rogue} = 1$-$P_{no\,rogue}$.

Crest height and crest-to-trough height exceedance probabilities $P(\eta/\sigma \geq \xi \mid D)$ and $P(H/H_s \geq z \mid D)$ for a large range of ξ and z values have been calculated in all sea states, using the different probability models. The duration D is 20 minutes to comply with the rogue definitions. In a low sea state the threshold ξ or z which has to be exceeded in order to produce a rogue wave large enough to surpass the thresholds established in table 5.3 will be much higher compared to those of a high sea state. The probability of exceeding a high threshold ξ or z rapidly decreases as the threshold grows larger. This means that, having the scatter diagram in mind, from a certain sea state range downwards the contribution of those sea states to the exceedance probability of the rogue thresholds will be nihil.
<u>Note</u> that only waves which classify as rogue are of interest to this calculation. If in a sea state the threshold is not considered rogue, then that sea state is excluded from the calculation.

Each bin of figure 5.19 is evaluated separately in terms of their exceedance probability of the rogue thresholds. This is done by first calculating the average H_s of the sea states within that bin. This average H_s is then used to determine the average threshold ξ or z that a sea state within that particular bin will have to exceed in order to exceed the rogue thresholds. Using these ξ and z values an average exceedance probability is calculated per bin. This is done by taking the average of the exceedance probabilities of all the sea states within the bin evaluated at that average ξ or z value. To check whether these probabilities may directly be averaged, or that the input parameters should be averaged, a comparison between these two methods is made in selected sea states where $H_s \geq 7.5m$, see Appendix B. From this comparison it is concluded that since the difference in results is minimal, the probabilities will be directly averaged as this is the fastest method. Now, to calculate the probability of at least one wave exceeding a threshold within the data set, the following equation will be evaluated:

$$P(rogue) = 1 - \left(\bigcap_{i=1}^{N} P(no\,rogue \mid Ss_i) \right) \qquad (5.6)$$

Where the $P(no\,rogue \mid Ss_i)$ is defined as the average probability of no wave exceeding the rogue threshold in that particular sea sate (Ss_i), to the power K, which represents the number of 20-minute time series found in the respective sea state bin:

$$P(no\,rogue \mid Ss_i) = P(no\,rogue)_{i,avg}^{K} \qquad (5.7)$$

Notice that in figure 5.19 the number in each bin represents a sea state of 1 hour. So to calculate K this number is multiplied by three.

At some point sea states will be excluded from the calculation based on the wave breaking limit $H/L < 0.14$ [40]. To give a quick indication of this cut-off limit the lowest crest-to-trough threshold of table 5.3, H_{rogue} = 17.56 m, is taken as an example. The minimum wavelength which a wave should have in order to attain such a wave height and not break would be $\sim 125\ m$. Using the dispersion relationship, this corresponds to a minimum wave period of 9 s. For each bin this wave breaking limit is evaluated using the average mean zero-crossing period. Since the wave breaking limit is defined with respect to the wave height and not the crest height, the rogue wave height from table 5.3 is used to determine the wave breaking limit belonging to the rogue crest height in the same row as well.

By keeping in mind the wave period cut-off limit for wave breaking, an assumption can be made from which point the inclusion of low sea states in the overall rogue wave probability calculation becomes insignificant. Since the lowest rogue wave threshold requires a minimum wave period of 9 s, we can disregard all bins containing waves with a lower mean zero-crossing period. The largest amount of sea states found in one bin in the valid T_m range then becomes '2758' (bin $2 < H_s \leq 2.5$ & $9 < T_m \leq 10$). Following equation 5.7, this would lead to $K_{max} = 8274$. Once the largest average sea state exceedance probabilities $P(no\,rogue)_{i,avg}$ are found to be in the order 10^{-9}, the inclusion of lower sea states are disregarded. Even using the value K_{max}, this

would no longer significantly influence the overall rogue probability.

5.7.1. Results - Overall probability within data set

In tables 5.4 and 5.5 below the probabilities of at least one wave within the data set exceeding one of the rogue thresholds are presented. As considered area $6.5 \times 6.5 \text{m}^2$ has been chosen in accordance with the waterline diameter of the OC3 Hywind spar.

Notice that in some cases the probabilities in column 3 (second rogue threshold) are lower than those in column 4 (first rogue threshold). This may seem counterintuitive but can be explained by the fact that sea states in which a certain treshold is not considered rogue are excluded from the overall probability calculation. Raising the threshold means the inclusion of higher sea states, and in this case the inclusion of these higher sea states adds more to the probability than what is lost by raising the threshold.

An example, the third rogue crest threshold ($\eta_{rogue} = 11.41m$) was formulated using the average H_s of the sea states in the range $9 < H_s \leq 9.5m$. The higher sea states, such as $9.5 < H_s \leq 10m$ and $10 < H_s \leq 10.5m$, are excluded in this calculation because there the crest would not be considered rogue.

Probability <u>at least one</u> rogue crest Data set, 19.5 years	$\eta_{rogue} = 10.98m$ [%]	$\eta_{rogue} = 11.41m$ [%]	$\eta_{rogue} = 12.4m$ [%]	$\eta_{rogue} = 12.98m$ [%]
Forristall	7.5	5.7	1.2	1.7
Tayfun	13.6	10.5	2.4	2.7
Tayfun-Fedele	28.5	22.1	5.9	5.6
STE2 $6.5 \times 6.5\text{m}^2$	65.5	55.8	22.4	20.2

Table 5.4: Probabilities of at least one rogue crest exceeding one the rogue thresholds within the data set, according to the Forristall, Tayfun, Tayfun-Fedele and the STE2 model.

Probability <u>at least one</u> rogue wave Data set, 19.5 years	$H_{rogue} = 17.56m$ [%]	$H_{rogue} = 18.26m$ [%]	$H_{rogue} = 19.84m$ [%]	$H_{rogue} = 20.62m$ [%]
Naess	37.9	27.8	6.6	8.5
Rayleigh	93.4	83.3	32.7	35.5
STE1QD $6.5 \times 6.5\text{m}^2$	93.2	84.7	43.1	40.4

Table 5.5: Probabilities of at least one rogue wave exceeding one the rogue thresholds within the data set, according to the Naess, Rayleigh and STE1QD model.

5.7.2. Results - 50-year probability extrapolation

A common extreme wave return period for offshore design calculations is 50 years. To estimate the probability of at least one of the rogue waves occurring within 50 years, the results from the data set have to be extrapolated. Hereby the assumption is made that the distribution of sea states retrieved from the data set is representative for the wave climate. Extrapolation from 19.5 to 50 years is done by multiplying exponent K (Eq. 5.7) by a factor $Y = 50/19.5 = 2.56$ and subsequently rounding K down to a whole number. The extrapolated 50-year return probabilities are presented in table 5.6 and 5.7 below.

Probability <u>at least one</u> rogue crest 50-year extrapolation	$\eta_{rogue} = 10.98m$ [%]	$\eta_{rogue} = 11.41m$ [%]	$\eta_{rogue} = 12.40m$ [%]	$\eta_{rogue} = 12.98m$ [%]
Forristall	18.2	14.0	3.0	4.4
Tayfun	31.3	24.6	6.1	6.8
Tayfun-Fedele	57.8	47.2	14.6	13.8
STE2 $6.5 \times 6.5\text{m}^2$	93.5	87.6	48.0	43.9

Table 5.6: Probabilities of at least one rogue crest exceeding one the rogue thresholds extrapolated from 19.5 to 50 years, according to the Forristall, Tayfun, Tayfun-Fedele and the STE2 model.

Probability __at least one__ rogue wave	$H_{rogue} = 17.56m$	$H_{rogue} = 18.26m$	$H_{rogue} = 19.84m$	$H_{rogue} = 20.62m$
50-year extrapolation	[%]	[%]	[%]	[%]
Naess	70.6	56.6	16.3	20.4
Rayleigh	99.9	99.0	64.1	67.5
STE1QD 6.5×6.5m^2	99.9	99.2	76.6	73.5

Table 5.7: Probabilities of at least one rogue wave exceeding one the rogue thresholds extrapolated from 19.5 to 50 years, according to the Naess, Rayleigh and STE1QD model.

5.7.3. Results - Estimated return periods

To compare the probability models in a way which is perhaps more relevant for design purposes, their estimated return periods will be evaluated. To do this, we again assume that the distribution of the sea states from the data set is representative for the full wave climate at this location. Also, an assumption has to be made about with which rogue wave probability one may say that the wave will occur. This probability will differ regarding ones desired risk profile, but for the purpose of this thesis a probability of 95% will be considered sufficient. These return periods are found by the same extrapolation method as applied for the 50-year return period in the previous subsection.

The 95% probability is an arbitrary threshold chosen as a value to represent the situation that 'most probably' at least one rogue wave has occurred. This value could also have been slightly higher or lower, depending the desired risk profile. Its good to note that these exact return periods are not the primary interest, but they are used rather to compare the models in terms of a common parameter used in design processes. Again clearly visible here is the behaviour that for some models, when the threshold is raised from the one in the third column to that of the fourth, the rogue wave actually becomes more likely due to the inclusion of higher sea states in which it is now considered rogue.

Probability __at least one__ rogue wave	$\eta_{rogue} = 10.98m$	$\eta_{rogue} = 11.41m$	$\eta_{rogue} = 12.40m$	$\eta_{rogue} = 12.98m$
Return period until 95% probability	[years]	[years]	[years]	[years]
Forristall	750	1000	5000	3350
Tayfun	400	525	2400	2150
Tayfun-Fedele	175	235	960	1010
STE2 6.5×6.5m^2	55	72	230	260

Table 5.8: Return periods in years necessary for a 95% probability of at least one rogue crest occurring, per threshold, for the Forristall, Tayfun, Tayfun-Fedele and STE2 model.

Probability __at least one__ rogue wave	$H_{rogue} = 17.56m$	$H_{rogue} = 18.26m$	$H_{rogue} = 19.84m$	$H_{rogue} = 20.62m$
Return period until 95% probability	Years	Years	Years	Years
Naess	123	180	850	660
Rayleigh	22	33	147	134
STE1QD 6.5×6.5m^2	22	31	104	113

Table 5.9: Return periods in years necessary for a 95% probability of at least one rogue wave occurring, per threshold, for the Naess, Rayleigh and STE1QD model.

5.8. Conclusions - Rogue wave probability

In this chapter, research into the probability of a rogue wave occurring offshore California was presented. The following subjects have been treated:

- Different probability models have been compared, whereby the influence of the spatial scale of the STE models was investigated.

- The influence of the shape of the wave spectrum on the estimated rogue wave probability was explored by evaluating two spectral parameters.

- Overall rogue wave probabilities were calculated for four rogue wave crest and crest-to-trough sizes.

When comparing the wave crest probability models on maximum exceedance probability per sea state, it was observed that even as the area sides X and Y approached $0m$, the STE2 model estimated a higher probability of a rogue crest occurring than the Forristall and Tayfun model in all sea states. The Tayfun-Fedele model estimated a slightly higher rogue crest probability than the STE2 model in two sea states, though only when the area size was smaller than $2\times2m^2$. Because the Tayfun-Fedele model is the most conservative TE crest model, and an area size of $2\times2m^2$ is small when floating offshore wind turbines are considered, the inclusion of the spatial dimension using the STE2 model for rogue wave crests will provide the most conservative estimate in all sea states.

Regarding the crest-to-trough probability models, the results from the comparison of the Naess and STE1QD model indicate that the STE1QD model predominates the Naess model regardless of the area size in all sea states. In the comparison with the Rayleigh and the STE1QD model, it was observed that the Rayleigh model estimates a higher rogue wave probability in all sea states when the area is smaller than $2\times2m^2$. As the area size increases, the rogue probability estimated by the STE1QD model increases and from an area size of $12\times12m^2$ and larger it was observed that the STE1QD predominates the Rayleigh model. The Rayleigh model is generally considered to be conservative. These results indicate that if a structure with a footprint larger than $12\times12m^2$ is considered, the STE1QD model would be the most conservative in all sea states. Hereby it should be noted that the exact area size may differ based on the environmental parameters of a location. Nevertheless, seeing as the original STE1 model is constructed using the Rayleigh distribution, and the Rayleigh distribution is only dependent on the ratio of desired wave height to significant wave height, this area size is a good indication.

The influence of two spectral shape parameters on the estimated rogue wave probability was investigated. For the wave crest models it was observed that the rogue crest probability increases as the wave spectrum became more narrow. This was seen for all four wave crest models. Exceptionally large wave crests, such as these rogues, influence the height of the platform of offshore structures. These results would indicate that rogue crests may occur more frequently at locations with in general more narrow wave spectra, which in combination with the platform's footprint should be taken into account when designing the platform height above the MSL.

The Naess and Rayleigh crest-to-trough probability models showed no clear preference for a narrow or wide spectrum. The STE1QD model displayed a slight tendency of increased rogue wave probability for a narrower wave spectrum, though the slope of the trendline was minimal from which nothing can be concluded.

Four rogue crest and crest-to-trough sizes were chosen by calculating the average significant wave height of the four upper rows of the wave climate scatter diagram, and using those wave heights to evaluate the rogue thresholds. The probability of at least one of those rogue waves occurring within a certain time-span was calculated for each probability model. For the STE models an area size of $6.5\times6.5m^2$ was chosen after the OC3-Hywind spar waterline diameter. Three scenarios were investigated:

- The probability of at least one rogue event occurring within the usable data set, consisting of 19.5 years worth of wave data.

- The probability of at least one rogue event occurring with a 50-year return period.

- The return period per model until a 95% occurence probability of at least one rogue event is achieved.

For the long-term rogue crest probability it was observed that the Forristall model estimates the lowest occurrence probability, followed by the Tayfun model, then by the Tayfun-Fedele model, and the STE2 model estimates the highest occurrence probability. The difference between the Tayfun-Fedele model and the STE2 model was significant, which was expected regarding the earlier results from section 5.5.

The estimated return periods until a 95% probability of at least one rogue crest were given in section 5.7.3. In offshore design practices it is common to work with 50- and 100-year return periods for extreme environmental conditions [24]. The return periods estimated by the TE models all largely exceed the 100 years. Only the STE2 model estimates return periods lower than 100 years for the two smallest rogue crests. This illustrates how using an STE model could provide more conservative estimates than a TE model.

Between the crest-to-trough models it was observed that the Rayleigh and STE1QD model estimate higher overall occurrence probabilities than the Naess model. Earlier, during the model comparisons of maximum exceedance probabilities, we observed that up until an area size of $12 \times 12 \text{m}^2$ the Rayleigh model estimated higher rogue wave probabilities in several sea states. In this overall rogue probability calculation, where the probabilities are averaged per bin, the results indicate that for the considered area size of $6.5 \times 6.5 \text{m}^2$ the Rayleigh and STE1QD model estimate similar occurrence probabilities. For the two smallest rogue waves they are nearly identical, and for the two largest the STE1QD model is slightly more conservative. When the overall rogue wave probability is considered, it appears that the STE1QD model is already more conservative from an area size of $6.5 \times 6.5 \text{m}^2$.

6

Dynamic response SFWT to rogue wave

This chapter presents the research into the dynamic response of the OC3-Hywind model to a rogue wave. First, an overview of the OrcaFlex OC3-Hywind model is given. Then, a theory to embed deterministic extreme waves in a random wave series, called the most likely wave model (MLW), is presented. Subsequently, using the rogue wave heights with different occurrence probabilities as evaluated in the previous chapter, a deterministic rogue wave is embedded in a random wave series based on real wave spectra from the environmental data, using the MLW model. These wave time-series are then imported into OrcaFlex to simulate the rogue wave impact with the SFWT. The dynamic response is presented in terms of surge, heave, pitch and nacelle accelerations of the SFWT. In the end, these values are compared to some reference limits that exist in the literature to asses the severity of the motions.

6.1. Description OC3-Hywind OrcaFlex model

Orcina has constructed an OrcaFlex OC3-Hywind model, 'K01 Floating wind turbine', which is publicly available on their website [65]. This model consists of the 5MW NREL reference turbine (table 6.1a) placed on the OC3 Hywind spar substructure (table 6.1b). The 5MW NREL reference turbine is recognised as an industry-standard reference model which is representative for a utility-scale, multi-megawatt wind turbine. To keep the turbine from drifting, the spar is anchored to the sea bed by three catenary mooring lines. The spar has a draft of $120m$ and the top, upon which the turbine tower is placed, extends $10m$ above the SWL.

5MW wind turbine		OC3-Hywind spar substructure	
Parameter	**Value**	**Parameter**	**Value**
Rotor, hub diameter	126 m, 3 m	Total draft	120 m
Hub height	90 m	Elevation to platform top above SWL	10 m
Cut-in, Rated, Cut-Out wind speed	3 m/s, 14 m/s, 25 m/s	Depth to top of taper below SWL	4 m
Rotor mass	110 000 kg	Depth to bottom of taper below SWL	12 m
Nacelle mass	240 000 kg	Platform diameter above taper	6.5 m
Tower mass	347 460 kg	Platform diameter below taper	9.4 m
Coordinate CM	(0.2m, 0.0m, 64.0m)	Total platform mass	7 466 330
		Number mooring lines	3
		Depth to fairleads below SWL	70 m
		Depth to anchors below SWL	320 m

Table 6.1: Some parameters of the OC3-Hywind model. (a) Properties of the 5MW reference turbine. (b) Properties of the OC3-Hywind spar substructure.

6.1.1. System modelling

The OrcaFlex OC3-Hywind model is built up out of the following components: the turbine, the tower, the spar platform and the mooring system. This subsection gives a brief overview of the modelling approach of the relevant parts.

The turbine element is a conventional three-bladed rotor, with options for variable speed and pitch control. A gear ratio can be specified and is set to 97 for the OC3-Hywind model. The rotor hub has a radius of $1.5m$ and is assigned to the turbine object. The transverse and axial moments of inertia around the main shaft are specified and the centre of mass of the hub is located at the geometric centre of the rotor.

The turbine blades in OrcaFlex are modelled by a structural model somewhat similar to the one used by lines, with inertia lumped at the nodes which are connected by massless segments. Each blade consists of 17 different elements, which can vary in length, wing type and (initial) pitch angle. The blade DOF's are set to 'free', which means that for each node, 6 DOF's are included. This allows the blade parts to move in a rotational and translational direction with respect to eachother, thus allowing the blade flexibility to be modelled.

The Nacelle is modelled as a 6D buoy object, with the proper mass, CM and inertia properties, as well as the appropriate C_M and C_a coefficients to capture the aerodynamic effects. Figure 6.1 below illustrates how the whole turbine element is modelled.
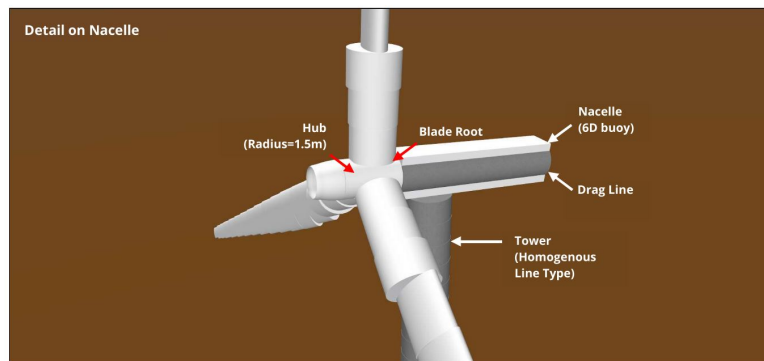
Figure 6.1: A detail of the nacelle to illustrate the turbine modelling. Retrieved from [69].

The conical tower is modelled as a line object with a 'homogeneos pipe' line type assigned to it. By doing so, a variable wall thickness can be modelled with the appropriate inner and outer diameters, as well as the physical properties of the tower such as the material density, young's modulus and Poisson ratio. This leads to a model where OrcaFlex can take the structural deflection of the tower into account.

The spar platform is modelled in Orcaflex using the 'spar' category of the 6D buoy element. This results in a rigid body spar platform, with 6 DOF's and the appropriate geometric and physical properties assigned to it. The spar buoy is split up into 40 discrete cylinders. To accurately capture changes to the hydrodynamic loading and buoyancy on the surface-piercing part of the spar buoy, the cylindric parts in the top section have been assigned a fine discretisation of $1m$, while for the lower part a discretisation of $10m$ is considered (see figure 6.2). To calculate the hydrodynamic loads on the spar in Orcaflex, the extended Morison's equation is considered (Eq. 6.7). The influence of radiation damping and diffraction effects are assumed negligible, as is assumed by the OC3 NREL report [46].
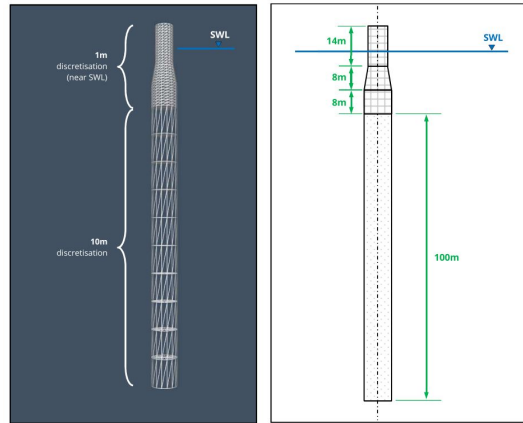
Figure 6.2: The OC3 Hywind spar substructure as built in OrcaFlex. Retrieved from [69].

The three catenary mooring lines holding the spar in place are assigned their physical properties via the appropriate line type elements. The anchors and mooring lines are placed evenly around the spar in azimuth increments of 120°, and the radius of the anchors to the centerline of the spar is approximately $854m$. The mooring lines are connected to the spar via a 'delta' or 'crowfoot' connection, as illustrated in figure 6.3. Each line is connected to the spar at a radius of $5.2m$ measured from the spar's centerline.
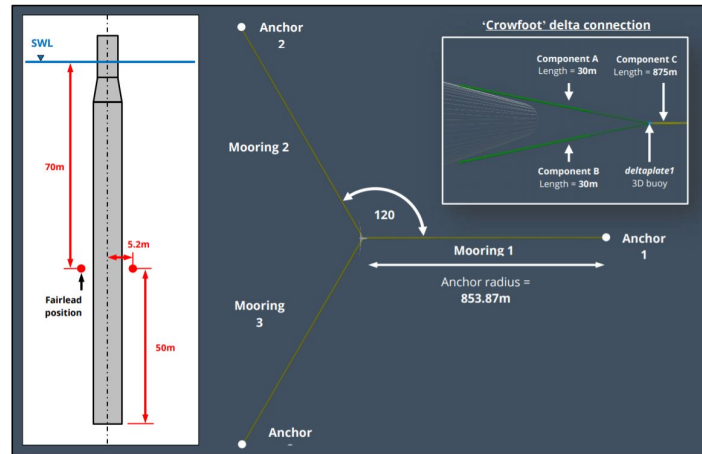
Figure 6.3: The mooring line arrangement of the OrcaFlex OC3-Hywind model. Retrieved from [65].

6.2. Most likely wave model

Computer simulations of a structure in a random wave field aimed at obtaining extreme loads can be incredibly time-consuming. A preferred alternative is a deterministic load condition which is accurate to a high enough degree. This section gives an overview of a popular theory, the most likely wave model, used to generate deterministic extreme waves and embed them in a random wave series.

Tromans *et al.* (1991) presented a theory for a deterministic probabilistic formulation of a single extreme wave called the NewWave theory [85]. Comparisons between this wave theory, time domain simulations and Stokes fifth order waves proved to be in excellent agreement. This section will give a brief overview of the NewWave theory.

The free surface elevation $\eta(x, y, t)$ may be assumed stationary over a finite area for a certain time duration, typically three hours. Then, η can be presented as a summation of harmonic components:

$$\eta(x, y, t) = \sum_n c_n \cos\left(k_n x \cos\theta_n + k_n y \cos\theta_n - \omega_n t + \epsilon_n\right) \tag{6.1}$$

where n is a large number and c_n is given by:

$$< c_n^2 >= 2 f(\omega_n, \theta_n) S(\omega_n) \Delta\omega\Delta\theta \tag{6.2}$$

For a component n, the wave number is k_n, the direction relative to the mean wave direction is θ_n, the frequency is ω_n and the phase is ε_n. The directional wave spectrum is given by $f(\omega_n, \theta_n) S(\omega_n)$. Extreme waves are waves that form when many components come into phase. In the NewWave theory a formulation is presented such that the largest waves of the sea can be described with deterministic phases and amplitudes. The surface elevation can be written as a function of time such that it is normally distributed around a most probable (and expected) value η_d^*:

$$\eta^* = \alpha\rho(\tau) + g(\tau) \tag{6.3}$$

where $\tau = t - t_1$, α is the crest amplitude and $\rho(\tau)$ is the autocorrelation function of the surface elevation. The first term of equation 6.3 is the most probable value η_d^*:

$$\eta_d^* = \alpha\rho(\tau) \tag{6.4}$$

This most probable value is deterministic and proportional to the crest amplitude. The second term of Equation 6.3 is a non-stationary Gaussian function with a zero mean and a standard deviation that increases from zero at the crest to the regular standard deviation of the underlying wave once it moves away from the crest. Equation 6.4 can be generalised such that:

$$\eta_d^*(X, t) = \frac{\alpha}{\sigma^2} \sum_n d_n \cos(k_n X - \omega_n t) \tag{6.5}$$

where $d_n = S(\omega_n) \Delta\omega$ and $X = x - x_1$.

Taylor *et al.* showed in their 1997 paper how the NewWave profile embedded in a stochastic wave time-series can be used to estimate the extreme response of a Jack-Up [82]. Their method ensures a deterministic extreme wave at t_0, after which the wave series returns to the random shape of the background waves. Their approach can be explained as follows: they state that a random wave series has an elevation a_0 and slope $\dot{a}$ at t_0. This elevation and slope are multiplied by the autocorrelation function $\rho(\tau)$ and its derivative $\dot{\rho}(\tau)$ respectively and subtracted from the signal. Due to the specific shape of the autocorrelation function this process essentially 'removes' the random wave which originally was at t_0. Then they add the desired deterministic wave back to the wave series with $a \cdot \rho(\tau)$. The exact process is given by equation 6.6 below. By adding equation 6.6 to equation 6.1 the NewWave model is embedded in the random wave series. This combination of NewWave theory and equation 6.6 is also referred to as the most likely wave (MLW) model.

$$\Delta a = (-a_0 + a) \cdot \rho(\tau) - \frac{\dot{a}}{\lambda^2} \cdot \dot{\rho}(\tau) \tag{6.6}$$

Here λ^2 is obtained using the second spectral moment: $m_2 = \lambda^2\sigma^2$.

6.3. Deterministic rogue wave time-series

To embed a deterministic rogue wave in a random wave series, both the NewWave theory and equation 6.6 (together the MLW model) are used. For each of the four rogue wave thresholds defined in table 5.3, five wave time-series have been generated with a deterministic rogue wave at t_r. These wave time-series consist of two parts: a random generated wave series from a wave spectrum and a deterministic rogue wave with a crest-to-trough height corresponding to the four rogue wave sizes. These two parts are explained further in detail in the subsections below.

6.3.1. Part 1: the wave spectrum

The wave spectrum which is used to generate the random wave series is different for the four rogue wave sizes. As explained in section 5.7, the four rogue wave thresholds were established by taking the four upper most rows of figure 5.19, calculating the average significant wave height per row, and using that average value to evaluate equation 2.1 and 2.2.

For each size rogue wave a 'most likely wave spectrum' is estimated. This most likely wave spectrum aims to reflect the average of the sea states in which that particular size rogue wave is most likely to occur. This

is useful because in theory such a rogue wave could form in many of the sea states, but averaging them all would not reflect the most probable conditions. The lower sea states are much less likely to produce a large rogue wave, despite them being more numerous. An assumption is made that the most likely wave spectrum consists of the averaged wave spectra belonging to the scatter diagram row of that particular rogue wave threshold, together with two rows below. An example: the third largest rogue wave, $H_{rogue} \geq 18.26$, was defined by taking the average H_s of row $9 < H_s < 9.5m$ to evaluate the rogue wave definitions. To calculate the most likely wave spectrum, all wave spectra belonging to that row, and two rows below ($8 < H_s < 8.5m$ and $8. < H_s < 9m$) are averaged. See for example figure 6.4, which shows the considered wave spectra (grey lines) used to calculate the most likely wave spectrum (red line) for the third rogue wave threshold.
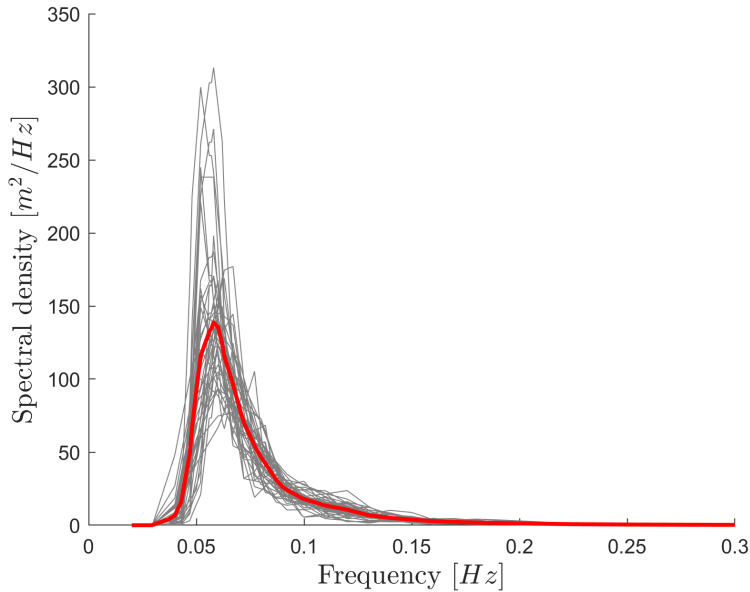
Figure 6.4: A visual representation of the most likely wave spectrum for the third rogue wave threshold $H_{rogue} \geq 18.26$. Grey lines represent the considered wave spectra and the red line represents the average, or the most likely wave spectrum. Only wave spectra belonging in the scatter diagram row of the particular rogue wave threshold and two rows below are considered.

The random wave time-series were generated from these most likely wave spectra, using the Python random module for the phase of each wave component, with a unique seed for each series. To determine whether a specific simluation duration is needed before the spar model reaches its equilibrium position, a few OrcaFlex simulations are done using the generated random wave series. Based on the surge response of the spar in these wave series no specific ramp-up period seems to be necessary in the main simulation, as the surge response immediately shows steady state behaviour.

Before the main simulation in Orcaflex there is usually a build-up stage, during which the motions of the vessel and the waves are smoothly built up from zero to their full magnitude. This build up period is chosen to be $50s$. When importing a wave time history in Orcaflex, one of the requirements is that it should have a number of components equal to a power of two (eg. 1024, 2048, 4096). Based on this requirement, the $50s$ build up period and the fact that no specific duration is needed before the system reaches its equilibrium, a total simulation time of $512s$ is chosen, where -$50s$ to $0s$ is the build up stage, and $0s$ to $462s$ is the main simulation. The time for the deterministic rogue wave to occur within the simulations is chosen to be at $350s$.

6.3.2. Part 2: the deterministic rogue wave
The deterministic rogue wave is modeled using the NewWave theory. The autocorrelation function of the underlying wave spectrum, used to estimate the deterministic shape of the large waves in that sea state, is obtained by averaging the autocorrelation functions of the wave spectra previously used to determine the most likely spectrum. This average autocorrelation function should therefore represent, in the same sense as the spectrum, a 'most likely' rogue wave shape. Figure 6.5 illustrates this process, where the considered

spectra are the same as those in figure 6.4, for the third rogue wave threshold. Notice that the peak of the function is already positioned at the desired timestamp of the deterministic rogue wave, at $t_r = 350s$.
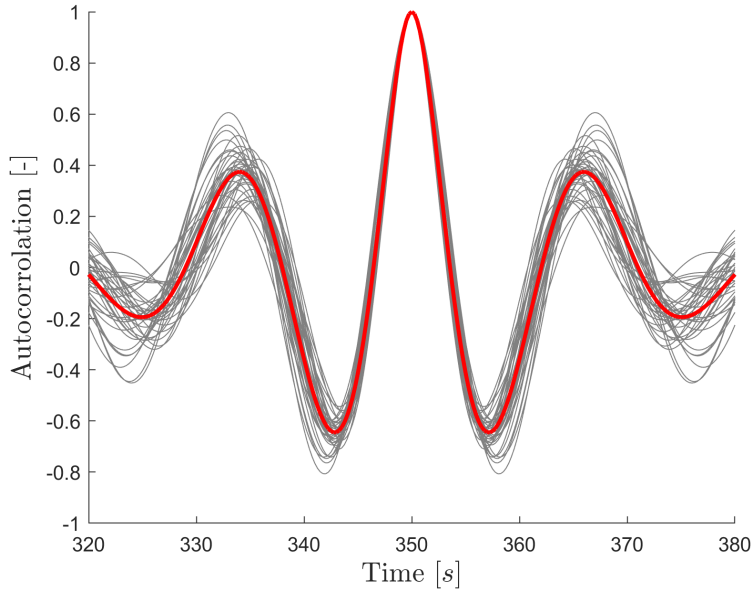
Figure 6.5: A visual representation of the most likely rogue wave shape for the third rogue wave threshold $H_{rogue} \geq 18.26$. Grey lines represent autocorrolation functions of the considered wave spectra where the red line represents the average.

The most likely rogue wave shape greatly influences the period of the final rogue wave embedded in the wave time-series. The wave periods associated with the most likely wave shapes for the four rogue wave sizes are presented in table 6.2 below.

H_{rogue} [m]	Period most likely shape [s]
20.62	16.0
19.84	15.8
18.26	15.6
17.56	15.4

Table 6.2: Wave periods of the corresponding most likely rogue wave shapes.

Now, using equation 6.6, the deterministic rogue wave can be embedded in a random wave series based on the relevant most likely wave spectrum. Figure 6.6 shows an excerpt of a random wave series, from $250s$ to $450s$, with the embedded deterministic rogue wave at $350s$. The deterministic wave series (black solid line) converges again with the unmodified random wave series (red dashed line) after about 40 seconds.
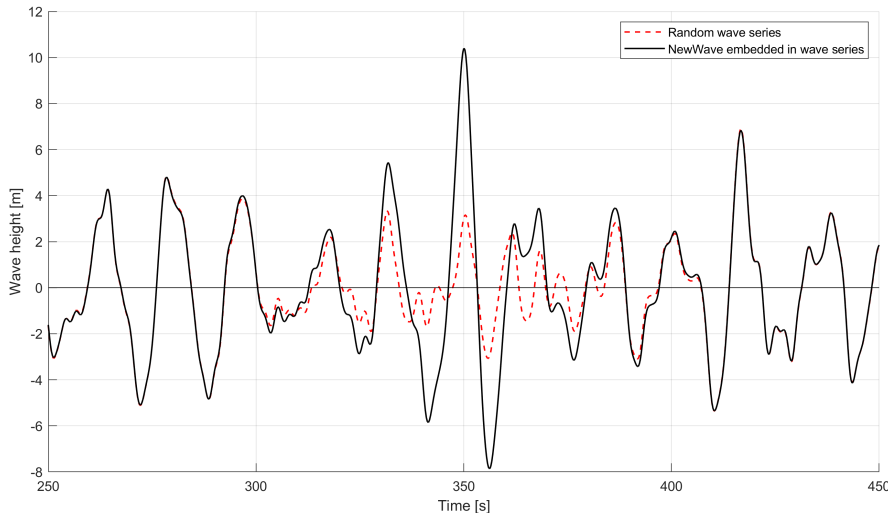
Figure 6.6: An excerpt from a wave time-series with a deterministic rogue wave embedded at 350s (black solid line). The red dashed line shows the unmodified random wave series. The rogue wave crest-to-trough height is 18.26m, after the third rogue wave threshold.

The MLW model gives a stochastic wave series where the size of the deterministic wave can be easily controlled. The peak of the wave is the point where the model is completely deterministic. Here the autocorrolation function equals '1' and the underlying wave of the random wave spectrum is essentially removed. However, once we start progressing away from this peak, the shape of the wave starts to get influenced by both the autocorrolation function and the underlying wave spectrum. Due to this influence of the underlying wave spectrum we will not see the exact shape of the autocorrolation embedded in the random wave series, but it will be very similar. This also influences the wave period, which will not be the exact value from table 6.2. At the moment this is a known shortcomming of the MLW model and unfortunately no improved alternative has been found yet.

6.4. From wave time history to dynamic response in OrcaFlex

A wave time history which is imported in OrcaFlex gives the wave elevation at a single point, the wave origin. However, OrcaFlex needs to obtain the wave elevation at any point on the sea surface for a successful simulation. OrcaFlex achieves this by performing a Fast Fourier Transform (FFT) on the wave elevation data, transforming the data into a number of frequency components. The FFT requires the number of samples N in the time history to be a power of 2 and returns $N/2$ components. A single Airy wave is used to represent such a component, and the combination of all these Airy waves is then used to determine the wave elevation and its kinematics at all points. This estimation which uses Airy wave components linearizes the waves. The velocity field of a nonlinear wave can be larger in magnitude, however if the waves are assumed to be non breaking, velocities approximated using linear wave theory will not deviate much [4].

In the previous section the choice was made to generate time histories with 2048 components. With $N = 2048$ our time history will be approximated by a superposition of 1024 Airy wave components. OrcaFlex essentially extrapolates these Airy wave components from the wave origin to all other points in order to derive the kinematics and elevation there. Such extrapolation induces errors which increase further away from the wave origin. To reduce these errors it is advised to choose the wave origin such that it is placed as close as possible to the most wave-sensitive parts of the model. During the simulations the wave origin is defined to be at $x = 0$, $y = 0$, which corresponds to the initial position of the centerline of the spar.

6.4.1. Dynamic response

During a time domain simulation in OrcaFlex the vessel motions are calculated by solving a 6-DOF equation of motion, as previously given by equation 3.1. Hydrodynamic loads are calculated by an extended form of the Morison's equation, which was given in its original form by equation 3.3. The extended form applies the

same principles, but for a moving body. For a moving body the inertia term is reduced by $C_a\Delta a_b$ and the drag term uses the velocity relative to the body. This results in the following extended Morison's equation used by OrcaFlex:

$$\boldsymbol{f} = (C_{\mathrm{M}}\Delta\boldsymbol{a}_{\mathrm{f}} - C_{\mathrm{a}}\Delta\boldsymbol{a}_{\mathrm{b}}) + \frac{1}{2}\rho C_{\mathrm{D}} A |\boldsymbol{v}_{\mathrm{r}}| \, \boldsymbol{v}_{\mathrm{r}} \tag{6.7}$$

where f is the wave force per unit length, C_M, C_a and C_D are the inertia, added mass and drag coefficient respectively, Δ is the water mass displaced by the body, a_f and a_b are the water acceleration and the vessel acceleration both relative to earth, ρ is the density of the water, A is the drag surface area and v_r is the water velocity relative to earth. The superposition of Airy waves which is created from the time history input can then be used by OrcaFlex to calculate the water particle velocity and acceleration components to serve as input in equation 6.7.

OrcaFlex offers two options for the solution method of the time simulation: an implicit and explicit integration scheme. The implicit integration scheme was introduced after the explicit scheme and provides huge improvements in run time. This is the default integration scheme and will be used for this thesis. For the implicit integration, OrcaFlex uses the generalised $-\alpha$ integration method as described by Chung and Hubert [23]. At the start of the simulation, the system takes into account the initial positions and orientations of all objects and nodes, which follow from the static analysis. The forces and moments acting on each node and free body are calculated. These forces and moments include: weight, buoyancy, hydro- and aerodynamic forces, shear and tension, bending and torque, friction with the seabed and forces due to contact with other objects. Then at the end of the time step the system equation of motion is solved. The dynamic equilibriums are found using an iterative method. If after a certain number of iterations no convergence has been achieved, the simulation is aborted.

6.5. OrcaFlex simulations

For each size rogue wave, five random seeds have been used to generate five random wave-time series. Per random seed, one wave time-series with, and one wave series without a rogue wave is made. This wave series without a rogue wave embedded can be seen as a base case, allowing a comparison to be made between the dynamic response induced by the rogue wave and the dynamic response which would have been observed in just the heavy sea state.
During the simulations, only the wave loads are considered. The wind and current speeds are set to $0\ m/s$, and the turbine is assumed to be in a parked condition, specified by setting the variable speed of the rotor to $0\ m/s$. These environmental conditions do however influence the dynamic response, which is why research in this area will be recommended for future work.

The dynamic response of the SFWT will be investigated on the basis of the surge, heave, pitch and nacelle acceleration. The wave time-series are imported as .txt files containing surface elevation and time in two columns. The default time-step for time domain simulations in OrcaFlex is $0.1s$, and there is no time-step size requirement when using the implict solution scheme. A time step sensitivity check is done by running one case using three different time steps: $0.1s$, $0.05s$ and $0.01s$. The goal is to asses which time step should be used in the further simulations, where a tradeoff between computation time and accuracy is made. A $0.05s$ time step is deemed best for this research, since a smaller time step only shows marginal differences in the results. See Appendix C for the evaluation.

6.5.1. Results - Dynamic response

Table 6.3 below presents the dynamic response of the SFWT in the base case wave series, and table 6.4 presents the results for the wave series with a rogue wave embedded. The reason a rogue wave size is reported in table 6.3, despite it being a random wave series without such a wave, is to make clear to which rogue wave threshold the wave series belong. For each parameter, the average maximum of the five simulations is reported. Also, the average period of the rogue wave is reported, due to this being slightly different in each wave series as explained in section 6.3.2. The individual simulation results for both the simulations with, and without a rogue wave, together with for each size rogue wave an impression of the dynamic response during the full simulation, are given in appendix D.

Some observations regarding the results from table 6.3 and table 6.4:

- The differences in dynamic response between the base case simulations (table 6.3), and the simulations with a rogue wave (table 6.4) can be clearly seen. The values of the four reported parameters in simulations with a rogue wave, for all wave series, are significantly higher. For example, for the simulation with the largest rogue wave the surge increased with 99.9%, the heave with 87.6%, the pitch with 60.7% and the nacelle acceleration with 61.1%.

- The largest rogue wave led to the largest surge response of $16.91m$, followed by the third largest rogue wave inducing a surge response of $15.32m$.

- The heave response is mild overall. The largest rogue wave led to the largest response, which is only $3.02m$. This comes as no surprise, as spar designs are great at reducing heave motions [56]. Also, the maximum of the heave motion did not always directly correlate with the rogue wave, but could also be found some time later. See for example figure 6.7.

- The largest rogue wave led to the largest pitch angle of 7.15°, followed by the third largest rogue wave inducing a pitch angle of 6.97°.

- The top three rogue wave sizes produced almost identical averaged nacelle accelerations of about 3.81-3.83 m/s^2, and the response to the fourth rogue wave is very close to this value.

- In both the simulations with the third and fourth largest rogue wave there is one simulation which could be considered an outlier (see Appendix D), due to the significantly higher induced response. In the case of the third largest rogue, this simulation is the cause that the induced motions are higher compared to those of the second largest rogue wave. In the case of the fourth largest rogue wave, the 'outlier' causes the motions to be more similar to the simulations with a higher wave than one would perhaps expect.

It is not always the case that larger rogue wave simulations induce motions which are much more extreme than the lower ones. This can be explained as follows: the seeds used to generate the random underlying wave spectrum are different for each simulation. This leads to different initial conditions of the floating turbine system before the rogue wave impact. Due to this, some initial conditions might be more favorable to induce extreme motions than others, which can lead to lower rogue waves inducing similar or more extreme motions than the larger ones.

Rogue wave size Without embedded rogue wave	Rogue period [s]	Surge [m]	Heave [m]	Pitch [°]	Nacelle acceleration [m/s^2]
H_{rogue} = 20.62	-	8.46	1.61	4.45	2.43
H_{rogue} = 19.84	-	8.41	1.81	4.66	2.77
H_{rogue} = 18.26	-	6.45	1.42	3.90	2.44
H_{rogue} = 17.56	-	6.56	1.37	3.73	2.29

Table 6.3: Dynamic response results from the OrcaFlex simulations. The wave series used for these simulations consisted of only the random wave series without a rogue wave embedded. Reported values are the average of the maximums of five simulations. Surge, heave and pitch are evaluated for the spar at the height of the MSL. Only the hydrodynamic loads are considered.

Rogue wave size With embedded rogue wave	Rogue period [s]	Surge [m]	Heave [m]	Pitch [°]	Nacelle acceleration [m/s^2]
H_{rogue} = 20.62	15.67	16.91	3.02	7.15	3.81
H_{rogue} = 19.84	15.57	14.31	2.51	6.35	3.83
H_{rogue} = 18.26	15.3	15.32	2.53	6.97	3.82
H_{rogue} = 17.56	14.3	13.07	2.01	5.63	3.69

Table 6.4: Dynamic response results from the OrcaFlex simulations. The wave series used for these simulations had the rogue waves embedded. Reported values are the average of the maximums of five simulations. Surge, heave and pitch are evaluated for the spar at the height of the MSL. Only the hydrodynamic loads are considered.

The dynamic response observed in the rogue wave simulations can be compared with the results of the two papers described in section 3.2.1, to see whether they are in the same ballpark. Both these authors used the

same OC3-Hywind spar design used in this study. Ruzzo *et al.* used an in-house 3-DOF numerical code and reported a maximum surge of $5.62\,m$, maximum heave of $4.38\,m$ and a maximum pitch angle of 7.77°, in response to a $20\,m$ rogue wave [70]. Qu *et al.* used an in-house 6-DOF numerical code and reported a maximum surge of about $16\,m$, maximum heave of about $1.75\,m$ and a maximum pitch of about 11.7°, in response to a $18.28\,m$ rogue wave with a $26\,m/s$ wind speed [66]. These results, though obviously not the same, suggest that the results from the OrcaFlex simulations seem very reasonable.

To illustrate the dynamic response, figure 6.7 presents an excerpt of the surface elevation and the response in surge, heave and pitch, of one simulation. This simulation was done with a rogue wave size of $20.62\,m$, which is visible at $350\,s$. The heave response is in phase with the large waves, and the maximum heave response is seen some time after the rogue wave. The surge and pitch response attain their maximum shortly after the rogue wave has passed.
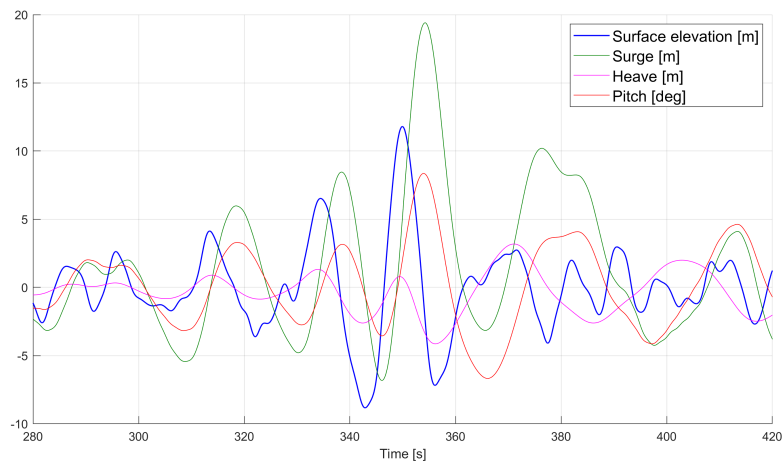
Figure 6.7: An excerpt from a simulation with a rogue wave $H_{rogue} = 20.62\,m$, showing the surface elevation, surge, heave and pitch response from $280\,s$ to $420\,s$.

Figure 6.8 presents an excerpt of the surface elevation and the nacelle acceleration. The nacelle acceleration is reported by Orcaflex only in absolute values, which is why the acceleration never moves below $y = 0$. The maximum nacelle acceleration is attained just after the rogue wave has passed. It appears that the nacelle acceleration varies with a second frequency besides the wave excitation, which may be due to the flexible modeling of the tower (see section 6.1.1).
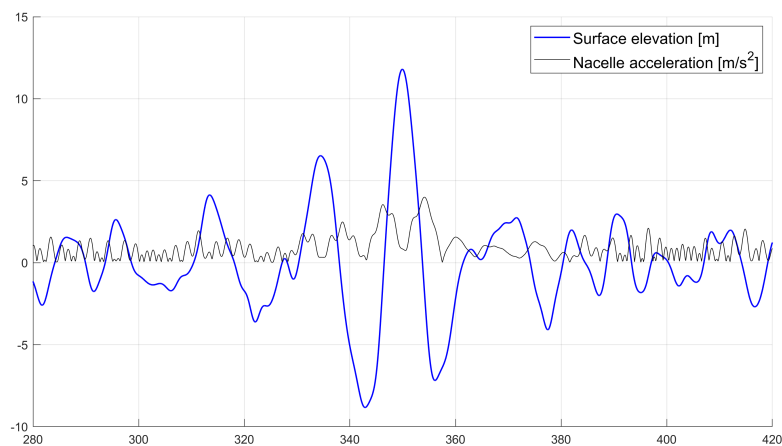
Figure 6.8: An excerpt from a simulation with a rogue wave $H_{rogue} = 20.62\,m$, showing the surface elevation and the nacelle acceleration from $280\,s$ to $420\,s$.

6.6. Conclusions - Dynamic response

In this chapter, research into the dynamic response of the OC3-Hywind SFWT against multiple rogue waves with different occurrence probabilities was presented. The rogue waves were each embedded in a random wave series, based on their most likely wave spectrum, using the MLW model. The time domain simulations have been done in OrcaFlex and both the responses to the wave series with and without a rogue wave have been reported. Earlier, the return period until a 95% occurrence probability for these rogue waves was calculated using different models. From these return periods it can be concluded that these rogue waves are a single, rare event during the life of an offshore structure, which good to consider when the dynamic responses are evaluated.

When comparing the dynamic response of the SFWT in the base case wave series (table 6.3) to the response of the wave series with a rogue wave embedded (table 6.4), it became evident that the deterministic rogue waves induced significantly more extreme motions compared to just the heavy sea state alone. The biggest surge, heave and pitch response followed from simulations with the largest rogue wave. The three largest rogue waves produced nearly identical nacelle accelerations, which can be explained by the turbine having more or less favorable initial conditions before the rogue wave impact.

It is difficult to make unambiguous conclusions regarding the potential danger of a rogue wave to the SFWT based only on the dynamic response. First of all, there are no specific limits for translational displacements of a catenary moored SFWT. Mostly the pitch angles and nacelle accelerations are limiting, due to stability criteria and the presence of sensitive components in the nacelle, such as the gearbox, generator and bearings. In the industry, these maximum angles and accelerations of wind turbines are imposed by the turbine OEM's (original equimpment manufacturers) and are treated very secretively. Even when a company is working on a project with an OEM, these limits tend not to be shared unless absolutely necessary (personal communication IntecSea). Regarding the OC3-Hywind system, no such limits were shared with NREL, and they were unsure if such information even had been developed (personal communication NREL).

In the literature, a few claims have been made regarding maximum allowable inclination and nacelle accelerations. Papers that discuss the pitch angle state that the maximum pitch angle should be taken as 10° [49] [72] [41] [78]. In absence of exact values from the industry, and in regard to the unanimity of the papers all deciding on a 10° maximum pitch angle, this could be used as a reference value for this thesis. Though it has to be said that the 10° seems to be regarded as a conventional value, mostly assumed in papers or desired as a maximum value during power production, and that little research seems to have been done into the true survivability aspect of this inclination angle. Whether the 10° relates to power production or survivability is something the literature doesn't agree on.

Regarding the nacelle acceleration, some papers state that $0.4g$ (3.92 m/s^2) is a common industry limit [78] [14] [15]. Other papers assume lower limits, such as $0.3g$ [62], or even $0.2g$ [51]. These provide some reference value for this thesis, although again the notion has to be made that little to no substantiation is given in these papers in terms of calculations regarding this number, and that the argumentation seems to be mostly based on 'common industry knowledge'.

When comparing the responses of table 6.4 with the reference values found in the literature, it appears that the pitch angles are below the conventional literature limit of 10°, and the nacelle accelerations are below $0.4g$. Regarding the pitch angle, its important to note that in the current simulations only the hydrodynamic loads have been considered. No wind or current speeds were simulated, while these also contribute to the dynamic response. It is expected that the addition of these environmental forces will increase the already significant pitch angles to values over this literature limit. Whether this will then be damaging to the turbine is difficult to say.

The nacelle accelerations can be said to be quite significant, as they are only slightly below the $0.4g$ literature limit, and notably higher than the lower 0.2 and $0.3g$ limits. It's not certain that the addition of more environmental factors will increase the maximum nacelle accelerations further, as the wind may also have a damping effect on the turbine motion.

When considering induced motions in single simulations (Appendix D), as opposed to the average of the five, sometimes the nacelle acceleration does exceed the $0.4g$. This does not immediately mean that the waves are dangerous. First of all, it's good to remember that the $0.4g$ is a reference value and that a single excursion over this limit may not immediately damage components. Also, different initial conditions of the turbine result in

more or less extreme motions. As this wave is a single, rare event in the life of a SFWT, the results are averaged over the five simulations to reduce the importance of these initial conditions, so the average portrays a more stable estimate.

To summarize, because the rogue wave is a single rare event and the values are below the $0.4g$ threshold, it appears that these nacelle accelerations are not especially threatening, but in the end this will depend on the sensitivity of the components inside the nacelle.

7

Conclusion

Due to the need for more renewable energy, interest in floating wind turbines has greatly increased over the last years. With research indicating that rogue waves occur more frequently than expected, the question arose whether rogue waves could be dangerous for these floating turbines. That was the objective that this thesis aimed to answer. First the main question will be answered, after which the sub-questions are evaluated in their chronological order. The following main research question had been established:

How threatening are rogue waves to a spar-type floating wind turbine, based on the probability of the wave occurring and the accompanying motion response?

In the literature there is no consensus on the occurrence probability of rogue waves and quantifiable statistics are seldom to never given. For this research, historical wave data from a wave buoy located off shore California is used to estimate an overall occurrence probability of four sizes rogue waves by TE and STE wave probability models. The rogue waves were embedded in a random wave series, based on their most likely wave spectrum, using a deterministic extreme wave model. With these wave time-histories, simulations were run in OrcaFlex using a publicly available OC3-Hywind model. During the simulation the turbine was assumed to be in parked condition and only the wave loading was considered. Mostly the pitch angles and nacelle accelerations are limiting for safety, due to stability criteria and sensitive components in the nacelle. These limits are imposed by turbine OEM's but are never shared publicly. Therefore, the results were compared with reference values from the literature. The dynamic response did not exceed these maximum reference values, but they can be considered quite serious as some did exceed lower thresholds. By using both the long-term occurrence probability of the rogue waves as estimated by the statistical models and the dynamic response, this research presents a new and advanced approach for a risk analysis of rogue waves to floating offshore structures. Based on the fact that for the two largest rogue waves the most conservative probability model estimates a return period of over 100 years until a 95% occurrence probability, and all four waves induced a dynamic response which did not exceed maximum reference limits, it appears that these rogue waves alone present no danger for the considered SFWT. However, ultimately this will depend on the sensitivity of the components inside the turbine, as well as the desired risk profile of the wind farm owner(s).

How do space-time extreme wave probability models compare to time-extreme models in predicting rogue waves off the Californian coast on a spatial scale relevant to floating offshore wind turbines?

The exceedance probability of the rogue crest and wave threshold was calculated in all hourly sea states by several TE and STE wave probability models. Using these probabilities different comparisons have been made to answer the considered sub-question. This paragraph presents the conclusions to this question, partly by answering the additionally formulated questions:

- *From what spatial scale do space-time extreme and time-extreme wave models yield significant differences?*

- *What is the influence of the shape of the directional wave spectrum on the predicted rogue wave occurrence?*

The influence of the spatial scale on the estimated rogue wave probability was investigated by comparing TE and STE models on the basis of maximum exceedance probability of the rogue threshold for different area sizes. For the first time, this research investigated the area size which will result in the STE model estimating higher rogue wave probabilities than the TE model. Regarding the considered TE crest models, it was observed that the Forristall model estimates the lowest probabilities, followed by the Tayfun model, and the Tayfun-Fedele model estimates the highest. Of those three models, only the Tayfun-Fedele model estimates higher probabilities than the STE2 model in two sea states, for an area size smaller than $2 \times 2 \text{m}^2$. Abnormal high wave crests such as these rogues influence the platform design height of offshore structures. Because the Tayfun-Fedele model is the most conservative TE crest model, and $2 \times 2 \text{m}^2$ is small compared to floating offshore wind turbines, incorporating the spatial dimension when evaluating rogue wave crests for a SFWT will result in the most conservative design.

Regarding the crest-to-trough models, it was observed that the STE1QD model estimates higher exceedance probabilities of the rogue threshold than the Naess model for all areas in all sea states. The Rayleigh model estimates higher probabilities than the STE1QD model in several sea states for an area size smaller than $12 \times 12 \text{m}^2$. When the area size was smaller than $2 \times 2 \text{m}^2$, the Rayleigh model estimated higher probabilities in all sea states. While evaluating the overall rogue wave probabilities where the probabilities were averaged per bin, it was observed that for the considered area of $6.5 \times 6.5 \text{m}^2$ the STE1QD model started to become more conservative than the Rayleigh model. It appears that when single maximum exceedance probabilities are compared, the Rayleigh model can be more conservative in several sea states until a STE area of $12 \times 12 \text{m}^2$, but when comparing the overall occurrence probabilities, the STE area from which the STE1QD model becomes more conservative is roughly $6.5 \times 6.5 \text{m}^2$.

The influence of the shape of the wave spectrum on the estimated rogue wave probability was investigated using two spectral bandwidth parameters which indicate whether the spectrum is narrow or wide. All four wave crest models displayed an increase in rogue crest probability as the wave spectrum became narrower. Regarding the crest-to-trough models, no clear preference was observed. These results indicate a heightened rogue crest occurrence probability for locations with frequent narrow wave spectra.

What is the dynamic response of a spar-type floating wind turbine to rogue waves with different occurrence probabilities as predicted by space-time and time-extreme wave models based on Orcaflex time-domain simulations?

Following the overall rogue wave probability analysis, four rogue waves were each embedded in random wave series, based on their most likely wave spectrum, using the MLW model. For each rogue wave five simulations were run with and without a rogue wave embedded in this random wave series. The deterministic rogue wave induced significantly more extreme motions than the heavy sea state alone. The surge, heave, pitch and nacelle acceleration were investigated, where the reported maximums were averaged over the five simulations. The biggest surge, heave and pitch response followed from simulations with the largest rogue wave. The three largest rogue waves induced nearly identical nacelle accelerations, which can be explained by the turbine having more or less favorable initial conditions before the rogue wave impact.

8

Discussion and recommendations

This chapter presents the discussion of the results and recommendations for further work. The subjects that will be discussed are presented in the same order as they have appeared in the report.

In this research, the rogue wave probability was evaluated using historical wave data obtained from a wave buoy located offshore California. This was a large 23 year data set which facilitated accurate mapping of the wave climate and subsequent probability calculations. It should be noted that this wave buoy is stationed is relatively deep water ($1646m$), which would be considered too deep for floating wind turbines. It's possible that closer to shore, where the water depth is more suitable for floating wind turbines, the wave climate is less extreme than at the wave buoy location, ultimately reducing the occurrence probability of large rogue waves.

The area size of the STE wave probability models was based on the OC3-Hywind turbine waterline diameter. These STE wave probability models are defined such that the waves are assumed to freely propagate within the area bounds. When a solid structure exists in the sea, the waves can no longer propagate within the bounds of the structure, only on the surfaces. When the area is sufficiently small compared to the wave length, the wave-structure interaction can be neglected and the current 3D models can be assumed valid. If one wants to take the wave-structure interaction into account, further research into a 2D adaptation of the STE models should be done.

The influence of the shape of the wave spectrum was investigated using two spectral bandwidth parameters. Due to the large data size, the scatter diagrams had a very wide spread of data points. The trendlines which were used to indicate a possible trend in the data therefore had low R^2 (coefficient of determination) values, which indicate a 'goodness-of-fit' of the trendlines. These trendlines should therefore not be regarded as being an exact representation of the data, but more like an indication to identify a preference.
The results of this study were related to two previous papers where the two spectral bandwidth parameters where investigated as possible rogue wave indicators. These papers did not agree on the preference of rogue waves for a more narrow or wide spectrum. Some results were in accordance with this study, while others indicated the opposite. It is possible that these spectral preferences could be dependent on the geographical location, as Cattrell concluded that rogue wave generation mechanisms are location dependent. They retrieved their data from buoys around North-America, Christou and Ewans retrieved the majority of their data from offshore platforms in the North sea, and this research evaluated data from a single buoy stationed in California. Further research could investigate the location dependence on possible spectral preferences of rogue waves to increase this understanding.

In section 5.7, the overall occurrence probability of four rogue crests and waves was calculated. During this calculation, sea states were excluded if the wave was not considered rogue in that sea state. This means that when, for example, the smallest rogue wave was considered, the highest sea states were not included in that calculation in order to uphold the rogue wave definitions, while in those high sea states that particular wave may not be so rare. It may therefore be good to note that the goal of this thesis was not to find occurrence probabilities of the most extreme waves, but to investigate rogue waves in particular, which are unexpected outliers with respect to their surrounding waves. When the only interest is the occurrence probability of ex-

treme waves, one would include all sea states in the calculation, leading to higher occurrence probabilities for all but the largest considered (rogue) wave.

Moreover, since only waves which classified as rogue were investigated in this thesis, it would be highly interesting to do further research and compare the STE and TE models on their estimation of the most probable maximum to explore the influence of the spatial dimension using a different criterion.

A deterministic extreme wave method was adopted for this research to efficiently simulate the rogue waves. Section 6.3.2 presented the process of embedding this deterministic rogue wave in a random wave series using the MLW model. Here the notion was made that the MLW model is completely deterministic on the wave peak, but as we move away from this peak the underlying wave spectrum starts to influence the wave shape, ultimately leading to slightly different rogue wave periods in each random wave series. At the moment there are no alternative deterministic models which preserve the exact period of the most likely wave shape. As the wave period influences the induced dynamic response, further research into a technique to better model this wave period can ultimately lead to a more accurate results.

As explained in section 6.4, the wave time-histories are approximated by a large amount of Airy waves which allow OrcaFlex to calculate the surface elevation and kinematics at all points. By approximating the surface elevation using Airy waves the rogue wave is essentially linearized, while in reality such a wave will be non-linear. To more accurately model the fluid dynamics of a rogue wave, one could use computational fluid dynamics (CFD). However, CFD is extremely time-consuming and should therefore only be used for specific situations. In relation to this, the results from OrcaFlex can be a very useful indicator whether further CFD analysis should be done. If the dynamic response reported in section 6.5.1, together with the estimated occurrence probability of the accompanying rogue wave, appear dangerous during the design process, it is advised to do a further CFD analysis.

During the simulations the turbine was assumed to be in parked condition, and no wind or current speed was simulated. Since the considered rogue waves are large they are likely to occur in a high sea state, which are usually accompanied by significant wind speeds. At the moment the dynamic response due to the rogue wave alone is already serious, though the maximum literature reference values are not exceeded. With the additional loading of the wind and current it's possible that these reference values are exceeded. To give a more complete picture of the dynamic response of the SFWT to a rogue wave, further research should be done to include these environmental factors.

Furthermore, since a rogue wave can occur in every sea state, it would be interesting to asses the probability of a rogue wave striking the turbine during operation. As the turbine is in operation, a large thrust force is working on a substantial distance from the center of buoyancy, which pitches the turbine. A rogue wave during operation may be smaller than the ones considered in this thesis, however combined with the heeling moment due to the thrust force, it could induce more extreme angles and motions.

The individual results from the simulations with the same rogue wave height were observed to differ relative to each other. While in general it could be observed that larger rogue waves induced more extreme motions, there where two outliers in the simulations with the third and fourth largest rogue wave which induced significantly more extreme motions compared to both their equal rogue waves and the larger rogue waves. It appears that the initial conditions before the rogue wave impact have a great influence on the induced motions. Since the time was limited and the primary focus of this study was not on the dynamic response, no further simulations or analysis were done to investigate this. It is very interesting for further research to investigate what factors cause the dynamic response to a rogue wave to increase or decrease, and how this relates to the once in a life time nature of these waves.

Appendices

A

Trendline analysis

This appendix presents three different trendline shape comparisons as addition to section 5.6 for the Tayfun, Naess and STE1QD models. Three trendlines are plotted: a linear, second order and third order line. The coefficient of determination, R^2, is mentioned in the description of the graphs. The wave crest models show similar behaviour, which is why only the Tayfun model is shown. The crest-to-trough models display no clear trend, which can be seen in the trendline analysis. The trendlines of the Rayleigh model, not shown here, are similar for the first, second and third order lines.

The Tayfun spectrum comparisons display an increase in estimated exceedance probability as the wave spectrum becomes more narrow for the three considered trendlines. Here the second and third order lines have a slope of 0 at a bandwidth value of 1 for a better fit to the data. The spread of the data points is wide, which makes the trendline less accurate in terms of the coefficient of determination. This can be seen in the low values of R^2. The second and third order trendlines show nearly identical shape and R^2 values. Other trendlines of the wave crest probability models display similar behaviour as those of the Tayfun model.

The Naess and STE1QD spectrum comparison data appear to be spread out over the bandwidth range and display no clear trend of increased rogue wave probability for a narrow or wide spectrum. The third order trendlines have the highest R^2 value but this still remains low due to the wide spread of the data. Due to the absence of a robust shape of the trendlines for the Naess and STE1QD models, the third order trendline is chosen as this has the highest R^2 value.

(a)   (b)
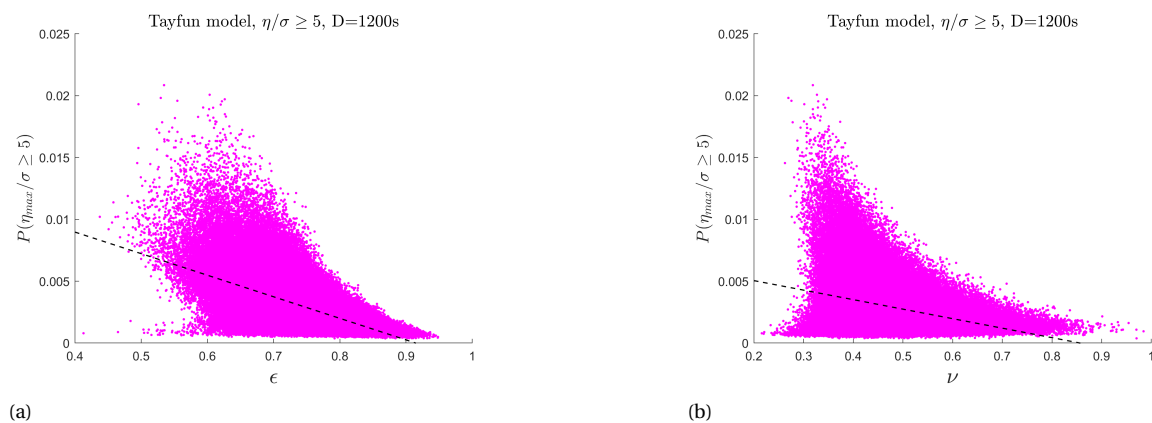
Figure A.1: Exceedance probability of the rogue wave threshold $P(\eta/\sigma \geq 5)$ for D = 20 minutes as estimated by the Tayfun model, plotted against (a) spectral width parameter ϵ, trendline is linear, $R^2 = 0.3358$ and (b) spectral width parameter ν, trendline is linear, $R^2 = 0.1021$.
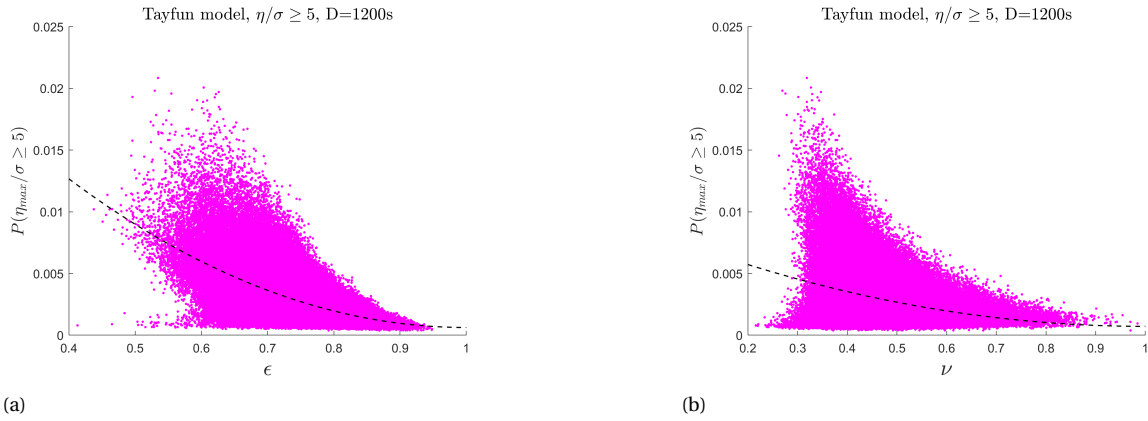
Figure A.2: Exceedance probability of the rogue wave threshold $P(\eta/\sigma \geq 5)$ for D = 20 minutes as estimated by the Tayfun model, plotted against (a) spectral width parameter ϵ, trendline is second order with slope 0 at $\epsilon = 1$, $R^2 = 0.3477$ and (b) spectral width parameter ν, trendline is second order with slope 0 at $\nu = 1$, $R^2 = 0.1053$.
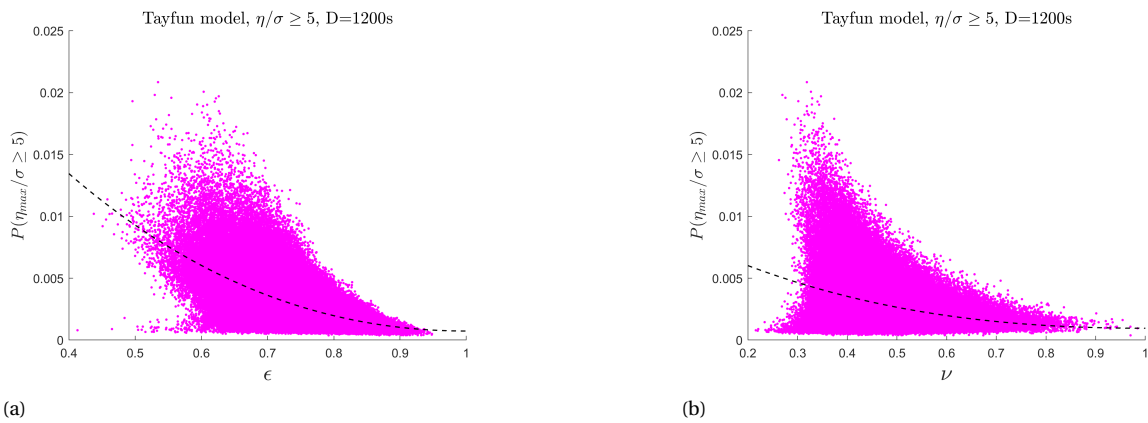
Figure A.3: Exceedance probability of the rogue wave threshold $P(\eta/\sigma \geq 5)$ for D = 20 minutes as estimated by the Tayfun model, plotted against (a) spectral width parameter ϵ, trendline is third order with slope 0 at $\epsilon = 1$, $R^2 = 0.3479$ and (b) spectral width parameter ν, trendline is third order with slope 0 at $\nu = 1$, $R^2 = 0.1055$.
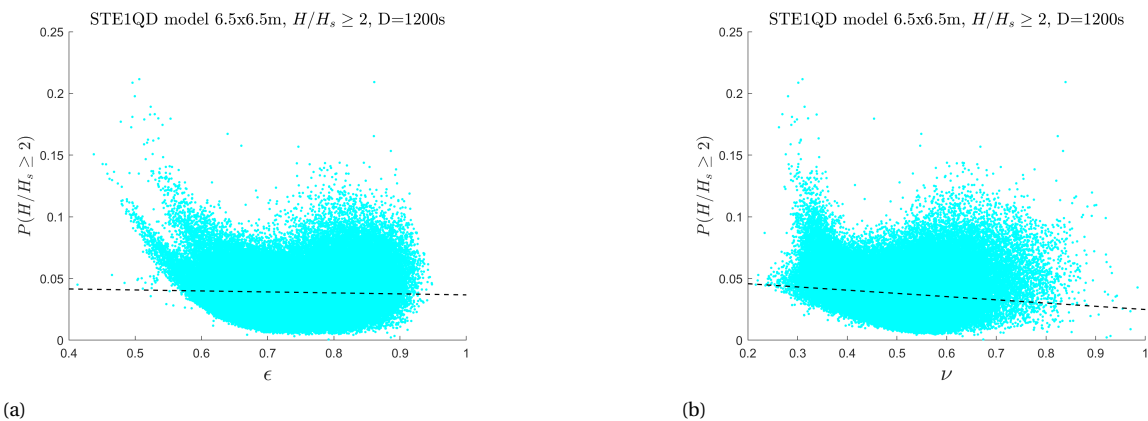
Figure A.4: Exceedance probability of the rogue wave threshold $P(H/H_s \geq 2)$ for D = 20 minutes as estimated by the STE1QD model with A=6.5x6.5m^2, plotted against (a) spectral width parameter ϵ, trendline is linear, $R^2 = 0.0011$ and (b) spectral width parameter ν, trendline is linear, $R^2 = 0.0192$.
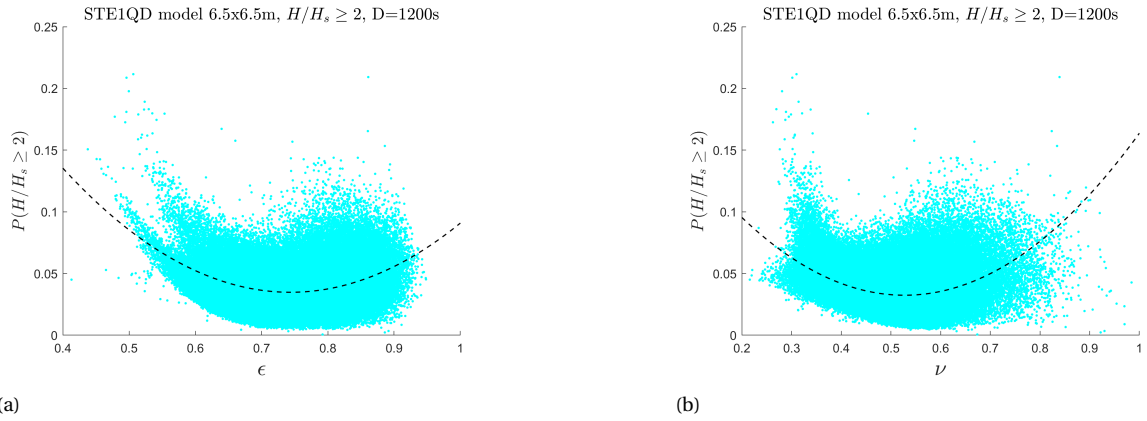
Figure A.5: Exceedance probability of the rogue wave threshold $P(H/H_s \geq 2)$ for D = 20 minutes as estimated by the STE1QD model with A=6.5x6.5m^2, plotted against (a) spectral width parameter ϵ, trendline is second order, $R^2 = 0.1087$ and (b) spectral width parameter ν, trendline is second order, $R^2 = 0.1706$.
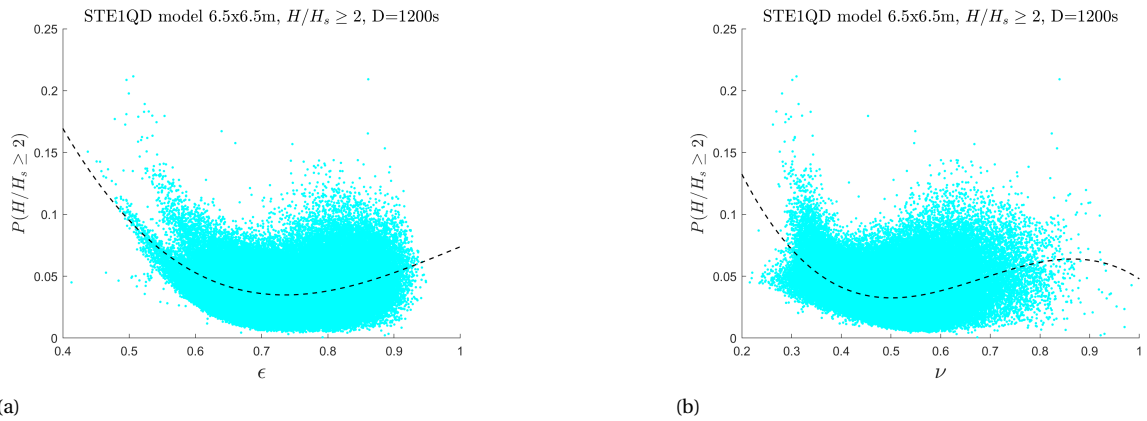
Figure A.6: Exceedance probability of the rogue wave threshold $P(H/H_s \geq 2)$ for D = 20 minutes as estimated by the STE1QD model with A=6.5x6.5m^2, plotted against (a) spectral width parameter ϵ, trendline is second order, $R^2 = 0.1106$ and (b) spectral width parameter ν, trendline is second order, $R^2 = 0.1881$.
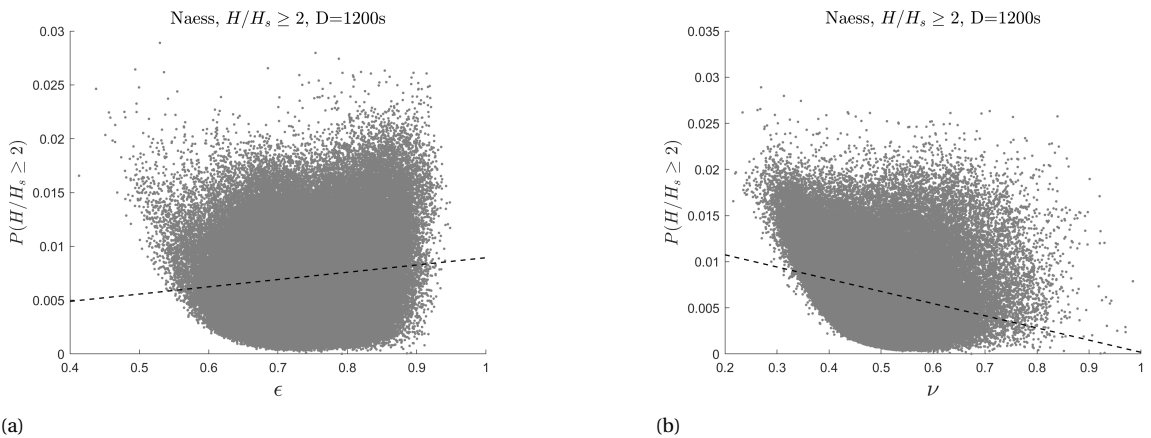
Figure A.7: Exceedance probability of the rogue wave threshold $P(H/H_s \geq 2)$ for D = 20 minutes as estimated by the Naess model, plotted against (a) spectral width parameter ϵ, trendline is linear, $R^2 = 0.0137$ and (b) spectral width parameter ν, trendline is linear, $R^2 = 0.0818$.
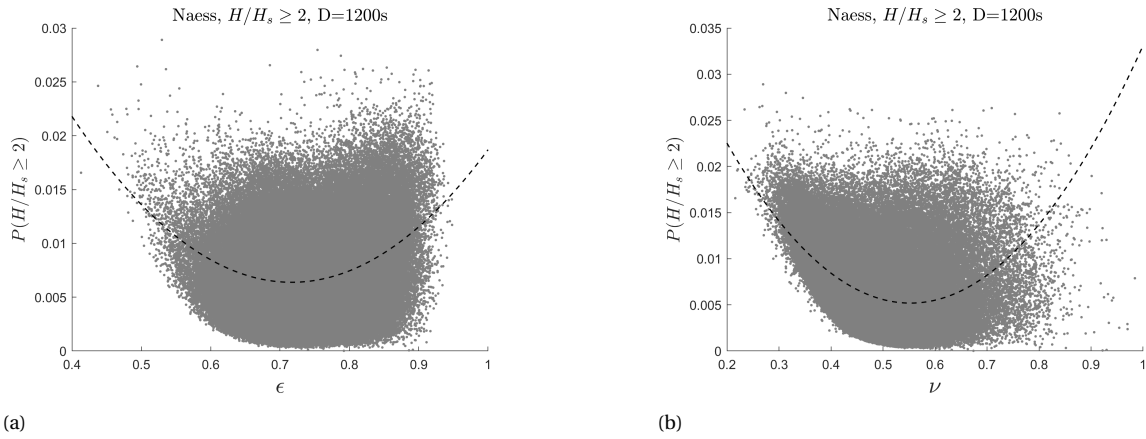
Figure A.8: Exceedance probability of the rogue wave threshold $P(H/H_s \geq 2)$ for D = 20 minutes as estimated by the Naess model, plotted against (a) spectral width parameter ϵ, trendline is second order, $R^2 = 0.0721$ and (b) spectral width parameter ν, trendline is third order, $R^2 = 0.2244$.
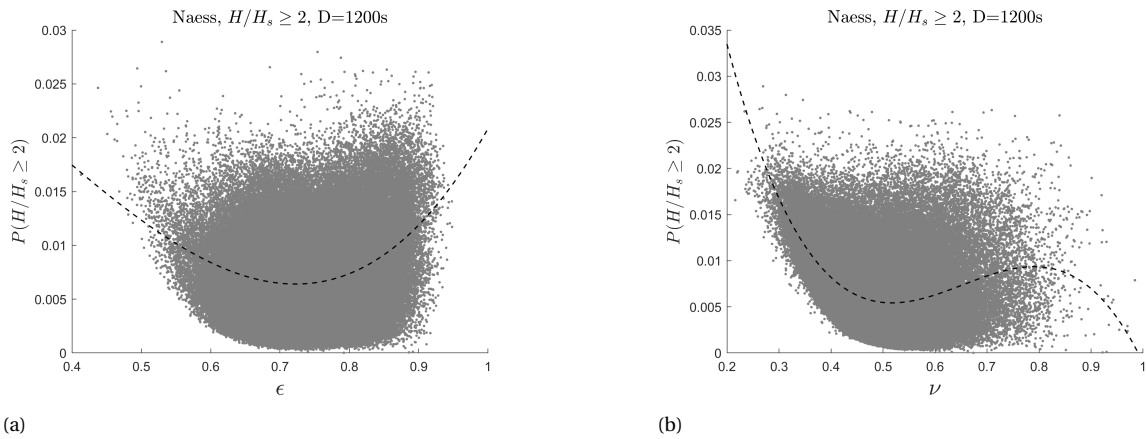
Figure A.9: Exceedance probability of the rogue wave threshold $P(H/H_s \geq 2)$ for D = 20 minutes as estimated by the Naess model, plotted against (a) spectral width parameter ϵ, trendline is third order, $R^2 = 0.0726$ and (b) spectral width parameter ν, trendline is third order, $R^2 = 0.2498$.

B

Analysis averaged probabilities

This appendix presents, for all considered probability models, comparisons between the average probability per bin and the probability resulting from the averaged input parameters in some high sea states. When calculating the overall rogue wave probabilities, an average probability has to be found per bin. The results in this appendix support the choice to directly average the exceedance probabilities per bin, since the difference between that and the probability resulting from the average parameters is very small, and it is the fastest method. The reviewed sea states are from a significant wave height of $7.5m$ and upwards, where the bin with the most sea state entries was chosen. The first section presents the tables for the wave crest models and the second section presents the tables for the crest-to-trough models.

B.1. Wave crest models

Sea state bin $7.5 < H_s \leq 8m$ and $11 < T_m \leq 12s$	Average $P(\eta/\sigma \geq 5 \mid D)$	Variance	Average parameters $P(\eta/\sigma \geq 5 \mid D)$	Difference $\Delta\%$
Foristall	0.00149	1.328e-8	0.00149	0
Tayfun	0.00244	2.062e-7	0.00240	1.67
Tayfun-Fedele	0.00469	1.681e-6	0.00450	4.22
STE2 6.5×6.5m^2	0.01184	2.566e-6	0.01175	0.77

Sea state bin $8 < H_s \leq 8.5m$ and $11 < T_m \leq 12s$	Average $P(\eta/\sigma \geq 5 \mid D)$	Variance	Average parameters $P(\eta/\sigma \geq 5 \mid D)$	Difference $\Delta\%$
Foristall	0.00166	3.746e-8	0.00164	1.22
Tayfun	0.00281	1.604e-7	0.00279	0.72
Tayfun-Fedele	0.00585	1.468e-6	0.00572	2.27
STE2 6.5×6.5m^2	0.01296	1.347e-6	0.01294	0.15

Sea state bin $8.5 < H_s \leq 9m$ and $12 < T_m \leq 13s$	Average $P(\eta/\sigma \geq 5 \mid D)$	Variance	Average parameters $P(\eta/\sigma \geq 5 \mid D)$	Difference $\Delta\%$
Foristall	0.00140	2.394e-8	0.00140	0
Tayfun	0.00245	1.215e-7	0.00243	0.82
Tayfun-Fedele	0.00487	1.039e-6	0.00476	2.31
STE2 6.5×6.5m^2	0.01126	1.163e-6	0.01122	0.36

Sea state bin $9 < H_s \leq 9.5m$ and $12 < T_m \leq 13s$	Average $P(\eta/\sigma \geq 5 \,|\, D)$	Variance	Average parameters $P(\eta/\sigma \geq 5 \,|\, D)$	Difference $\Delta\%$
Foristall	0.00145	3.437e-9	0.00145	0
Tayfun	0.00242	2.343e-8	0.00241	0.41
Tayfun-Fedele	0.00476	2.199e-7	0.00473	0.63
STE2 6.5×6.5m^2	0.01124	2.284e-7	0.01125	-0.09

Sea state bin $9.5 < H_s \leq 10m$ and $12 < T_m \leq 13s$	Average $P(\eta/\sigma \geq 5 \,|\, D)$	Variance	Average parameters $P(\eta/\sigma \geq 5 \,|\, D)$	Difference $\Delta\%$
Foristall	0.00146	0	0.00146	0
Tayfun	0.00258	0	0.00258	0
Tayfun-Fedele	0.00536	0	0.00536	0
STE2 6.5×6.5m^2	0.01164	0	0.01164	0

Sea state bin $10 < H_s \leq 10.5m$ and $13 < T_m \leq 14s$	Average $P(\eta/\sigma \geq 5 \,|\, D)$	Variance	Average parameters $P(\eta/\sigma \geq 5 \,|\, D)$	Difference $\Delta\%$
Foristall	0.00139	1.880e-10	0.00139	0
Tayfun	0.00197	5.621e-10	0.00197	0
Tayfun-Fedele	0.00354	6.594e-9	0.00354	0
STE2 6.5×6.5m^2	0.00955	1.891e-9	0.00955	0

B.2. Crest-to-trough models

Sea state bin $7.5 < H_s \leq 8m$ and $11 < T_m \leq 12s$	Average $P(\eta/\sigma \geq 5 \,|\, D)$	Variance	Average parameters $P(\eta/\sigma \geq 5 \,|\, D)$	Difference $\Delta\%$
Naess	0.00682	1.557e-6	0.00672	1.49
Rayleigh	0.03434	7.193e-7	0.03432	0.06
STE1QD 6.5×6.5m^2	0.02615	1.311e-5	0.02596	0.73

Sea state bin $8 < H_s \leq 8.5$ and $11 < T_m \leq 12$	Average $P(H/H_s \geq 2 \,|\, D)$	Variance	Average parameters $P(H/H_s \geq 2 \,|\, D)$	Difference $\Delta\%$
Naess	0.00660	4.233e-6	0.00634	4.1
Rayleigh	0.03457	8.786e-7	0.03454	0.09
STE1QD 6.5×6.5m^2	0.02550	3.790e-5	0.02497	2.12

Sea state bin $8.5 < H_s \leq 9m$ and $12 < T_m \leq 13s$	Average $P(\eta/\sigma \geq 5 \,|\, D)$	Variance	Average parameters $P(\eta/\sigma \geq 5 \,|\, D)$	Difference $\Delta\%$
Naess	0.00637	1.624e-6	0.00627	1.59
Rayleigh	0.03217	5.227e-7	0.03215	0.06
STE1QD 6.5×6.5m^2	0.02372	1.033e-5	0.02357	0.02

Sea state bin $9 < H_s \leq 9.5m$ and $12 < T_m \leq 13s$	Average $P(\eta/\sigma \geq 5 \,|\, D)$	Variance	Average parameters $P(\eta/\sigma \geq 5 \,|\, D)$	Difference $\Delta\%$
Naess	0.00678	9.298e-7	0.00672	0.89
Rayleigh	0.03201	1.498e-7	0.03201	0
STE1QD 6.5×6.5m^2	0.02493	6.456e-6	0.02486	0.28

| Sea state bin | Average | Variance | Average parameters | Difference |
$9.5 < H_s \leq 10m$ and $12 < T_m \leq 13s$	$P(\eta/\sigma \geq 5 \mid D)$		$P(\eta/\sigma \geq 5 \mid D)$	$\Delta\%$
Naess	0.00887	0	0.00887	0
Rayleigh	0.03100	0	0.03100	0
STE1QD $6.5 \times 6.5 \text{m}^2$	0.02995	0	0.02995	0

| Sea state bin | Average | Variance | Average parameters | Difference |
$10 < H_s \leq 10.5m$ and $13 < T_m \leq 14s$	$P(\eta/\sigma \geq 5 \mid D)$		$P(\eta/\sigma \geq 5 \mid D)$	$\Delta\%$
Naess	0.00660	3.919e-8	0.00660	0
Rayleigh	0.03025	3.795e-8	0.03025	0
STE1QD $6.5 \times 6.5 \text{m}^2$	0.02370	3.008e-7	002370	0

C
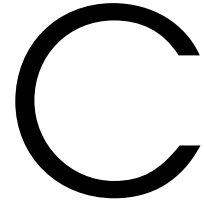
Time step sensitivity check

A time step sensitivity check is done to determine which time step should be used in the simulations, where a tradeoff between computation time and accuracy is made. If a smaller time step results in approximately the same results as the larger time step before, the larger time step is chosen to reduce simulation time.

One case is run using three different time steps: $0.1s$, $0.05s$ and $0.01s$. Here OrcaFlex' default value is $0.1s$. This is a wave series containing the largest crest-to-trough rogue wave, one where $H_{rogue} = 20.62m$. First the default value of $0.1s$ is run. When the rogue wave hits the turbine at $350s$, the simulation has trouble finding the dynamic equilibriums using multiple iterations. As explained in section 6.4.1, when after a certain number of iterations no convergence has been found, the simulation is aborted. In this case, no solution was found after 100 iterations and the simulation with the $0.1s$ time step was aborted. The default value of $0.1s$ therefore is not adequate for the simulations.

The two simulations with a time step of $0.05s$ and $0.01s$ had no trouble running at all. Table C.1 below presents the results of the simulations, where the spar surge, heave and pitch are evaluated, together with the nacelle acceleration. The values have been rounded to two decimals.

Rogue wave size $H_{rogue} = 20.62$	Max. surge [m]	Max. heave [m]	Max. pitch [°]	Max. nacelle acceleration [m/s^2]
$\Delta t = 0.05$s	16.51	2.57	6.86	3.83
$\Delta t = 0.01$s	16.52	2.57	6.86	3.78
% difference	0.06	0	0	1.3

Table C.1: A comparison of the results from the same wave series input with a time step of $0.05s$ and $0.01s$.

The surge, heave and pitch show little to no differences. The maximum nacelle acceleration shows a marginal difference of 1.3%. Based on this comparison, the choice is made to use a time step of $0.05s$ in all the simulations.

D

Appendix C

This appendix presents four images of the dynamic response of the SFWT in a wave series with a deterministic rogue wave at $350s$. Starting from lowest to highest, the results of one simulation for each size rogue wave are presented. These results are shown here to illustrate the responses observed during the whole simulation.
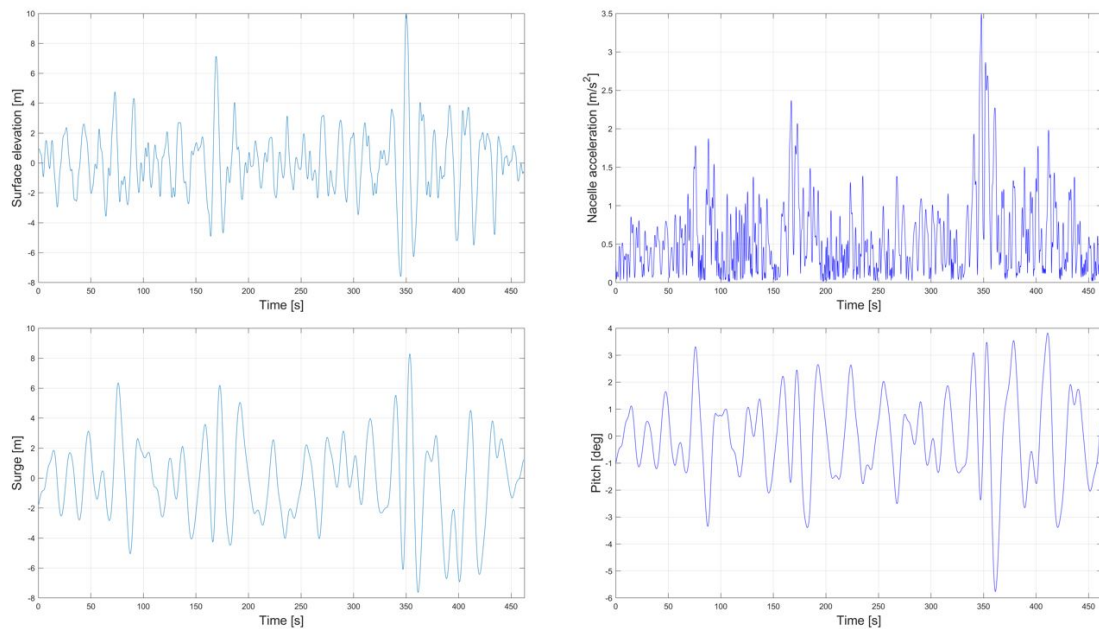
Figure D.1: A complete dynamic response of the SFWT in a wave series with a deterministic rogue wave $H_{rogue} = 17.56m$. Upper left: surge, upper right: pitch, bottom left: nacelle acceleration, bottom right: heave. Random seed 58.
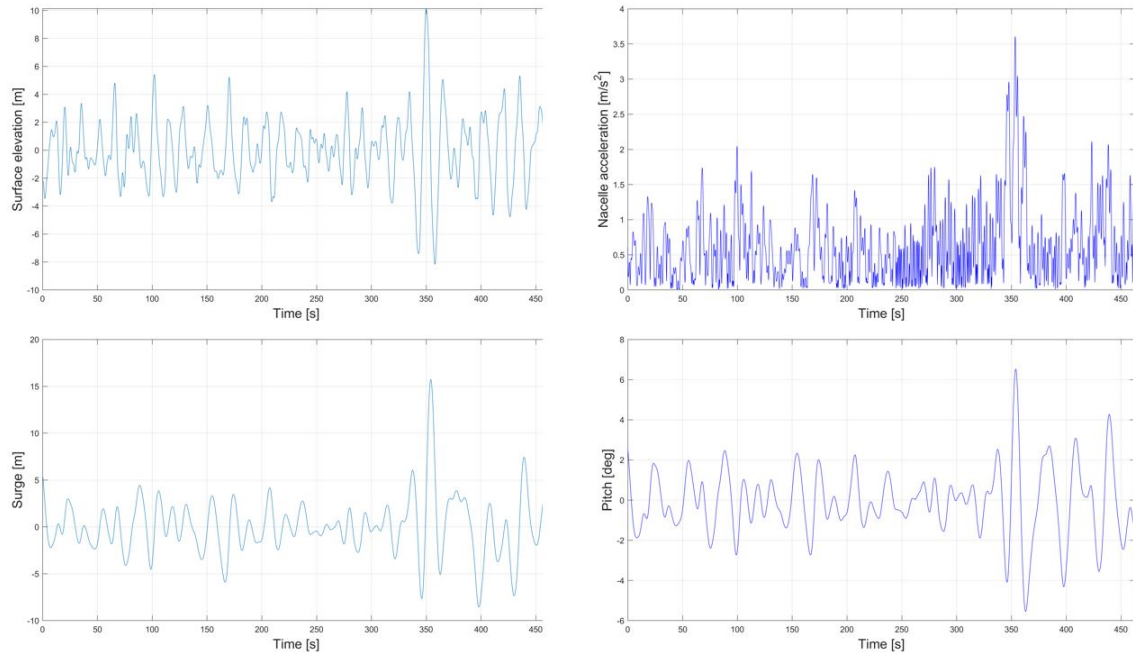
Figure D.2: A complete dynamic response of the SFWT in a wave series with a deterministic rogue wave $H_{rogue} = 18.26\,m$. Upper left: surge, upper right: pitch, bottom left: nacelle acceleration, bottom right: heave. Random seed 31.
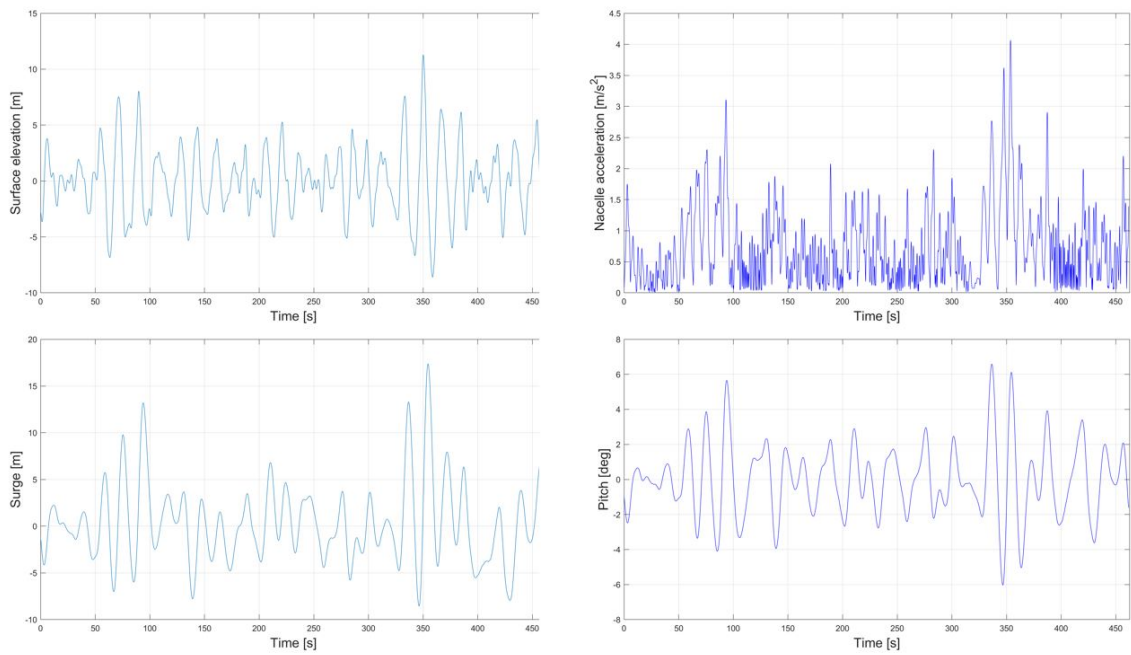
Figure D.3: A complete dynamic response of the SFWT in a wave series with a deterministic rogue wave $H_{rogue} = 19.84\,m$. Upper left: surge, upper right: pitch, bottom left: nacelle acceleration, bottom right: heave. Random seed 7.
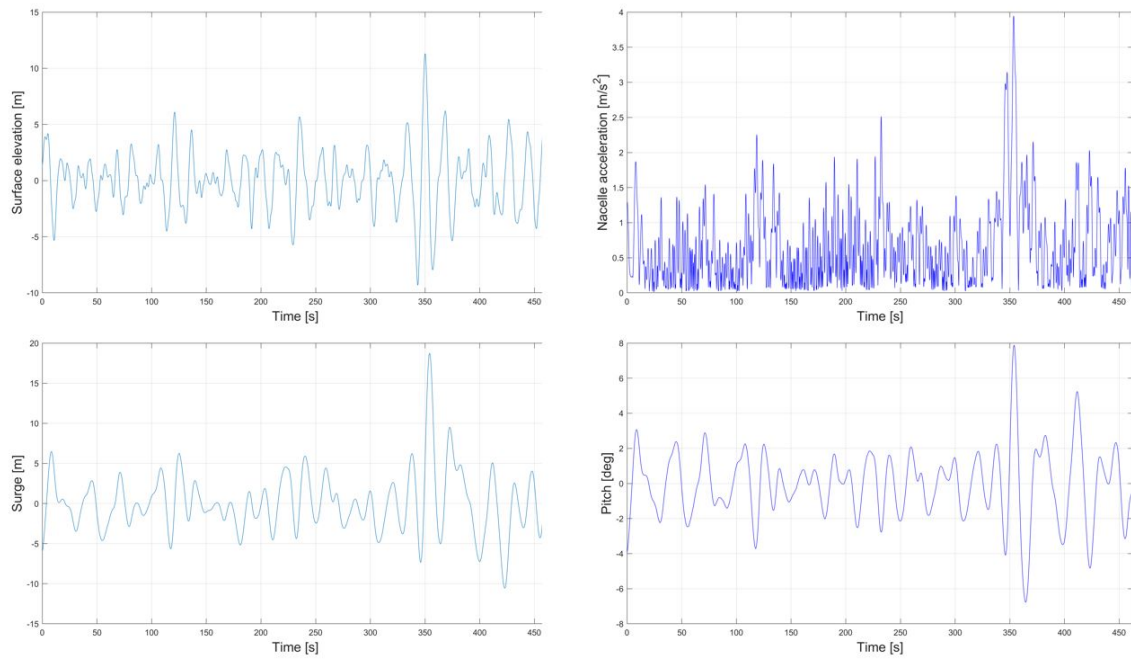
Figure D.4: A complete dynamic response of the SFWT in a wave series with a deterministic rogue wave $H_{rogue} = 20.62\,m$. Upper left: surge, upper right: pitch, bottom left: nacelle acceleration, bottom right: heave. Random seed 69.

E

Appendix E

Simulations with embedded rogue wave	Surge	Heave	Pitch	Nacelle acceleration
$H_{rogue} = 20.62m$	[m]	[m]	[m]	[m/s^2]
Sim1	18.73	2.92	7.89	3.95
Sim2	16.52	2.57	6.86	3.84
Sim3	19.41	3.18	8.36	4.00
Sim4	13.1	4.08	6.83	4.24
Sim5	16.77	2.34	5.82	3.04

Simulations with embedded rogue wave	Surge	Heave	Pitch	Nacelle acceleration
$H_{rogue} = 19.84m$	[m]	[m]	[m]	[m/s^2]
Sim1	17.34	2.66	6.56	4.07
Sim2	13.35	2.48	4.91	3.59
Sim3	12.73	2.54	6.10	3.24
Sim4	10.72	2.64	5.43	4.08
Sim5	17.34	2.23	8.71	4.17

Simulations with embedded rogue wave	Surge	Heave	Pitch	Nacelle acceleration
$H_{rogue} = 18.26m$	[m]	[m]	[m]	[m/s^2]
Sim1	15.73	1.96	6.53	3.61
Sim2	13.41	3.76	6.38	3.94
Sim3	12.94	2.53	5.22	3.49
Sim4	13.79	1.63	5.95	3.38
Sim5	20.71	2.76	10.75	4.67

Simulations with embedded rogue wave	Surge	Heave	Pitch	Nacelle acceleration
$H_{rogue} = 17.56m$	[m]	[m]	[m]	[m/s^2]
Sim1	14.13	1.85	6.70	3.91
Sim2	12.73	1.55	4.47	3.29
Sim3	19.10	2.68	9.29	4.51
Sim4	8.28	2.64	3.82	3.49
Sim5	11.12	1.35	3.90	3.23

Simulations <u>without</u> embedded rogue wave	Surge	Heave	Pitch	Nacelle acceleration
$H_{rogue} = 20.62m$	[m]	[m]	[m]	[m/s^2]
Sim1	6.48	1.67	3.07	2.51
Sim2	9.85	1.55	5.30	2.94
Sim3	9.16	1.29	4.17	2.34
Sim4	9.00	1.78	5.53	2.27
Sim5	7.81	1.78	4.19	2.10

Simulations <u>without</u> embedded rogue wave	Surge	Heave	Pitch	Nacelle acceleration
$H_{rogue} = 19.84m$	[m]	[m]	[m]	[m/s^2]
Sim1	13.28	2.18	5.69	3.10
Sim2	8.24	1.41	4.01	2.45
Sim3	8.14	1.68	3.91	2.68
Sim4	9.61	1.56	5.11	2.83
Sim5	8.29	2.23	4.59	2.80

Simulations <u>without</u> embedded rogue wave	Surge	Heave	Pitch	Nacelle acceleration
$H_{rogue} = 18.26m$	[m]	[m]	[m]	[m/s^2]
Sim1	5.89	0.98	2.55	2.03
Sim2	10.39	1.47	5.35	2.85
Sim3	5.79	1.27	2.90	2.51
Sim4	7.71	1.62	3.39	2.37
Sim5	9.27	1.77	5.31	2.45

Simulations <u>without</u> embedded rogue wave	Surge	Heave	Pitch	Nacelle acceleration
$H_{rogue} = 17.56m$	[m]	[m]	[m]	[m/s^2]
Sim1	7.63	1.39	3.82	2.00
Sim2	7.66	1.34	4.46	2.42
Sim3	8.17	1.47	3.48	2.24
Sim4	6.88	1.45	3.65	2.37
Sim5	7.34	1.21	3.25	2.44

F

Appendix D

F.1. Script: Import and sort data

```python
import os
import pickle

#Script: Import and sort data

#Define the paths to the environmental data files
Path_meteo = "C:\\Users\\tijme\\Documents\\TU Delft\\Master
↪  Offshore\\Afstuderen\\Environmental data\\NOAA\\Monterey\\Meteo\\"
Path_energy = "C:\\Users\\tijme\\Documents\\TU Delft\\Master
↪  Offshore\\Afstuderen\\Environmental data\\NOAA\\Monterey\\Energy\\"
Path_alpha1 = "C:\\Users\\tijme\\Documents\\TU Delft\\Master
↪  Offshore\\Afstuderen\\Environmental data\\NOAA\\Monterey\\Alpha1\\"
Path_alpha2 = "C:\\Users\\tijme\\Documents\\TU Delft\\Master
↪  Offshore\\Afstuderen\\Environmental data\\NOAA\\Monterey\\Alpha2\\"
Path_r1 = "C:\\Users\\tijme\\Documents\\TU Delft\\Master
↪  Offshore\\Afstuderen\\Environmental data\\NOAA\\Monterey\\r1\\"
Path_r2 = "C:\\Users\\tijme\\Documents\\TU Delft\\Master
↪  Offshore\\Afstuderen\\Environmental data\\NOAA\\Monterey\\r2\\"

Path = [Path_meteo,Path_energy, Path_alpha1, Path_alpha2, Path_r1, Path_r2]

filelist_m = os.listdir(Path_meteo)
filelist_e = os.listdir(Path_energy)
filelist_a1 = os.listdir(Path_alpha1)
filelist_a2 = os.listdir(Path_alpha2)
filelist_r1 = os.listdir(Path_r1)
filelist_r2 = os.listdir(Path_r2)

filelist = []

filelist.append(filelist_m)
filelist.append(filelist_e)
filelist.append(filelist_a1)
filelist.append(filelist_a2)
filelist.append(filelist_r1)
filelist.append(filelist_r2)

data =[]
```

```python
#Here all data coming from the 6 subfolders are imported.
#For each parameter the yearly data is appended in a list thus containing all years.
#Data structure first index: 0 'Meteo', 1 'Energy', 2 'Alpha1', 3 'Alpha2', 4 'r1', 5
↪   'r2'
#Data structure second index: Year
#Data structure third index: Hour
#Data structure fourth index: Column

for j in range(len(filelist)):
    data_all_years = []
    for i in filelist[j]:
        if i.endswith(".txt"):
            with open(Path[j] + i, 'r') as f:
                data_year =[]
                next(f)
                for line in f:
                    stripped_line = line.strip()
                    line_list = [float(x) for x in stripped_line.split()]
                    data_year.append(line_list)
            data_all_years.append(data_year)
    data.append(data_all_years)


#Here the first corrupt data lines are filtered out. Corrupt data is displayed as a
↪   '999' entry.
#Therefore the criterium of column 8 < 900 is adopted. Column 8 should be normal data
#in all data files.

data_sorted = []
for k in range(len(data)):                    #Parameter
    data_sorted_parameter =[]
    for j in range(len(data[k])):             #Year
        data_sorted_year =[]
        for i in range(len(data[k][j])):      #Select line
            if k == 0:                                    #Select the meteo file
                if j == 22:                               #Last year of the set
                    if data[k][j][i][4] == 40:            #Only select data sampled at
                    ↪   40 min
                        if len(data[k][j][1]) >17:        #Some meteo files have an
                        ↪   extra column
                            if data[k][j][i][8] < 90:     #Corrupt meteo data is 99
                                data_sorted_year.append(data[k][j][i])
                        else:
                            if data[k][j][i][7] < 90:
                                data_sorted_year.append(data[k][j][i])
                else:
                    if len(data[k][j][1]) >17:
                            if data[k][j][i][8] < 90:
                                data_sorted_year.append(data[k][j][i])
                    else:
                            if data[k][j][i][7] < 90:
                                data_sorted_year.append(data[k][j][i])
            else:
                if data[k][j][i][8] < 900:                #Other corrupt data is
                ↪   999
```

```python
                data_sorted_year.append(data[k][j][i])
            data_sorted_parameter.append(data_sorted_year)
        data_sorted.append(data_sorted_parameter)



#Since we need input from all 6 data files it's important that there are no
↪   timestamps for
#which data from one of the files is missing. Therefore all remaining dates in the
↪   sorted data
#files are extracted so that they can be compared. Incomplete timestamps (not all 6
↪   files
#contain it) will be removed later on.

dates = []
for k in range(len(data_sorted)): #Parameter
    dates_parameter = []
    for j in range(len(data[k])): #Year
        dates_year = []
        for i in range(len(data_sorted[k][j])): #Lines in year
            date = str(data_sorted[k][j][i][0])+str(data_sorted[k][j][i][1])+str(d↓
            ↪   ata_sorted[k][j][i][2])+str(data_sorted[k][j][i][3])
            dates_year.append(date)
        dates_parameter.append(dates_year)
    dates.append(dates_parameter)




#The code below compares the available dates of one parameter to those of the other
#parameters and adds the differences to a list. This list is later used to exclude
↪   all dates
#for which certain information is missing.
#Note: The structure is different than above. First index is year, then parameter
differences = []
for j in range(len(dates[0])): #Year
    diff_parameter = []
    for k in range(len(dates)): #Parameter
        if k == 0:
            a = [1,2,3,4,5]
        elif k ==1:
            a = [0,2,3,4,5]
        elif k ==2:
            a = [0,1,3,4,5]
        elif k ==3:
            a = [0,1,2,4,5]
        elif k ==4:
            a = [0,1,2,3,5]
        elif k ==5:
            a = [0,1,2,3,4]

        diff1 = list(list(set(dates[k][j])-set(dates[a[0]][j])) +
        ↪   list(set(dates[a[0]][j])-set(dates[k][j])))
        diff2 = list(list(set(dates[k][j])-set(dates[a[1]][j])) +
        ↪   list(set(dates[a[1]][j])-set(dates[k][j])))
        diff3 = list(list(set(dates[k][j])-set(dates[a[2]][j])) +
        ↪   list(set(dates[a[2]][j])-set(dates[k][j])))
```

```python
        diff4 = list(list(set(dates[k][j])-set(dates[a[3]][j])) +
         ↪   list(set(dates[a[3]][j])-set(dates[k][j])))
        diff5 = list(list(set(dates[k][j])-set(dates[a[4]][j])) +
         ↪   list(set(dates[a[4]][j])-set(dates[k][j])))


        diff_parameter.append(diff1+diff2+diff3+diff4+diff5)
    differences.append(diff_parameter)

#Append all corrected data

data_good = []
for k in range(len(data_sorted)): #parameter
    data_good_parameter = []
    for j in range(len(data_sorted[k])): #year
        data_good_year = []
        for i in range(len(data_sorted[k][j])): #lines
            string = str(data_sorted[k][j][i][0])+str(data_sorted[k][j][i][1])+str(d↵
             ↪   ata_sorted[k][j][i][2])+str(data_sorted[k][j][i][3])
            if string not in differences[j][k]:
                data_good_year.append(data_sorted[k][j][i])
        data_good_parameter.append(data_good_year)
    data_good.append(data_good_parameter)


#Print all data to one file
outfile = open('data_good','wb')
pickle.dump(data_good,outfile)
outfile.close()

#Print data of seperate years to pickle files
path_pickle = "C:\\Users\\tijme\\Documents\\TU Delft\\Master
 ↪   Offshore\\Afstuderen\\Environmental data\\Python\\Pickle_data"

name =['\\data_1998', '\\data_1999', '\\data_2000','\\data_2001', '\\data_2002',
 ↪   '\\data_2003','\\data_2004',
        '\\data_2005', '\\data_2006','\\data_2007', '\\data_2008',
         ↪   '\\data_2009','\\data_2010', '\\data_2011', '\\data_2012',
        '\\data_2013', '\\data_2014','\\data_2015', '\\data_2016',
         ↪   '\\data_2017','\\data_2018', '\\data_2019', '\\data_2020']


for j in range(len(data_good[0])): #year
    data_year =[]
    for k in range(len(data_good)): #parameter
        data_year.append(data_good[k][j])
        file = open(path_pickle + name[j],'wb')
        pickle.dump(data_year,file)
        file.close()
```

F.2. Script: Calculate spectral moments and input parameters

```python
import numpy as np
import math as m
import pickle



#Import data

data_energy = []
with open('C:\\Users\\tijme\\Documents\\TU Delft\\Master
 Offshore\\Afstuderen\\Environmental
 data\\NOAA\\Monterey\\Energy\\energy_2020.txt') as energy:
    next(energy)
    for line in energy:

        stripped_line = line.strip()
        line_list = [float(x) for x in stripped_line.split()]
        data_energy.append(line_list)

data_alpha1 = []
with open('C:\\Users\\tijme\\Documents\\TU Delft\\Master
 Offshore\\Afstuderen\\Environmental
 data\\NOAA\\Monterey\\Alpha1\\alpha1_2020.txt') as alpha1:
    next(alpha1)
    for line in alpha1:

        stripped_line = line.strip()
        line_list = [float(x) for x in stripped_line.split()]
        data_alpha1.append(line_list)

data_alpha2 = []
with open('C:\\Users\\tijme\\Documents\\TU Delft\\Master
 Offshore\\Afstuderen\\Environmental
 data\\NOAA\\Monterey\\Alpha2\\alpha2_2020.txt') as alpha2:
    next(alpha2)
    for line in alpha2:

        stripped_line = line.strip()
        line_list = [float(x) for x in stripped_line.split()]
        data_alpha2.append(line_list)

data_r1 = []
with open('C:\\Users\\tijme\\Documents\\TU Delft\\Master
 Offshore\\Afstuderen\\Environmental data\\NOAA\\Monterey\\r1\\r1_2020.txt') as
 r1:
    next(r1)
    for line in r1:

        stripped_line = line.strip()
        line_list = [float(x) for x in stripped_line.split()]
        data_r1.append(line_list)

data_r2 = []
```

```python
with open('C:\\Users\\tijme\\Documents\\TU Delft\\Master
↪  Offshore\\Afstuderen\\Environmental data\\NOAA\\Monterey\\r2\\r2_2020.txt') as
↪  r2:
    next(r2)
    for line in r2:

        stripped_line = line.strip()
        line_list = [float(x) for x in stripped_line.split()]
        data_r2.append(line_list)

data_meteo = []
with open('C:\\Users\\tijme\\Documents\\TU Delft\\Master
↪  Offshore\\Afstuderen\\Environmental data\\NOAA\\Monterey\\Meteo\\meteo_2020.txt')
↪  as meteo:
    next(meteo)
    for line in meteo:
        stripped_line = line.strip()
        line_list = [float(x) for x in stripped_line.split()]
        data_meteo.append(line_list)

#Here the sorted data from the script 'Import_data' is loaded from a pickle file.
infile = open("C:\\Users\\tijme\\Documents\\TU Delft\\Master
↪  Offshore\\Afstuderen\\Environmental data\\Python\\Pickle_data\\data_2020", 'rb')
data_year = pickle.load(infile)
infile.close()

#Here the paths are defined to write the pickle data files containing the different
↪  parameters
path_foristall = "C:\\Users\\tijme\\Documents\\TU Delft\\Master
↪  Offshore\\Afstuderen\\Environmental data\\Python\\Pickle_Foristall"
path_tayfun = "C:\\Users\\tijme\\Documents\\TU Delft\\Master
↪  Offshore\\Afstuderen\\Environmental data\\Python\\Pickle_Tayfun"
path_ste = "C:\\Users\\tijme\\Documents\\TU Delft\\Master
↪  Offshore\\Afstuderen\\Environmental data\\Python\\Pickle_STE"

#Define constants
radian_array = np.linspace(2*np.pi/36, 2*np.pi,36)
radian_list = radian_array.tolist()

#Frequency array for the 'short' sampling frequency of 0.1Hz until 0.35Hz

freq_array_s = np.linspace(0.03,0.35,33)
freq_list_s = freq_array_s.tolist()
freq_matrix_s = np.ones((36,33))*freq_array_s

#Custom frequency array for the sampling frequency of 0.0325 to 0.48. Delta_f changes
↪  throughout...

freq_list_l = [0.02,.0325,.0375,  .0425,  .0475,  .0525,  .0575,  .0625,  .0675,
↪  .0725,  .0775,  .0825,  .0875,  .0925,  .1000,  .1100,  .1200,  .1300,  .1400,
↪  .1500,  .1600,  .1700,  .1800,  .1900,  .2000,  .2100,  .2200,  .2300,  .2400,
↪  .2500,  .2600,  .2700,  .2800,  .2900,  .3000,  .3100,  .3200,  .3300, .3400,
↪  .3500,  .3650,  .3850,  .4050,  .4250,  .4450,  .4650,  .4850]
freq_array_l =np.array(freq_list_l)
freq_matrix_l = np.ones((36,47))*freq_array_l
```

```python
#Directional matrix produces the right result compared to my excel file. Checked
↪   twice
def directional_matrix(meteo,energy,alpha1,alpha2,r1,r2,radian_list):
    dir_all = []

    if len(meteo) > 17: #Threshold for different sampling
        wd = meteo[11]
    else:
        wd = meteo[10]


    for i in range(len(radian_list)):
        dir_row = []

        if len(alpha1)<40: #Threshold for different sampling
            for j in range(4, len(alpha1)):

                D   = (1/np.pi)*(0.5+(2/3)*(r1[j]/100)*m.cos(rad↓
                ↪   ian_list[i]-(alpha1[j]-wd↓
                ↪   +90)/180*np.pi)+(r2[j]/100)*(1/6)*m.cos(2*(rad↓
                ↪   ian_list[i]-(alpha2[j]-wd+90)/180*np.pi)))
                dir_row.append(D)
            dir_all.append(dir_row)

        else:
            for j in range(5, len(alpha1)):
                D   = (1/np.pi)*(0.5+(2/3)*(r1[j]/100)*m.cos(rad↓
                ↪   ian_list[i]-(alpha1[j]-wd↓
                ↪   +90)/180*np.pi)+(r2[j]/100)*(1/6)*m.cos(2*(rad↓
                ↪   ian_list[i]-(alpha2[j]-wd+90)/180*np.pi)))
                dir_row.append(D)
            dir_all.append(dir_row)


    dir_matrix = np.array(dir_all)

    return(dir_matrix)

#Energy matrix procudes the right result compared to my excel file. Checked twice
def energy_matrix(dir_matrix,energy,alpha1):

    delta_theta = (2*np.pi)/36

    if len(alpha1)<40:
        delta_f = 0.01
    else:
        delta_f =
        ↪   [0.0125,        0.005,        0.005,        0.005,        0.005,        0.005,        0.

    #print(data_energy)

    energy_list = []
    if len(alpha1)<40:     #Threshold for different sampling
        for i in range(4,37):
            energy_list.append(energy[i])
```

```python
    else:
        for i in range(5,52):
            energy_list.append(energy[i])

    energy_vector = np.array(energy_list)
    energy_matrix = dir_matrix*energy_vector*delta_theta*delta_f


    return(energy_matrix)



def kx(freq_list_s,freq_list_l,alpha1,radian_list):

    k_vector = []
    if len(alpha1) <40: #Threshold for different sampling
        for i in range(len(freq_list_s)):
            k = ((freq_list_s[i]*2*np.pi)**2)/9.81
            k_vector.append(k)
    else:
        for i in range(len(freq_list_l)):
            k = ((freq_list_l[i]*2*np.pi)**2)/9.81
            k_vector.append(k)

    kx_list = []
    for j in range(len(radian_list)):
        kx_row =[]
        for i in range(len(k_vector)):
            #Counterintuitively, due to the way the degrees are defined we have to
            ↪  use sin()
            k_x = k_vector[i]*m.sin(radian_list[j])
            kx_row.append(k_x)
        kx_list.append(kx_row)

    kx_array =np.array(kx_list)
    return(kx_array)

def ky(freq_list_s,freq_list_l,alpha1,radian_list):

    k_vector = []
    if len(alpha1) <40: #Threshold for different sampling
        for i in range(len(freq_list_s)):
            k = ((freq_list_s[i]*2*np.pi)**2)/9.81
            k_vector.append(k)
    else:
        for i in range(len(freq_list_l)):
            k = ((freq_list_l[i]*2*np.pi)**2)/9.81
            k_vector.append(k)

    ky_list = []
    for j in range(len(radian_list)):
        ky_row =[]
        for i in range(len(k_vector)):
            #Counterintuitively, due to the way the degrees are defined we have to
            ↪  use cos()
            ky = k_vector[i]*m.cos(radian_list[j])
            ky_row.append(ky)
```

```python
            ky_list.append(ky_row)

    ky_array =np.array(ky_list)
    return(ky_array)


def moments(en_matrix,kx_matrix,ky_matrix,freq_matrix_s, freq_matrix_l,alpha1):

    #Define the coefficients for the directional moments:
    i_coef = [0,0,2,0,1,0,1,0,0] #m000, m002, m200 ,m020, m101, m011, m110, m001,
    ↪   m004
    j_coef = [0,0,0,2,0,1,1,0,0] #m000, m002, m200 ,m020, m101, m011, m110, m001,
    ↪   m004
    l_coef = [0,2,0,0,1,1,0,1,4] #m000, m002, m200 ,m020, m101, m011, m110, m001,
    ↪   m004

    dir_moments = []

    for i in range(len(i_coef)):
        if len(alpha1) <40: #Threshold for different sampling
            total_matrix =
            ↪   (kx_matrix**i_coef[i])*(ky_matrix**j_coef[i])*(freq_matrix_s**l_coef[i])*en_matrix
            moment = total_matrix.sum()
            dir_moments.append(moment)
        else:
            total_matrix =
            ↪   kx_matrix**i_coef[i]*ky_matrix**j_coef[i]*freq_matrix_l**l_coef[i]*en_matrix
            dir_moments.append(total_matrix.sum())


    return(dir_moments)

#Parameters necessary for Tayfun model. Compared to excel
def parameters_T(dir_moments):
    m000 = dir_moments[0]
    m002 = dir_moments[1]
    m001 = dir_moments[7]
    m004 = dir_moments[8]

    e = m.sqrt(1-(m002**2/(m000*m004)))
    v = m.sqrt(m000*m002/(m001**2)-1)
    mu_m = m.sqrt(m000)*((2*np.pi*m001/m000)**2)/9.81

    mu = mu_m*(1-v+v**2)


    parameters_t = []
    parameters_t.append(mu)
    parameters_t.append(mu_m)
    parameters_t.append(e)
    parameters_t.append(v)

    return(parameters_t)

#Parameters necessary for Space-Time extreme model. Compared to excel
def parameters_ST(dir_moments):
    #order m000, m002, m200 ,m020, m101, m011, m110
```

```python
    Tm = m.sqrt(dir_moments[0]/dir_moments[1])
    Lx = 2*np.pi*m.sqrt(dir_moments[0]/dir_moments[2])
    Ly = 2*np.pi*m.sqrt(dir_moments[0]/dir_moments[3])
    a_xt = dir_moments[4]/m.sqrt(dir_moments[2]*dir_moments[1])
    a_yt = dir_moments[5]/m.sqrt(dir_moments[3]*dir_moments[1])
    a_xy = dir_moments[6]/m.sqrt(dir_moments[2]*dir_moments[3])
    parameters =[]
    parameters.append(Tm)
    parameters.append(Lx)
    parameters.append(Ly)
    parameters.append(a_xt)
    parameters.append(a_yt)
    parameters.append(a_xy)
    return(parameters)

#Parameters necessary for Foristall model. Compared to excel
def parameters_F(dir_moments,meteo):

    if len(meteo) > 17: #Threshold for different sampling
        Hs = meteo[8]
    else:
        Hs = meteo[7]

    T1 = dir_moments[0]/dir_moments[7]   #spectral mean wave period
    s1 = (2*np.pi/9.81)*(Hs/T1**2)   #steepness
    omega_1 = 1/T1*2*np.pi
    k1 = omega_1**2/9.81
    d = 1646 #Depth of buoy in meters

    Ur = Hs/((k1**2)*(d**3))
    alpha = 0.3536 + 0.2568*s1+0.08*Ur
    beta = 2-1.7912*s1-0.5302*Ur+0.284*Ur**2



    foristall_par = []
    foristall_par.append(alpha)
    foristall_par.append(beta)

    return(foristall_par)

def main():

    parameters_ste = []
    parameters_t = []
    parameters_f = []
    for i in range(len(data_year[0])): #Iterate over all lines data set

        #Calculate all necessary matrices
        dir_matrix =
        ↪  directional_matrix(data_year[0][i],data_year[1][i],data_year[2][i],d↓
        ↪  ata_year[3][i],data_year[4][i],data_year[5][i],radian_list)
        en_matrix = energy_matrix(dir_matrix,data_year[1][i],data_year[2][i])
        kx_matrix = kx(freq_list_s,freq_list_l,data_year[2][i],radian_list)
        ky_matrix = ky(freq_list_s,freq_list_l,data_year[2][i],radian_list)
```

```python
            #Calculate directional spectral moments
            dir_moments =
            ↪  moments(en_matrix,kx_matrix,ky_matrix,freq_matrix_s,freq_matrix_l,d⌋
            ↪  ata_year[2][i])

            #Calculate the probability model parameters and append them to a list
            parameters_ste.append(parameters_ST(dir_moments))
            parameters_t.append(parameters_T(dir_moments))
            parameters_f.append(parameters_F(dir_moments,data_year[0][i]))

    #Foristall
    file_f = open(path_foristall + '\\Foristall_2020','wb')
    pickle.dump(parameters_f,file_f)
    file_f.close()

    #Tayfun
    file_t = open(path_tayfun + '\\Tayfun_2020','wb')
    pickle.dump(parameters_t,file_t)
    file_t.close()

    #STE
    file_ste = open(path_ste + '\\STE_2020','wb')
    pickle.dump(parameters_ste,file_ste)
    file_ste.close()

if __name__ == "__main__":
  main()
```

F.3. Script: Probability models

```python
import pickle
import math as m
import numpy as np
from scipy.optimize import fsolve


#Here the paths are defined to the pickle data files containing the different
↪   parameters
path_foristall1 = "C:\\Users\\tijme\\Documents\\TU Delft\\Master
↪   Offshore\\Afstuderen\\Environmental data\\Python\\Pickle_Foristall"
path_tayfun1 = "C:\\Users\\tijme\\Documents\\TU Delft\\Master
↪   Offshore\\Afstuderen\\Environmental data\\Python\\Pickle_Tayfun"
path_ste = "C:\\Users\\tijme\\Documents\\TU Delft\\Master
↪   Offshore\\Afstuderen\\Environmental data\\Python\\Pickle_STE"
path_autocor = "C:\\Users\\tijme\\Documents\\TU Delft\\Master
↪   Offshore\\Afstuderen\\Environmental data\\Python\\Pickle_autocor"



#Here the paths are defined to write the probability data to different folders
path_rayleigh = "C:\\Users\\tijme\\Documents\\TU Delft\\Master
↪   Offshore\\Afstuderen\\Environmental data\\Python\\Probabilities\\Rayleigh"
path_foristall = "C:\\Users\\tijme\\Documents\\TU Delft\\Master
↪   Offshore\\Afstuderen\\Environmental data\\Python\\Probabilities\\Foristall"
path_tayfun = "C:\\Users\\tijme\\Documents\\TU Delft\\Master
↪   Offshore\\Afstuderen\\Environmental data\\Python\\Probabilities\\Tayfun"
path_tayfun_fedele = "C:\\Users\\tijme\\Documents\\TU Delft\\Master
↪   Offshore\\Afstuderen\\Environmental data\\Python\\Probabilities\\Tayfun_Fedele"
path_ste1 = "C:\\Users\\tijme\\Documents\\TU Delft\\Master
↪   Offshore\\Afstuderen\\Environmental data\\Python\\Probabilities\\STE1"
path_ste2 = "C:\\Users\\tijme\\Documents\\TU Delft\\Master
↪   Offshore\\Afstuderen\\Environmental data\\Python\\Probabilities\\STE2"

path_rayleigh_cor = "C:\\Users\\tijme\\Documents\\TU Delft\\Master
↪   Offshore\\Afstuderen\\Environmental data\\Python\\Probabilities\\Rayleigh_cor"
path_ste1QD = "C:\\Users\\tijme\\Documents\\TU Delft\\Master
↪   Offshore\\Afstuderen\\Environmental data\\Python\\Probabilities\\STE1_QD"

def Rayleigh(meteo,Tm):

    #This function calculates the Rayleigh WAVE HEIGHT distribution

    if len(meteo) > 17: #Threshold for different sampling
        Hs = meteo[8]
    else:
        Hs = meteo[7]

    #Vector with different H/Hs ratios
    z =
    ↪   [1,1.1,1.2,1.3,1.4,1.5,1.6,1.7,1.8,1.9,2,2.1,2.2,2.3,2.4,2.5,2.6,2.7,2.8,2.9,3]
    #z =
    ↪   [2,2.1,2.2,2.3,2.4,2.5,2.6,2.7,2.8,2.9,3,3.1,3.2,3.3,3.4,3.5,3.6,3.7,3.8,3.9,4,4.1,4.2,4.3,4.
    #Define the duration [s]
    d = 1200 #s

    #Calculate average number of waves
    N = d/Tm
```

```python
    p_r = []
    p_r.append(meteo[0])
    p_r.append(meteo[1])
    p_r.append(meteo[2])
    p_r.append(meteo[3])
    p_r.append(Hs)

    #Calculate the probability of exceedance during 20 minutes
    for i in range(len(z)):
        pr = m.exp(-2*(z[i])**2)
        prob_20 = 1-(1-pr)**N
        p_r.append(prob_20)

    return(p_r)

def Bandwidth_rayleigh(meteo,Tm,auto_cor):

    #This function calculates the bandwidth corrected Rayleigh WAVE HEIGHT
    ↪   distribution

    if len(meteo) > 17: #Threshold for different sampling
        Hs = meteo[8]
    else:
        Hs = meteo[7]

    #Vector with different H/Hs ratios
    z =
    ↪   [1,1.1,1.2,1.3,1.4,1.5,1.6,1.7,1.8,1.9,2,2.1,2.2,2.3,2.4,2.5,2.6,2.7,2.8,2.9,3]
    #Rogue specific vector
    #z =
    ↪   [2,2.1,2.2,2.3,2.4,2.5,2.6,2.7,2.8,2.9,3,3.1,3.2,3.3,3.4,3.5,3.6,3.7,3.8,3.9,4,4.1,4.2,4.3,4.
    #Define the duration [s]
    d = 1200 #s

    #Calculate average number of waves
    N = d/Tm

    #Extract psi
    psi_star = auto_cor[0]

    p_r = []
    p_r.append(meteo[0])
    p_r.append(meteo[1])
    p_r.append(meteo[2])
    p_r.append(meteo[3])
    p_r.append(Hs)

    #Calculate the probability of exceedance during 20 minutes
    for i in range(len(z)):
        pr = m.exp(-(4/(1-psi_star))*(z[i])**2)
        prob_20 = 1-(1-pr)**N
        p_r.append(prob_20)

    return(p_r)
```

```python
def Foristall(parameters_f,meteo,Tm):
    if len(meteo) > 17: #Threshold for different sampling
        Hs = meteo[8]
    else:
        Hs = meteo[7]

    #Define the duration [s]
    d = 1200 #s

    #Calculate average number of waves
    N = d/Tm

    #Different size rogue wave thresholds, ranging from eta = 1-1.5 Hs
    eta =
    ↪ [0.5*Hs,0.55*Hs,0.6*Hs,0.65*Hs,0.7*Hs,0.75*Hs,0.8*Hs,0.85*Hs,0.9*Hs,0.95*Hs,Hs,1.05*Hs,1.1*H
    #Rogue
    #eta =
    ↪ [1.25*Hs,1.275*Hs,1.3*Hs,1.325*Hs,1.35*Hs,1.375*Hs,1.4*Hs,1.425*Hs,1.45*Hs,1.475*Hs,1.5*Hs,1
    ↪ 1.85*Hs,1.875*Hs,1.9*Hs,1.925*Hs,1.95*Hs,1.975*Hs,2*Hs,2.025*Hs,2.05*Hs,2.075*Hs,2.1*Hs,2.12
    alpha = parameters_f[0]
    beta = parameters_f[1]

    p_f = []
    #Add the timestamps to the probability list for later use
    p_f.append(meteo[0])
    p_f.append(meteo[1])
    p_f.append(meteo[2])
    p_f.append(meteo[3])
    p_f.append(Hs)

    #Calculate the probability of exceedance during 20 minutes
    for i in range(len(eta)):
        pf = m.exp(-(eta[i]/(alpha*Hs))**beta)
        prob_20 = 1-(1-pf)**N
        p_f.append(prob_20)



    return p_f

def Tayfun(parameters_t,meteo,Tm):
    if len(meteo) > 17: #Threshold for different sampling
        Hs = meteo[8]
    else:
        Hs = meteo[7]

    #Define the duration [s]
    d = 1200 #s

    #Calculate average number of waves
    N = d/Tm

    #Vector with ratios eta/sigma
    xi = [2,2.2,2.4,2.6,2.8,3,3.2,3.4,3.6,3.8,4,4.2,4.4,4.6,4.8,5,5.2,5.4,5.6,5.8,6]
```

```
    #xi =
    ↪   [5,5.1,5.2,5.3,5.4,5.5,5.6,5.7,5.8,5.9,6,6.1,6.2,6.3,6.4,6.5,6.6,6.7,6.8,6.9,7,7.1,7.2,7.3,7
    mu =parameters_t[0]

    p_t = []
    p_t.append(meteo[0])
    p_t.append(meteo[1])
    p_t.append(meteo[2])
    p_t.append(meteo[3])
    p_t.append(Hs)

    #Calculate the probability of exceedance during 20 minutes
    for i in range(len(xi)):
        pt = m.exp(-((-1+m.sqrt(1+2*mu*xi[i]))**2)/(2*mu**2))
        prob_20 = 1-(1-pt)**N
        p_t.append(prob_20)

    return(p_t)

def Tayfun_Fedele(parameters_t,meteo,Tm):

    if len(meteo) > 17: #Threshold for different sampling
        Hs = meteo[8]
    else:
        Hs = meteo[7]

    #Define the duration [s]
    d = 1200 #s

    #Calculate average number of waves
    N = d/Tm

    #Vector with ratios eta/sigma
    xi = [2,2.2,2.4,2.6,2.8,3,3.2,3.4,3.6,3.8,4,4.2,4.4,4.6,4.8,5,5.2,5.4,5.6,5.8,6]
    #xi =
    ↪   [5,5.1,5.2,5.3,5.4,5.5,5.6,5.7,5.8,5.9,6,6.1,6.2,6.3,6.4,6.5,6.6,6.7,6.8,6.9,7,7.1,7.2,7.3,7
    mu =parameters_t[0]
    mu_m = parameters_t[1]

    #The approximation for the bound excess kurtosis
    l40 = 18*mu_m**2
    Lambda = 8*l40/3

    p_tf = []
    p_tf.append(meteo[0])
    p_tf.append(meteo[1])
    p_tf.append(meteo[2])
    p_tf.append(meteo[3])
    p_tf.append(Hs)

    #Calculate the probability of exceedance during 20 minutes
    for i in range(len(xi)):
        ptf = m.exp(-0.5*((-1+m.sqrt(1+2*mu*xi[i]))/mu)**2)*(1+Lambd
        ↪   a/64*xi[i]**2*(xi[i]**2-4))
        prob_20 = 1-(1-ptf)**N
        p_tf.append(prob_20)
```

```python
    return(p_tf)

def STE1(parameters_ste,meteo,Tm):

    if len(meteo) > 17: #Threshold for different sampling
        Hs = meteo[8]
    else:
        Hs = meteo[7]

    #Extract the space-time parameters

    Lx = parameters_ste[1]
    Ly = parameters_ste[2]
    axt = parameters_ste[3]
    ayt = parameters_ste[4]
    axy = parameters_ste[5]


    if abs(axt) > 1 or abs(ayt) > 1 or abs(axy)>1:
        print(meteo[0],meteo[1],meteo[2],meteo[3])


    #Define the spatial grid [m]
    x = [0,0.5,5,6.5,10,15,20,25,30,35,40,45,50,55,60,65,70,75,80,85,90,95,100] #m
    y = [0,0.5,5,6.5,10,15,20,25,30,35,40,45,50,55,60,65,70,75,80,85,90,95,100] #m
    #Define the duration [s]
    d = 1200 #s

    #Vector with ratios eta/sigma
    z = [2,2.2,2.4,2.6,2.8,3,3.2,3.4,3.6,3.8,4,4.2,4.4,4.6,4.8,5,5.2,5.4,5.6,5.8,6]
    #z =
    ↪ [5,5.1,5.2,5.3,5.4,5.5,5.6,5.7,5.8,5.9,6,6.1,6.2,6.3,6.4,6.5,6.6,6.7,6.8,6.9,7,7.1,7.2,7.3,7
    p_ste1_total = []
    for j in range(len(x)):

        Nv = 2*np.pi*(x[j]*y[j]*d↵
        ↪  )/(Lx*Ly*Tm)*m.sqrt(1-axt**2-axy**2-ayt**2+2*axt*axy*ayt)
        Ns = m.sqrt(2*np.pi)*((x[j]*d)/(Lx*Tm)*m.sqrt(1-axt**2) +
        ↪  (x[j]*y[j])/(Lx*Ly)*m.sqrt(1-axy**2) + (y[j]*d)/(Ly*Tm)*m.sqrt(1-ayt**2)
        ↪  )
        Nb = x[j]/Lx+y[j]/Ly+d/Tm


        #Most probable maximum of eta/sigma
        h_st = abs(fsolve(f,[4],(Nv,Ns,Nb))) #Solve the implicit function for H_st

        p_ste = []
        p_ste.append(meteo[0])
        p_ste.append(meteo[1])
        p_ste.append(meteo[2])
        p_ste.append(meteo[3])
        p_ste.append(Hs)
```

```python
        #Calculate the probability of exceedance during 20 minutes
        for i in range(len(z)):
            pste =
            ↪  m.exp(-m.exp(-(z[i]-h_st)*(h_st-(2*Nv*h_st+Ns)/(Nv*h_st**2+Ns*h_st+Nb))))
            prob_20 = 1-pste
            p_ste.append(prob_20)
        p_ste1_total.append(p_ste)




    return(p_ste1_total)




def STE2(parameters_ste,meteo,Tm,parameters_t):
    if len(meteo) > 17: #Threshold for different sampling
        Hs = meteo[8]
    else:
        Hs = meteo[7]

    #Extract the space-time parameters
    mu = parameters_t[0]
    Lx = parameters_ste[1]
    Ly = parameters_ste[2]
    axt = parameters_ste[3]
    ayt = parameters_ste[4]
    axy = parameters_ste[5]

    #Define the spatial grid [m]
    x = [0,0.5,5,6.5,10,15,20,25,30,35,40,45,50,55,60,65,70,75,80,85,90,95,100] #m
    y = [0,0.5,5,6.5,10,15,20,25,30,35,40,45,50,55,60,65,70,75,80,85,90,95,100] #m
    #Define the duration [s]
    d = 1200 #s

    #Vector with ratios eta/sigma
    xi = [2,2.2,2.4,2.6,2.8,3,3.2,3.4,3.6,3.8,4,4.2,4.4,4.6,4.8,5,5.2,5.4,5.6,5.8,6]
    #xi =
    ↪  [5,5.1,5.2,5.3,5.4,5.5,5.6,5.7,5.8,5.9,6,6.1,6.2,6.3,6.4,6.5,6.6,6.7,6.8,6.9,7,7.1,7.2,7.3,7

    p_ste2_total = []
    for j in range(len(x)):
        Nv = 2*np.pi*(x[j]*y[j]*d↵
        ↪  )/(Lx*Ly*Tm)*m.sqrt(1-axt**2-axy**2-ayt**2+2*axt*axy*ayt)
        Ns = m.sqrt(2*np.pi)*((x[j]*d)/(Lx*Tm)*m.sqrt(1-axt**2) +
        ↪  (x[j]*y[j])/(Lx*Ly)*m.sqrt(1-axy**2) + (y[j]*d)/(Ly*Tm)*m.sqrt(1-ayt**2)
        ↪  )
        Nb = x[j]/Lx+y[j]/Ly+d/Tm


        #Most probable maximum of eta/sigma
        h_st = abs(fsolve(f,[4],(Nv,Ns,Nb))) #Solve the implicit function for H_st
```

```python
        p_ste2 = []
        p_ste2.append(meteo[0])
        p_ste2.append(meteo[1])
        p_ste2.append(meteo[2])
        p_ste2.append(meteo[3])
        p_ste2.append(Hs)

        #Calculate the probability of exceedance during 20 minutes
        for i in range(len(xi)):
            pste =
            ↪  m.exp(-m.exp(-((xi[i]-h_st-mu/2*h_st**2)*(h_st-(2*Nv*h_st+Ns)/(Nv*h_st**2+Ns*h_st+Nb
            prob_20 = 1-pste
            p_ste2.append(prob_20)
        p_ste2_total.append(p_ste2)


    return(p_ste2_total)



def STE1_QD(parameters_ste,meteo,Tm,autocor):

    if len(meteo) > 17: #Threshold for different sampling
        Hs = meteo[8]
    else:
        Hs = meteo[7]

    #Extract the space-time parameters

    Lx = parameters_ste[1]
    Ly = parameters_ste[2]
    axt = parameters_ste[3]
    ayt = parameters_ste[4]
    axy = parameters_ste[5]

    psi_star = autocor[0]
    sigma = Hs/4

    if abs(axt) > 1 or abs(ayt) > 1 or abs(axy)>1:
        print(meteo[0],meteo[1],meteo[2],meteo[3])


    #Define the spatial grid [m]
    x = [0,0.5,5,6.5,10,15,20,25,30,35,40,45,50,55,60,65,70,75,80,85,90,95,100] #m
    y = [0,0.5,5,6.5,10,15,20,25,30,35,40,45,50,55,60,65,70,75,80,85,90,95,100] #m
    #Define the duration [s]
    d = 1200 #s

    #Vector with ratios h/Hs
    z =
    ↪  [1*Hs,1.1*Hs,1.2*Hs,1.3*Hs,1.4*Hs,1.5*Hs,1.6*Hs,1.7*Hs,1.8*Hs,1.9*Hs,2*Hs,2.1*Hs,2.2*Hs,2.3*
    #z =
    ↪  [2*Hs,2.1*Hs,2.2*Hs,2.3*Hs,2.4*Hs,2.5*Hs,2.6*Hs,2.7*Hs,2.8*Hs,2.9*Hs,3*Hs,3.1*Hs,3.2*Hs,3.3*

    p_Hste1_total = []
    for j in range(len(x)):
```

```python
        Nv = 2*np.pi*(x[j]*y[j]*d↲
        ↪ )/(Lx*Ly*Tm)*m.sqrt(1-axt**2-axy**2-ayt**2+2*axt*axy*ayt)
        Ns = m.sqrt(2*np.pi)*((x[j]*d)/(Lx*Tm)*m.sqrt(1-axt**2) +
        ↪ (x[j]*y[j])/(Lx*Ly)*m.sqrt(1-axy**2) + (y[j]*d)/(Ly*Tm)*m.sqrt(1-ayt**2)
        ↪ )
        Nb = x[j]/Lx+y[j]/Ly+d/Tm


        #Most probable maximum of eta/sigma
        h_st = abs(fsolve(f,[4],(Nv,Ns,Nb))) #Solve the implicit function for H_st

        p_ste = []
        p_ste.append(meteo[0])
        p_ste.append(meteo[1])
        p_ste.append(meteo[2])
        p_ste.append(meteo[3])
        p_ste.append(Hs)

        #Calculate the probability of exceedance during 20 minutes
        for i in range(len(z)):
            pste =
            ↪ m.exp(-m.exp(-(z[i]-h_st*sigma*m.sqrt(2*(1-psi_star)))*((h_st-(2*Nv*h_st+Ns)/(Nv*h_s
            prob_20 = 1-pste
            p_ste.append(prob_20)
        p_Hste1_total.append(p_ste)

    return(p_Hste1_total)

def f(h,Nv,Ns,Nb): #This is the implicit function to solve for h_st
    return (Nv*h**2+Ns*h+Nb)*m.exp(-h**2/2)-1



#Here the seperate functions containing the probability models are excecuted
def main():

    name_f =['\\Foristall_1998', '\\Foristall_1999',
    ↪ '\\Foristall_2000','\\Foristall_2001', '\\Foristall_2002',
    ↪ '\\Foristall_2003','\\Foristall_2004',
        '\\Foristall_2005', '\\Foristall_2006','\\Foristall_2007',
        ↪ '\\Foristall_2008', '\\Foristall_2009','\\Foristall_2010',
        ↪ '\\Foristall_2011', '\\Foristall_2012',
        '\\Foristall_2013', '\\Foristall_2014','\\Foristall_2015',
        ↪ '\\Foristall_2016', '\\Foristall_2017','\\Foristall_2018',
        ↪ '\\Foristall_2019', '\\Foristall_2020']

    name_t =['\\Tayfun_1998', '\\Tayfun_1999', '\\Tayfun_2000','\\Tayfun_2001',
    ↪ '\\Tayfun_2002', '\\Tayfun_2003','\\Tayfun_2004',
        '\\Tayfun_2005', '\\Tayfun_2006','\\Tayfun_2007', '\\Tayfun_2008',
        ↪ '\\Tayfun_2009','\\Tayfun_2010', '\\Tayfun_2011', '\\Tayfun_2012',
        '\\Tayfun_2013', '\\Tayfun_2014','\\Tayfun_2015', '\\Tayfun_2016',
        ↪ '\\Tayfun_2017','\\Tayfun_2018', '\\Tayfun_2019', '\\Tayfun_2020']

    name_ste =['\\STE_1998', '\\STE_1999', '\\STE_2000','\\STE_2001', '\\STE_2002',
    ↪ '\\STE_2003','\\STE_2004',
```

```
        '\\STE_2005', '\\STE_2006','\\STE_2007', '\\STE_2008',
        ↪    '\\STE_2009','\\STE_2010', '\\STE_2011', '\\STE_2012',
        '\\STE_2013', '\\STE_2014','\\STE_2015', '\\STE_2016',
        ↪    '\\STE_2017','\\STE_2018', '\\STE_2019', '\\STE_2020']

name_data =['\\data_1998', '\\data_1999', '\\data_2000','\\data_2001',
↪    '\\data_2002', '\\data_2003','\\data_2004',
    '\\data_2005', '\\data_2006','\\data_2007', '\\data_2008',
    ↪    '\\data_2009','\\data_2010', '\\data_2011', '\\data_2012',
    '\\data_2013', '\\data_2014','\\data_2015', '\\data_2016',
    ↪    '\\data_2017','\\data_2018', '\\data_2019', '\\data_2020']

name_rayleigh =['\\Rayleigh_1998', '\\Rayleigh_1999',
↪    '\\Rayleigh_2000','\\Rayleigh_2001', '\\Rayleigh_2002',
↪    '\\Rayleigh_2003','\\Rayleigh_2004',
    '\\Rayleigh_2005', '\\Rayleigh_2006','\\Rayleigh_2007', '\\Rayleigh_2008',
    ↪    '\\Rayleigh_2009','\\Rayleigh_2010', '\\Rayleigh_2011',
    ↪    '\\Rayleigh_2012',
    '\\Rayleigh_2013', '\\Rayleigh_2014','\\Rayleigh_2015', '\\Rayleigh_2016',
    ↪    '\\Rayleigh_2017','\\Rayleigh_2018', '\\Rayleigh_2019',
    ↪    '\\Rayleigh_2020']

name_rayleigh_cor =['\\Rayleigh_cor_1998', '\\Rayleigh_cor_1999',
↪    '\\Rayleigh_cor_2000','\\Rayleigh_cor_2001', '\\Rayleigh_cor_2002',
↪    '\\Rayleigh_cor_2003','\\Rayleigh_cor_2004',
    '\\Rayleigh_cor_2005', '\\Rayleigh_cor_2006','\\Rayleigh_cor_2007',
    ↪    '\\Rayleigh_cor_2008', '\\Rayleigh_cor_2009','\\Rayleigh_cor_2010',
    ↪    '\\Rayleigh_cor_2011', '\\Rayleigh_cor_2012',
    '\\Rayleigh_cor_2013', '\\Rayleigh_cor_2014','\\Rayleigh_cor_2015',
    ↪    '\\Rayleigh_cor_2016', '\\Rayleigh_cor_2017','\\Rayleigh_cor_2018',
    ↪    '\\Rayleigh_cor_2019', '\\Rayleigh_cor_2020']


name_foristall =['\\Foristall_1998', '\\Foristall_1999',
↪    '\\Foristall_2000','\\Foristall_2001', '\\Foristall_2002',
↪    '\\Foristall_2003','\\Foristall_2004',
    '\\Foristall_2005', '\\Foristall_2006','\\Foristall_2007',
    ↪    '\\Foristall_2008', '\\Foristall_2009','\\Foristall_2010',
    ↪    '\\Foristall_2011', '\\Foristall_2012',
    '\\Foristall_2013', '\\Foristall_2014','\\Foristall_2015',
    ↪    '\\Foristall_2016', '\\Foristall_2017','\\Foristall_2018',
    ↪    '\\Foristall_2019', '\\Foristall_2020']

name_Tayfun =['\\Tayfun_1998', '\\Tayfun_1999', '\\Tayfun_2000','\\Tayfun_2001',
↪    '\\Tayfun_2002', '\\Tayfun_2003','\\Tayfun_2004',
    '\\Tayfun_2005', '\\Tayfun_2006','\\Tayfun_2007', '\\Tayfun_2008',
    ↪    '\\Tayfun_2009','\\Tayfun_2010', '\\Tayfun_2011', '\\Tayfun_2012',
    '\\Tayfun_2013', '\\Tayfun_2014','\\Tayfun_2015', '\\Tayfun_2016',
    ↪    '\\Tayfun_2017','\\Tayfun_2018', '\\Tayfun_2019', '\\Tayfun_2020']

name_Tayfun_Fedele =['\\Tayfun-Fedele_1998', '\\Tayfun-Fedele_1999',
↪    '\\Tayfun-Fedele_2000','\\Tayfun-Fedele_2001', '\\Tayfun-Fedele_2002',
↪    '\\Tayfun-Fedele_2003','\\Tayfun-Fedele_2004',
    '\\Tayfun-Fedele_2005', '\\Tayfun-Fedele_2006','\\Tayfun-Fedele_2007',
    ↪    '\\Tayfun-Fedele_2008', '\\Tayfun-Fedele_2009','\\Tayfun-Fedele_2010',
    ↪    '\\Tayfun-Fedele_2011', '\\Tayfun-Fedele_2012',
```

```
                '\\Tayfun-Fedele_2013', '\\Tayfun-Fedele_2014','\\Tayfun-Fedele_2015',
            ↪    '\\Tayfun-Fedele_2016', '\\Tayfun-Fedele_2017','\\Tayfun-Fedele_2018',
            ↪    '\\Tayfun-Fedele_2019', '\\Tayfun-Fedele_2020']

    name_STE1 =['\\STE1_1998', '\\STE1_1999', '\\STE1_2000','\\STE1_2001',
    ↪    '\\STE1_2002', '\\STE1_2003','\\STE1_2004',
            '\\STE1_2005', '\\STE1_2006','\\STE1_2007', '\\STE1_2008',
            ↪    '\\STE1_2009','\\STE1_2010', '\\STE1_2011', '\\STE1_2012',
            '\\STE1_2013', '\\STE1_2014','\\STE1_2015', '\\STE1_2016',
            ↪    '\\STE1_2017','\\STE1_2018', '\\STE1_2019', '\\STE1_2020']

    name_STE2 =['\\STE2_1998', '\\STE2_1999', '\\STE2_2000','\\STE2_2001',
    ↪    '\\STE2_2002', '\\STE2_2003','\\STE2_2004',
            '\\STE2_2005', '\\STE2_2006','\\STE2_2007', '\\STE2_2008',
            ↪    '\\STE2_2009','\\STE2_2010', '\\STE2_2011', '\\STE2_2012',
            '\\STE2_2013', '\\STE2_2014','\\STE2_2015', '\\STE2_2016',
            ↪    '\\STE2_2017','\\STE2_2018', '\\STE2_2019', '\\STE2_2020']

    name_STE1_QD =['\\STE1_QD_1998', '\\STE1_QD_1999',
    ↪    '\\STE1_QD_2000','\\STE1_QD_2001', '\\STE1_QD_2002',
    ↪    '\\STE1_QD_2003','\\STE1_QD_2004',
            '\\STE1_QD_2005', '\\STE1_QD_2006','\\STE1_QD_2007', '\\STE1_QD_2008',
            ↪    '\\STE1_QD_2009','\\STE1_QD_2010', '\\STE1_QD_2011', '\\STE1_QD_2012',
            '\\STE1_QD_2013', '\\STE1_QD_2014','\\STE1_QD_2015', '\\STE1_QD_2016',
            ↪    '\\STE1_QD_2017','\\STE1_QD_2018', '\\STE1_QD_2019', '\\STE1_QD_2020']


    name_autocor =['\\autocor_1998', '\\autocor_1999',
    ↪    '\\autocor_2000','\\autocor_2001', '\\autocor_2002',
    ↪    '\\autocor_2003','\\autocor_2004',
            '\\autocor_2005', '\\autocor_2006','\\autocor_2007', '\\autocor_2008',
            ↪    '\\autocor_2009','\\autocor_2010', '\\autocor_2011', '\\autocor_2012',
            '\\autocor_2013', '\\autocor_2014','\\autocor_2015', '\\autocor_2016',
            ↪    '\\autocor_2017','\\autocor_2018', '\\autocor_2019', '\\autocor_2020']

    for k in range(len(name_data)):
        #Import the relevant parameters from the pickles
        infile_f = open(path_foristall1 + name_f[k],'rb')
        data_foristall = pickle.load(infile_f)
        infile_f.close()

        infile_t = open(path_tayfun1 + name_t[k],'rb')
        data_tayfun = pickle.load(infile_t)
        infile_t.close()

        infile_ste = open(path_ste + name_ste[k],'rb')
        data_ste = pickle.load(infile_ste)
        infile_ste.close()

        #Import the autocorrolation parameters
        infile_autocor = open(path_autocor + name_autocor[k],'rb')
        data_autocor = pickle.load(infile_autocor)
        infile_autocor.close()

        #Import the wave data from the pickle
```

```python
infile_data = open("C:\\Users\\tijme\\Documents\\TU Delft\\Master
↪  Offshore\\Afstuderen\\Environmental data\\Python\\Pickle_data" +
↪  name_data[k], 'rb')
data_year = pickle.load(infile_data)
infile_data.close()


#Excecute Rayleigh model
prob_r = []
for i in range(len(data_foristall)):
    Tm = data_ste[i][0]   #Calculate the mean zero-crossing period Tm
    p_r = Rayleigh(data_year[0][i],Tm)
    prob_r.append(p_r)


file_r = open(path_rayleigh + name_rayleigh[k],'wb')
pickle.dump(prob_r,file_r)
file_r.close()

#Execute bandwidth corrected Rayleigh model
prob_r_cor = []
for i in range(len(data_foristall)):
    Tm = data_ste[i][0]   #Calculate the mean zero-crossing period Tm
    p_r_cor = Bandwidth_rayleigh(data_year[0][i],Tm,data_autocor[i])
    prob_r_cor.append(p_r_cor)


file_r_cor = open(path_rayleigh_cor + name_rayleigh_cor[k],'wb')
pickle.dump(prob_r_cor,file_r_cor)
file_r_cor.close()


#Excecute Foristall model
prob_f = []
for i in range(len(data_foristall)):
    Tm = data_ste[i][0]   #Calculate the mean zero-crossing period Tm
    p_f = Foristall(data_foristall[i],data_year[0][i],Tm)
    prob_f.append(p_f)

file_f = open(path_foristall + name_foristall[k],'wb')
pickle.dump(prob_f,file_f)
file_f.close()

#Excecute Tayfun model
prob_t = []
for i in range(len(data_tayfun)):
    Tm = data_ste[i][0]   #Calculate the mean zero-crossing period Tm
    p_t = Tayfun(data_tayfun[i],data_year[0][i],Tm)
    prob_t.append(p_t)

#Tayfun
file_t = open(path_tayfun + name_Tayfun[k],'wb')
pickle.dump(prob_t,file_t)
file_t.close()

#Excecute Tayfun-Fedele model
```

```python
    prob_tf = []
    for i in range(len(data_tayfun)):
        Tm = data_ste[i][0]   #Calculate the mean zero-crossing period Tm
        p_t = Tayfun_Fedele(data_tayfun[i],data_year[0][i],Tm)
        prob_tf.append(p_t)

    file_tf = open(path_tayfun_fedele + name_Tayfun_Fedele[k],'wb')
    pickle.dump(prob_tf,file_tf)
    file_tf.close()




    #Excecute STE1 model
    prob_ste1 = []
    for i in range(len(data_ste)):
        Tm = data_ste[i][0]   #Calculate the mean zero-crossing period Tm
        p_ste1 = STE1(data_ste[i],data_year[0][i],Tm)
        prob_ste1.append(p_ste1)

    file_ste1 = open(path_ste1 + name_STE1[k],'wb')
    pickle.dump(prob_ste1,file_ste1)
    file_ste1.close()

    #Excecute STE2 model
    prob_ste2 = []
    for i in range(len(data_ste)):
        Tm = data_ste[i][0]   #Calculate the mean zero-crossing period Tm
        p_ste2 = STE2(data_ste[i],data_year[0][i],Tm,data_tayfun[i])
        prob_ste2.append(p_ste2)



    file_ste2 = open(path_ste2 + name_STE2[k],'wb')
    pickle.dump(prob_ste2,file_ste2)
    file_ste2.close()

    #Excecute STE1-QD model
    prob_H_ste1 = []
    for i in range(len(data_ste)):
        Tm = data_ste[i][0]   #Calculate the mean zero-crossing period Tm
        p_Hste1 = STE1_QD(data_ste[i],data_year[0][i],Tm,data_autocor[i])
        prob_H_ste1.append(p_Hste1)

    file_ste1_QD = open(path_ste1QD + name_STE1_QD[k],'wb')
    pickle.dump(prob_H_ste1,file_ste1_QD)
    file_ste1_QD.close()


    print(data_year[0][0][0])




if __name__ == "__main__":
    main()
```

Bibliography

[1] TAA Adcock, PH Taylor, S Yan, QW Ma, and PAEM Janssen. Did the draupner wave occur in a crossing sea? *Proceedings of the Royal Society A: Mathematical, Physical and Engineering Sciences*, 467(2134): 3004–3021, 2011.

[2] Robert J Adler and Jonathan E Taylor. *Random fields and geometry.* Springer Science & Business Media, 2009.

[3] George Biddell Airy. *Tides and waves.* B. Fellowes, 1845.

[4] Alberto Alberello, Amin Chabchoub, Jason P Monty, Filippo Nelli, Jung Hoon Lee, John Elsnab, and Alessandro Toffoli. An experimental comparison of velocities underneath focussed breaking waves. *Ocean Engineering*, 155:201–210, 2018.

[5] Aque-RET. Types of foundations and moorings for offshore wind turbines, 2012. URL http://aquaret. com/indexea3d.html?option=com_content&view=article&id=203&Itemid=344&lang=en. [Online; accessed December 9, 2020].

[6] Are Mjaavatten. Matlab polyfix function to fit polynomial to data, 2020. URL https://nl.mathworks. com/matlabcentral/fileexchange/54207-polyfix-x-y-n-xfix-yfix-xder-dydx. [Online; accessed April 13, 2021].

[7] Anouk de Bakker. Infragravity waves, 2019. URL http://www.coastalwiki.org/wiki/ Infragravity_waves.

[8] Francesco Barbariol, Jean-Raymond Bidlot, Luigi Cavaleri, Mauro Sclavo, Jim Thomson, and Alvise Benetazzo. Maximum wave heights from global model reanalysis. *Progress in oceanography*, 175:139–160, 2019.

[9] Alvise Benetazzo, Francesco Barbariol, Filippo Bergamasco, Andrea Torsello, Sandro Carniel, and Mauro Sclavo. Observation of extreme sea waves in a space–time ensemble. *Journal of Physical Oceanography*, 45(9):2261–2275, 2015.

[10] Alvise Benetazzo, Fabrice Ardhuin, Filippo Bergamasco, Luigi Cavaleri, Pedro Veras Guimaraes, Michael Schwendeman, Mauro Sclavo, Jim Thomson, and Andrea Torsello. On the shape and likelihood of oceanic rogue waves. *Scientific Reports*, 7(1):1–11, 2017.

[11] Alvise Benetazzo, Francesco Barbariol, and Silvio Davison. Short-term/range extreme-value probability distributions of upper bounded space-time maximum ocean waves. *Journal of Marine Science and Engineering*, 8(9):679, 2020.

[12] Alvise Benetazzo, Francesco Barbariol, Paolo Pezzutto, Joanna Staneva, Arno Behrens, Silvio Davison, Filippo Bergamasco, Mauro Sclavo, and Luigi Cavaleri. Towards a unified framework for extreme sea waves from spectral models: Rationale and applications. *Ocean Engineering*, page 108263, 2020.

[13] Paolo Boccotti. *Wave mechanics for ocean engineering.* Elsevier, New York, 2000.

[14] Sung Boo, Jun Zou, and SW Im. Conceptual design of 5mw floating wind turbines for korean offshore. In *The 2013 World Congress on Advances in Structural Engineering and Mechanics, Jeju, Korean.*

[15] Sung Youn Boo, Steffen Allan Shelly, Daejun Kim, et al. Design and dynamic performances of y-wind floating offshore wind turbine platform. In *The 27th International Ocean and Polar Engineering Conference.* International Society of Offshore and Polar Engineers, 2017.

[16] Alan Buis. The atmosphere: Getting a handle on carbon dioxide. URL https://climate.nasa.gov/ news/2915/the-atmosphere-getting-a-handle-on-carbon-dioxide/.

[17] Floating Offshore Wind Carbon Trust. Market and technology review. *Prepared for the Scottish Government*, 2015.

[18] Mercè Casas-Prat and Leo H Holthuijsen. Short-term statistics of waves observed in deep water. *Journal of Geophysical Research: Oceans*, 115(C9), 2010.

[19] AD Cattrell, M Srokosz, BI Moat, and R Marsh. Can rogue waves be predicted using characteristic wave parameters? *Journal of Geophysical Research: Oceans*, 123(8):5624–5636, 2018.

[20] L Cavaleri, L Bertotti, L Torrisi, E Bitner-Gregersen, Marina Serio, and Miguel Onorato. Rogue waves in crossing seas: The louis majesty accident. *Journal of Geophysical Research: Oceans*, 117(C11), 2012.

[21] Luigi Cavaleri, Francesco Barbariol, Alvise Benetazzo, Luciana Bertotti, Jean-Raymond Bidlot, Peter Janssen, and Nils Wedi. The draupner wave: A fresh look and the emerging view. *Journal of Geophysical Research: Oceans*, 121(8):6061–6075, 2016.

[22] Marios Christou and Kevin Ewans. Field measurements of rogue water waves. *Journal of Physical Oceanography*, 44(9):2317–2335, 2014.

[23] Jintai Chung and GM Hulbert. A time integration algorithm for structural dynamics with improved numerical dissipation: the generalized-α method. 1993.

[24] GL DNV and Environmental Loads. recommended practice dnv-rp-c205. *Environmental conditions and environmental loads. Norway: Det Norske Veritas*, 2017.

[25] L Draper. 'freak'ocean waves. *Weather*, 21(1):2–4, 1966.

[26] John M Dudley, Véronique Sarano, and Fréderic Dias. On hokusai's great wave off kanagawa: Localization, linearity and a rogue wave in sub-antarctic waters. *Notes and Records of the Royal Society*, 67(2): 159–164, 2013.

[27] Kristian Dysthe, Harald E. Krogstad, and Peter Müller. Oceanic rogue waves. *Annual Review of Fluid Mechanics*, 40:287–310, 2008. ISSN 00664189.

[28] MD Earle, KE Steele, and DWC Wang. Use of advanced directional wave spectra analysis methods. *Ocean Engineering*, 26(12):1421–1434, 1999.

[29] Gerhard Ersdal and Erik Ho¨ rnlund. Assessment of offshore structures for life extension. In *International Conference on Offshore Mechanics and Arctic Engineering*, volume 48227, pages 277–284, 2008.

[30] D Faulkner. Shipping safety: a matter of concern. In *Proceedings-Institute of Marine Engineering Science and Technology Part B Journal of Marine Design and Operations*, pages 37–56. IMAREST PUBLICATIONS, 2003.

[31] Francesco Fedele. Space–time extremes in short-crested storm seas. *Journal of Physical Oceanography*, 42(9):1601–1615, 2012.

[32] Francesco Fedele and M Aziz Tayfun. On nonlinear wave groups and crest statistics. *Journal of Fluid Mechanics*, 620:221, 2009.

[33] Francesco Fedele, Alvise Benetazzo, Guillermo Gallego, Ping-Chang Shih, Anthony Yezzi, Francesco Barbariol, and Fabrice Ardhuin. Space–time measurements of oceanic sea states. *Ocean Modelling*, 70: 103–115, 2013.

[34] Francesco Fedele, Joseph Brennan, Sonia Ponce De León, John Dudley, and Frédéric Dias. Real world ocean rogue waves explained without the modulational instability. *Scientific reports*, 6:27715, 2016.

[35] Christophe Fochesato, Stéphan Grilli, and Frédéric Dias. Numerical modeling of extreme rogue waves generated by directional energy focusing. *Wave Motion*, 44:395–416, 04 2007. doi: 10.1016/j.wavemoti. 2007.01.003.

[36] George Z Forristall. Wave crest distributions: Observations and second-order theory. *Journal of physical oceanography*, 30(8):1931–1943, 2000.

[37] G George. Stokes. on the theory of oscillatory waves. *Transactions of the Cambridge Philosophical Society*, 8:441–455, 1847.

[38] Marcin Gradowski, Marco Alves, Rui Gomes, and Joao Henriques. Integration of a hydrodynamic negative spring concept into the owc spar buoy. 08 2017.

[39] Sverre Haver. A possible freak wave event measured at the draupner jacket january 1 1995. In *Rogue waves*, volume 2004, pages 1–8, 2004.

[40] Leo H. Holthuijsen. *Waves in Oceanic and Coastal Waters*. Cambridge University Press, 2007. doi: 10.1017/CBO9780511618536.

[41] Fons Huijs, Joop Mikx, Feike Savenije, and Erik-Jan de Ridder. Integrated design of floater, mooring and control system for a semi-submersible floating wind turbine. *Proceedings of the EWEA Offshore, Frankfurt, Germany*, 19:21, 2013.

[42] IRENA. Future of wind: Deployment, investment, technology, grid integration and socio-economic aspects (a global energy transformation paper. *International Renewable Energy Agency, Abu Dhabi*, 2019.

[43] Peter AEM Janssen. Nonlinear four-wave interactions and freak waves. *Journal of Physical Oceanography*, 33(4):863–884, 2003.

[44] SH Jeon, YU Cho, MW Seo, JR Cho, and WB Jeong. Dynamic response of floating substructure of spar-type offshore wind turbine with catenary mooring cables. *Ocean Engineering*, 72:356–364, 2013.

[45] Jason Jonkman. Definition of the floating system for phase iv of oc3. Technical report, National Renewable Energy Lab.(NREL), Golden, CO (United States), 2010.

[46] Jason Jonkman and Walter Musial. Offshore code comparison collaboration (oc3) for iea wind task 23 offshore wind technology and deployment. Technical report, National Renewable Energy Lab.(NREL), Golden, CO (United States), 2010.

[47] Jason Jonkman, Sandy Butterfield, Walter Musial, and George Scott. Definition of a 5-mw reference wind turbine for offshore system development. Technical report, National Renewable Energy Lab.(NREL), Golden, CO (United States), 2009.

[48] Feng Zhao Joyce Lee. Global offshore wind report 2020. *Global wind energy council*, 8 2020.

[49] A Kolios, M Borg, and D Hanak. Reliability analysis of complex limit states of floating wind turbines. *Journal of Energy Challenges and Mechanics*, 2(1):6–9, 2015.

[50] Y. J. Lee, C. Y. Ho, and Z. Z. Huang. Hydrodynamic responses of a spar-type floating wind turbine in high waves. *Journal of Mechanics*, 31(1):105–112, 2015. ISSN 18118216. doi: 10.1017/jmech.2014.69.

[51] Mareike Leimeister. Global limit states for the design of floating wind turbine support structures. In *13th EAWE PhD Seminar*, 2017.

[52] Lighthouse. A datawell directional waverider buoy, 2016. URL https://www.lighthouse-geo.com/equipment/2016/12/16/a-new-mkiii-for-hhi/. [Online; accessed January 17, 2021].

[53] Yichao Liu, Sunwei Li, Qian Yi, and Daoyi Chen. Developments in semi-submersible fl oating foundations supporting wind turbines : A comprehensive review. *Renewable and Sustainable Energy Reviews*, 60:433–449, 2016. ISSN 1364-0321. doi: 10.1016/j.rser.2016.01.109. URL http://dx.doi.org/10.1016/j.rser.2016.01.109.

[54] Guy Brindley Lizet Ramírez, Daniel Fraile. Offshore wind in europe, key trends and statistics 2019. *Wind Europe*, 2 2020.

[55] Michael S Longuet-Higgins. Observations of the directional spectrum of sea waves using the motions of a floating buoy. *Ocean wave spectra*, 1961.

[56] QW Ma and MH Patel. On the non-linear forces acting on a floating spar platform in ocean waves. *Applied Ocean Research*, 23(1):29–40, 2001.

[57] ML McAllister and TS van den Bremer. Experimental study of the statistical properties of directionally spread ocean waves measured by buoys. *Journal of Physical Oceanography*, 50(2):399–414, 2020.

[58] Nobuhito Mori and Peter AEM Janssen. On kurtosis and occurrence probability of freak waves. *Journal of Physical Oceanography*, 36(7):1471–1483, 2006.

[59] Nobuhito Mori, Peter AEM Janssen, and Miguel Onorato. Freak wave prediction from spectra. In *Proceedings of the 10th international workshop on wave hindcasting and forecasting and coastal hazard symposium*, page 13. Citeseer, 2007.

[60] JR Morison, JW Johnson, SA Schaaf, et al. The force exerted by surface waves on piles. *Journal of Petroleum Technology*, 2(05):149–154, 1950.

[61] Arvid Naess. On the distribution of crest to trough wave heights. *Ocean Engineering*, 12(3):221–234, 1985.

[62] Amir R Nejad and Jone Torsvik. Drivetrains on floating offshore wind turbines: lessons learned over the last 10 years. *Forschung im Ingenieurwesen*, pages 1–9, 2021.

[63] NOAA. Wave buoys national data buoy center, 2021. URL https://www.ndbc.noaa.gov/. [Online; accessed February 1, 2021].

[64] Miguel Onorato, Davide Proment, and Alessandro Toffoli. Triggering rogue waves in opposing currents. *Physical review letters*, 107(18):184502, 2011.

[65] Orcina. K01 floating wind turbine orcaflex model, 2019. URL https://www.orcina.com/resources/examples/?key=k. [Online; accessed December 1, 2020].

[66] Xiaoqi Qu, Yan Li, Yougang Tang, Zhiqiang Hu, Pei Zhang, and Tianchang Yin. Dynamic response of spar-type floating offshore wind turbine in freak wave considering the wave-current interaction effect. *Applied Ocean Research*, 100:102178, 2020.

[67] Amir Rasekhi Nejad, Erin E Bachynski, and Torgeir Moan. On tower top axial acceleration and drivetrain responses in a spar-type floating wind turbine. In *International Conference on Offshore Mechanics and Arctic Engineering*, volume 57779, page V009T12A009. American Society of Mechanical Engineers, 2017.

[68] W. Rosenthal and S. Lehner. Rogue Waves: Results of the MaxWave Project. *Journal of Offshore Mechanics and Arctic Engineering*, 130(2), 06 2008. ISSN 0892-7219. doi: 10.1115/1.2918126. URL https://doi.org/10.1115/1.2918126. 021006.

[69] A Ross and G Mckinnon. Orcina Project 1405 Wind Turbine Validation Report. Technical report, 2018.

[70] Carlo Ruzzo and Felice Arena. A numerical study on the dynamic response of a floating spar platform in extreme waves. *Journal of Marine Science and Technology*, 24(4):1135–1152, 2019.

[71] Stig E. Sand, N. E. Ottesen Hansen, Per Klinting, Ovet T. Gudmestad, and Martin J. Sterndorff. *Freak Wave Kinematics*, pages 535–549. Springer Netherlands, Dordrecht, 1990. ISBN 978-94-009-0531-3. doi: 10.1007/978-94-009-0531-3_34. URL https://doi.org/10.1007/978-94-009-0531-3_34.

[72] Paul Sclavounos, Christopher Tracy, and Sungho Lee. Floating offshore wind turbines: Responses in a seastate pareto optimal designs and economic assessment. In *International Conference on Offshore Mechanics and Arctic Engineering*, volume 48234, pages 31–41, 2008.

[73] P.D. Sclavounos, S Lee, J DiPietro, G Potenza, P Caramuscio, and G De Michele. Floating offshore wind turbines: Tension leg platform ad taught leg buoy concepts supporting 3-5 MW wind turbines. *European Wind Energy Conference EWEC*, 2010.

[74] Richard J Seymour and David Castel. Systematic underestimation of maximum crest heights in deep water using surface-following buoys. In *Proceedings of 17th International Conference on Offshore Mechanics and Arctic Engineering*, pages 1–8, 1998.

[75] Siemens Gamesa. Illustration of sg 14-222 ddd siemens turbine, 2020. URL `https://www.siemensgamesa.com/products-and-services/offshore/wind-turbine-sg-14-222-dd`. [Online; accessed June 8, 2021].

[76] Alexey Slunyaev, Ira Didenkulova, and Efim Pelinovsky. Rogue waters. *Contemporary Physics*, 52(6): 571–590, 2011.

[77] Hideyuki Suzuki and Akira Sato. Load on turbine blade induced by motion of floating platform and design requirement for the platform. In *International Conference on Offshore Mechanics and Arctic Engineering*, volume 42711, pages 519–525, 2007.

[78] Miguel Taboada, Alvaro Ortega, Rafael Martín, Albino Pombo, Jaime Moreu, et al. An evaluation of the effect that motions at the nacelle have on the cost of floating offshore wind turbines. In *Offshore Technology Conference*. Offshore Technology Conference, 2020.

[79] H Tamura, T Waseda, and Y Miyazawa. Freakish sea state and swell-windsea coupling: Numerical study of the suwa-maru incident. *Geophysical Research Letters*, 36(1), 2009.

[80] M Aziz Tayfun. Narrow-band nonlinear sea waves. *Journal of Geophysical Research: Oceans*, 85(C3): 1548–1552, 1980.

[81] M Aziz Tayfun and Francesco Fedele. Wave-height distributions and nonlinear effects. *Ocean engineering*, 34(11-12):1631–1649, 2007.

[82] Paul H Taylor, Philip Jonathan, and Léon A Harland. Time domain simulation of jack-up dynamics with the extremes of a gaussian process. 1997.

[83] A Toffoli, T Waseda, H Houtani, L Cavaleri, DM Greaves, and Miguel Onorato. Rogue waves in opposite currents: an experimental study on deterministic and stochastic wave trains. 2015.

[84] Alessandro Toffoli, L Fernandez, Jaak Monbaliu, M Benoit, E Gagnaire-Renou, JM Lefevre, L Cavaleri, Davide Proment, C Pakozdi, CT Stansberg, et al. Experimental evidence of the modulation of a plane wave to oblique perturbations and generation of rogue waves in finite water depth. *Physics of Fluids*, 25 (9):091701, 2013.

[85] Peter S Tromans, Ali R Anaturk, Paul Hagemeijer, et al. A new model for the kinematics of large ocean waves-application as a design wave. In *The First International Offshore and Polar Engineering Conference*. International Society of Offshore and Polar Engineers, 1991.

[86] Jeremy Lee UWA. Schematic view catenary and taut mooring, Nov 2018.

[87] Peter Wellens. Lecture notes in introduction to offshore hydromechanics, Sept 2019.

[88] Ma Yu, Zhi-qiang Hu, and Long-fei Xiao. Wind-wave induced dynamic response analysis for motions and mooring loads of a spar-type offshore floating wind turbine. *Journal of Hydrodynamics, Ser. B*, 26(6): 865–874, 2015.

[89] Vladimir E Zakharov and LA Ostrovsky. Modulation instability: the beginning. *Physica D: Nonlinear Phenomena*, 238(5):540–548, 2009.